BRNO UNIVERSITY OF TECHNOLOGY

VYSOKÉ UČENÍ TECHNICKÉ V BRNĚ

FACULTY OF MECHANICAL ENGINEERING

FAKULTA STROJNÍHO INŽENÝRSTVÍ

INSTITUTE OF PROCESS ENGINEERING

ÚSTAV PROCESNÍHO INŽENÝRSTVÍ

SIMULATIONS OF PHOTOBIOREACTORS FROM HYDRODYNAMICS AND MASS TRANSFER POINT OF VIEW

SIMULACE FOTOBIOREAKTORŮ Z POHLEDU HYDRODYNAMIKY A PŘENOSU HMOTY

DOCTORAL THESIS

DIZERTAČNÍ PRÁCE

AUTHOR — Ing. Miroslav Rebej

AUTOR PRÁCE

SUPERVISOR — doc. Ing. Zdeněk Jegla, Ph.D.

ŠKOLITEL

BRNO 2022

Abstract

Simulations of photobioreactors with microalgae-specific cultures is a field that connects microbiology with the multiphase fluid dynamics. In microalgae cultivation, it is necessary to account for various phenomena, e.g., multiphase hydrodynamics with water, CO_2 bubbles and microalgae, multiphase species mass transfer, radiation transport, light attenuation, growth and culmination of microalgae and their effect on fluid properties. Computational model presented in this doctoral dissertation thesis links the multiphase hydrodynamic model and the species mass transfer model. In the thesis, there is an overview of applicable computational models some given types of photobioreactors. The developed multiphase hydrodynamic model and the species mass transfer model then draw from this overview. Next, the accuracy of these models was compared with laboratory experiments. As a result, the developed computational model of the photobioreactor can be further extended with other sub-models, i.e., the irradiation model and the biomass growth model.

Keywords

photobioreactor, multiphase flow, PIV, bubbly flow, mass transfer, fluid dynamics

Abstrakt

Modelování fotobioreaktorů s kulturami specifických mikrořas je oborem, který propojuje mikrobiologii s vícefázovou mechanikou tekutin. Při kultivaci je nutné zohlednit řadu jevů, jako např. vícefázové proudění zahrnující vodu, bubliny CO_2 a mikrořasy, vícefázový přenos látek, přenos energie zářením, intenzitu pohlcování světla či růst a množení mikrořas a jejich vliv na vlastnosti tekutiny Výpočtový model prezentován v téhle doktorské dizertační práci právě propojuje vícefázový hydrodynamický model s modelem přenosu hmoty jednotlivých složek. V práci je uveden základní přehled výpočtových modelů aplikovatelných pro různé typy fotobioreaktorů. Z tohoto přehledu pak bylo vytvořeno finální nastavení vícefázového hydrodynamického modelu a modelu přenosu hmoty jednotlivý složek. Přesnost výpočtových sub-modelů pak byla ověřena pomocí laboratorních experimentů. Ve výsledku tak může být vyvinutý výpočtový model fotobioreaktora dále rozšířen o další výpočtové sub-modely, a to o model záření a model růstu mikrořas.

Klíčová slova

fotobioreaktor, vícefázové proudění, PIV, bublinkový tok, přestup hmoty, dynamika tekutin

REBEJ, Miroslav. *Simulations of photobioreactors from hydrodynamics and mass transfer point of view*. Brno, 2022. Available also at: https://www.vutbr.cz/studenti/zav-prace/detail/146666. Doctoral Thesis. Vysoké učení technické v Brně, Fakulta strojního inženýrství, Institute of Process Engineering. Supervisor Zdeněk Jegla.

I would like to express my gratitude to doc. Ing. Zdeněk Jegla, Ph.D., Ing. Jiří Vondál, Ph.D., and Ing. Tomáš Juřena, Ph.D. for supervising this work. Their guidance, support, and friendly advice have always been very valuable. Also, special thank you is due to my family and friends for their support and encouragements during my studies. Last but not least, I thank God for all the education I was gifted.

This research was supported by the EU project Strategic Partnership for Environmental Technologies and Energy Production, funded as project No. CZ.02.1.01/0.0/0.0/16_026/0008413 by Czech Republic Operational Programme Research, Development and Education, Priority Axis 1: Strengthening capacity for high-quality research.

Brno Ph.D. Talent Scholarship Holder – Funded by the Brno City Municipality.

Contents

1 Introduction

Microalgae are naturally ecologically diverse. Due to their ability to adapt to different life conditions, they can be found growing in many biotopes, e.g., damp places or aquatic environments. The algae lack various structures that characterize land plants, such as leaves or roots, and other organs that are found in other vascular plants. However, their uniqueness comes from the presence of chlorophyll and having photosynthetic ability in a single algal cell. Therefore, algal cultivation allows for rather easy operation for biomass generation and effective genetic and metabolic research in a much shorter time period than conventional plants (Pelczar et al., 1993). Microalgae, as biological CO_2 and O_2 exchangers, can offer some biotechnological potential, as well. Examples of areas where the microalgal technology can bring some novelty may be in areas of pharmaceuticals, cosmetics, agriculture, food, or environment. Their added value may be found, for instance, in production of high value bioproducts or in reduction of CO_2 emissions, see Table 1.1 for some examples. However, utilization of such biotechnology must be based on a strong biotechnological basis and intended biomass utilization must also be taken into account when considering a technical solution.

Table 1.1 Types of selected microalgae and their commercial relevance

Microalgae	Application	Reference
Thalassiosira weissflogii	Production of EPA and fucoxanthin	Marella and Tiwari (2020)
Chlorella vulgaris	Wastewater biotreatment	Sabeti et al. (2019)
	Production of SFA	Ramírez-López et al. (2019)
Scenedesmus obliquus	Protein extraction	Patnaik et al. (2019)
	Biodiesel production	Han et al. (2016)
Fistulifera solaris	PUFA and EPA production	Tanaka et al. (2017)
Phaeodactylum tricornutum	PUFA and EPA production	Rodolfi et al. (2017)
Chlorella protothecoides	Biodiesel production	Darpito et al. (2015)
Tetraselmis suecica	Biodiesel production	Heo et al. (2015)

EPA: eicosapentaenoic acid; PUFA: polyunsaturated fatty acid; SFA: saturated fatty acid

There are two major technical solutions for the cultivation of microorganisms, open and closed cultivation systems. Photobioreactors, i.e., closed technical systems for microalgal cultivation, give a clear advantage over open systems, such as ponds, when it comes to intensive production of high value bioproducts. Closed photobioreactors allow for cultivation under controlled conditions so that the medium does not get contaminated or lost, e.g., due to evaporation. However, cultivation processes in such photobioreactors have different operational requirements as living conditions of microalgae are often far from their natural habitat in closed vessels. The main differences may be higher cell densities in the medium resulting in issues with irradiation density and with light patterns, or different variations of pH and temperature. Moreover, due to induced flow velocities, the microalgae cells may experience constant shear stress at, or even above, potential death-levels (Pulz, 2001; Singh and Sharma, 2012).

Therefore, the design of any technical solutions needs to be evaluated for the cost-effective application and economic feasibility. Next, adequate control strategies and harvesting techniques have to be implemented to optimize the overall process yield. Nevertheless, to reach a state where optimum growth is maintained, all aspects of microalgae cultivation must be in balance, i.e. hydrodynamics, mass transfer, irradiation, and cell growth (Acién Fernández et al., 2013; Gao et al., 2018b).

1.1 Objectives of the Dissertation Thesis

The aim of this thesis is to provide mathematical models of a microalgae cultivation vessel. The methodology is based on multiphase flow analyses of the photobioreactor model that integrates the reactor's hydrodynamics with principles of mass transfer.

The beginning of this doctoral thesis (Chapter 2) is dedicated to the literature review that introduces numerical modelling of multiphase flows and its application in the field of photobioreactors. Individual aspects of numerical modelling of photobioreactors are then discussed in a greater detail. Chapter 3 then introduces two types of photobioreactors that were used in this work. Next, in Chapter 4 and 5 are presented individual computational models for hydrodynamics and mass transfer, respectively. These chapters also present preliminary work that was done to develop and set-up these models. Furthermore, the models are complemented with laboratory experiments so that the results could be validated, as well. At last, results of each model are discussed in respective summaries.

In addition to the hydrodynamic and mass transfer models, there is a brief demonstration of an additional irradiation model in Chapter 6. Lastly, final conclusions are discussed and some future work is proposed.

2 Literature Review

Computational Fluid Dynamics (CFD) is a powerful method for simulation of hydrodynamics, heat transfer and mass transfer in many engineering applications, including the field of photobioreactors (Bitog et al., 2011; Pires et al., 2017). Mathematical modelling of any phenomena can bring its understanding and to help overcome possible limitations. By utilizing the CFD, it is possible to predict even complex inherent phenomena (Bitog et al., 2014). However, comprehensive modelling of photobioreactors can be still very challenging in comparison to conventional reactors as there are strong interactions between fluid dynamics, nutrient concentration, light distribution, algae growth rate and a biomass distribution. Moreover, the coupling between physical, chemical and biological phenomenon is of a multi-time and multi-scale nature (Gao, 2016). Another complication in numerical analyses of multiphase flows is the lack of validated mesoscale models for the momentum interaction and momentum transfer between phases, or mass transfer between phases (Buffo and Marchisio, 2014). Furthermore, the application of CFD to describe biological processes is also less-explored (Pires et al., 2017).

Nevertheless, regarding other design methods, CFD modelling of photobioreactors gives several advantages, e.g. low cost, reduced workload or shorter design periods (Pires et al., 2017). For these reasons, the application of CFD modelling techniques in the field of photobioreactors is favourable anyway.

2.1 Numerical Modelling of Multiphase Flows

A large number of flows encountered in nature and industry are mixtures of phases. Advances in computational fluid mechanics have provided the basis for further insight into the dynamics of multiphase flows. As a result, the applicability of CFD methods to such flows has become common practice in engineering. Among the available multiphase simulation approaches for hydrodynamic studies, the Eulerian–Eulerian (E-E) and the Eulerian–Lagrangian (E-L) multiphase models have been popularly used. In any up-to-date CFD package, e.g. the ANSYS Fluent (ANSYS Inc., 2020a), there should be three different Eulerian-Eulerian multiphase models available: the volume of fluid model, the mixture model, and the full Eulerian model.

The Eulerian–Eulerian multiphase model averages the Navier–Stokes equations over the control volume and solves the continuity, mass, and momentum equations for a combination of fluid phases or fluid and solid phases. It considers all phases in the Eulerian representation, creating the need for mass and momentum balances for each phase. This approach uses only one pressure field for all phases and the interaction between phases is modelled through the interaction terms, e.g., the drag force, lift force, wall lubrication force, or turbulent dispersion force. However, their applicability and accuracy in the correct prediction of gas-liquid flow features is different for any considered case. Thus, making this multiphase approach rather complex. For instance, flow in bubble columns is driven by the rising bubbles so the main interfacial forces are buoyancy, drag, lift, and virtual mass. In case of a flow agitated by the stirrer, buoyancy and drag forces seem to dominate (Buffo and Marchisio, 2014).

In contrast to the Eulerian-Eulerian approach, the Eulerian-Lagrangian approach treats the secondary phases as single particles where particle trajectories are calculated as a result of forces acting on them. However, the primary phase is also treated as a continuum. The flow field is then calculated from balance equations of momentum, mass, and energy exchange between phases. The Eulerian-Lagrangian formulation may offer a detailed view on the bubbly flow inside a bubble column-type photobioreactor, including bubble trajectory and related interactions (Joshi, 2001). However, its limitation comes from the formulation that the bubbles are spherical and the number of bubbles that can be tracked puts high demands on the computational requirements (Bitog et al., 2011).

2.2 Review of Numerical Modelling in Photobioreactors

As already stated, the comprehensive modelling approach of a photobioreactor should include following sub-models (Gao et al., 2018b):

- Hydrodynamic model
- Mass transfer model
- Irradiation model
- Biomass growth model
- Coupling method

As a result, it is a complex task to study the characteristics of a culturing systems in photobioreactors with all sub-models combined. Therefore, the majority of studies puts focus only on a specific component of the photobioreactor model (Pires et al., 2017). Moreover, very little research has been focused on full-scale photobioreactors for mass cultivation. This is mainly due to the difficulties in maintaining internal environmental conditions of the full-scale photobioreactors, producing a similar light intensity and spectrum as sunlight, and evaluating the mixing efficiency according to the different photobioreactor designs (Seo et al., 2012). Table 2.1 lists some of the recent CFD studies in the field of photobioreactors.

Table 2.1 List of recent CFD publications

Author	CFD Code	Framework	Photobioreactor
Patil et al. (2021)	ANSYS Fluent	E-E	Bubble column
Pozzobon and Perré (2020)	OpenFOAM	E-L	Stirred tank
Guler et al. (2020)	ANSYS CFX	E-E	Airlift
Ali et al. (2019)	COMSOL	E-E	Flat-panel
Jin et al. (2019)	COMSOL	E-E	Membrane
López-Rosales et al. (2019)	ANSYS Fluent	E-E	Bubble column
Sabeti et al. (2019)	ANSYS Fluent	E-L	Stirred tank
Gao et al. (2018a)	ANSYS Fluent	E-E	Airlift
McHardy et al. (2018)	ANSYS CFX	E-E	Bubble column
Amini et al. (2018)	ANSYS Fluent	E-E	Open raceway pond
Papacek et al. (2018)	ANSYS Fluent	SP	Taylor-Couette
Farhadian et al. (2018)	ANSYS Fluent	E-E	Airlift
Zhao et al. (2018)	ANSYS Fluent	E-E	Flat-panel
He et al. (2017)	ANSYS Fluent	E-L	Tubular
Zeng et al. (2016)	ANSYS CFX	SP	Open raceway pond
Chen et al. (2016)	ANSYS CFX	E-E	Airlift
Zhang et al. (2015)	COMSOL	E-E	Flat-panel
Soman and Shastri (2015)	ANSYS Fluent	E-E	Airlift/Flat-panel
Huang et al. (2015a)	ANSYS CFX	E-E	Flat-panel
Huang et al. (2015b)	ANSYS CFX	SP	Open raceway pond
Gao et al. (2015b)	ANSYS Fluent	E-E	Taylor-Couette
Park and Li (2015)	ANSYS Fluent	SP	Open raceway pond
McClure et al. (2014)	ANSYS CFX	E-E	Bubble column
Zhang et al. (2013)	ANSYS Fluent	SP	Tubular

E-E: Eulerian-Eulerian multiphase framework; E-L: Eulerian-Lagrangian multiphase framework; SP: Single-phase framework

In the recent publications related to CFD and photobioreactors, the ANSYS Fluent and ANSYS CFX are the most common CFD codes. Next, the full Eulerian-Eulerian approach is used the most often among those publications. Moreover, the two-fluid Eulerian CFD framework is the only one actually usable for high gas-flow rates at the industrial scale (Cappello et al., 2021).

The number of terms to be modelled in the momentum equations in multiphase flows is always large, and this makes the modelling of turbulence in multiphase simulations extremely complex. Similarly to single-phase flows, there are the k-ε, k-ω, and the Reynolds Stress Model (RSM) closure models extended to multiphase flow application. Such extensions are meant to capture the underlaying physics when the single-phase models fail. These extensions, however, provide another challenge in balancing the accuracy and time. Based on the literature review, the practice most often applied in flows with low gas volume fraction is to use the two-equation turbulence model, e.g., the k-ε model, for the continuous phase and an interaction term to couple the fluctuations in all phases.

Another simplification applied to the gas-liquid flows in photobioreactors is to assume that the secondary phase is dispersed in the forms of droplets or bubbles. Naturally, these bubbles can have various shapes and sizes, so they are usually simplified to spheres of a single diameter. Nevertheless, the use of a constant bubble size is often very gross simplification that, on the other hand, allows to easily model bubble flows. The available multiphase numerical modelling approach that is able to handle multiple bubble sizes can be based on the calculation of population balance equations. This approach, however, introduces a large set of additional equations and, therefore, significantly increases computational requirements. Favourably, the bubble shape can be approximated by the proper choice of a drag model. The drag model and its drag coefficient are the most important interaction terms between phases in numerical modelling of gas-liquid flows (ANSYS Inc., 2020a). The term links momentum exchange between phases and is usually empirically based. The most recommended drag models for flows where bubbles can have various shapes are the Grace (Grace et al., 1976), Tomiyama (Tomiyama, 1998), and Ishii-Zuber (Ishii and Zuber, 1979) drag model. The simplest drag model formulation, the Schiller–Naumann drag correlation, is not considered to be the best option for drag force in aerated systems (Soman and Shastri, 2015). Also, the best applicability to bubble swarm flows may offer the Ishi-Zuber drag model but, generally, there is a lack of understanding of bubble swarm flows (Ngo and Lim, 2020).

Other meso-scale (interaction) models may be difficult to include, and authors are not united in the importance of what interaction forces are necessary. For instance, Cappello et al. (2021) in their large scale-up work considered only drag forces and concluded that other forces did not lead to any clear improvement. Guler et al. (2020), on the other hand, included all possible interactions, i.e., drag, lift, virtual mass, wall lubrication, turbulent dispersion, and turbulence transfer. The overview of numerical models found in the literature review is presented in Table 2.2.

Table 2.2 Interaction models

Author	Bubble size	Turbulence model	Drag	Lift	Virtual mass	Wall lubrication	Turbulent dispersion	Turbulence transfer
Patil et al. (2021)	N/A	standard k-ε	Grace	Tomiyama	no	Antal	no	no
Guler et al. (2020)	3 mm	SST k-ω	Grace	Legendre-Magnaudet	constant	Frank	Burns	Sato
Ali et al. (2019)	8 mm	k-ε	constant	no	no	no	no	no
Jin et al. (2019)	1 mm	standard k-ε	Schiller and Naumann	no	no	no	no	no
López-Rosales et al. (2019)	4.5 to 7 mm	realizable k-ε	Grace	no	no	no	no	no
Gao et al. (2018a)	3 mm	RSM	Tomiyama	constant	constant	Antal	Burns	Sato
McHardy et al. (2018)	7 mm	SST k-ω	Grace, Ishii-Zuber	Legendre-Magnaudet	constant	Frank	Burns	no
Farhadian et al. (2018)	3 mm	k-ε	Schiller and Naumann	no	no	no	no	no
Zhao et al. (2018)	5 mm	standard k-ε	yes	yes	yes	no	no	no
Chen et al. (2016)	2 to 5 mm	standard k-ε	Grace	no	no	no	no	Sato
Zhang et al. (2015)	2 mm	standard k-ε	constant	no	no	no	no	no
Soman and Shastri (2015)	5 mm	standard k-ε	Schiller and Naumann	no	no	no	no	no

2.3 Gas-Liquid Hydrodynamics

In the photobioreactor technology, the gaseous phase serves primarily as a nutrient for cells. In addition to that, it can also affect mixing of the medium (Bitog et al., 2014). Therefore, bubbles can have an impact on a variety of chemical and biochemical reactions that take place in the vessel (Almani et al., 2021). Often, the strategy is to study bubbly flow at the level of a single bubble and apply the findings and setup to subsequent, more complex, flow studies (Ziegenhein and Lucas, 2017).

The bubbly flow is defined by means of the following dimensionless numbers: the Eötvös number (Eo), the Reynolds number (Re), and the Morton number (Mo). Their definitions are in Eqs. (1) to (3), respectively (Ziegenhein and Lucas, 2017).

$$Eo = \frac{\Delta\rho g d_B^2}{\sigma} \tag{1}$$

$$Re = \frac{\rho_p u_{slip} d_B}{\mu_p} \tag{2}$$

$$Mo = \frac{g\mu_p^4 \Delta\rho}{\rho_p^2 \sigma^3} \tag{3}$$

where $\Delta\rho$ is the density difference of the primary and the secondary phase, g is the gravitational acceleration, d_B is the bubble diameter, σ is the surface tension, ρ_p is the density of the primary phase, u_{slip} is the slip velocity between phases, and μ_p is the dynamic viscosity of the primary phase.

Depending on the medium and the flow regime, bubbles can have various forms of shapes. This is expressed in the Grace diagram in Figure 2.1 where the bubble shape description is based on the aforementioned dimensionless numbers. However, a problem can arise when defining the bubble size in terms of a single diameter. Hence, there are different approaches to define the equivalent bubble diameter in the literature. Dijkhuizen et al. (2010) based the bubble equivalent diameter on the horizontal and vertical diameter, d_h and d_v respectively, that were found in an experiment. Calculated equivalent bubble diameter was defined by Eq. (4).

$$d_B = (d_h^2 d_v)^{1/3} \tag{4}$$

Ziegenhein and Lucas (2017), on the other hand, took the major and minor axis of the projected bubble area. The equivalent bubble diameter was then defined as the spherical equivalent of the rotational volume. In the work of Thobie et al. (2017), the equivalent diameter corresponds to the diameter of a spherical bubble having the same projected area as the measured bubble. However, this approach may result in an overestimation of the real equivalent diameter in case of large bubbles which are flattened in the column gap.

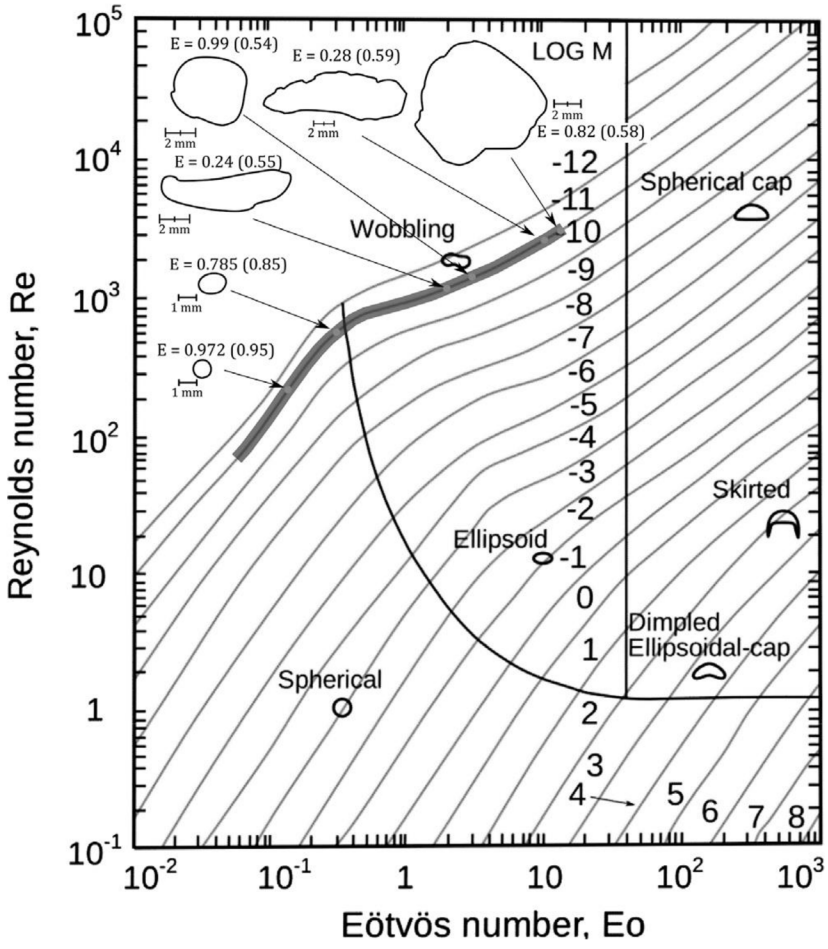

Figure 2.1 Grace diagram (Grace et al., 1976; Ziegenhein and Lucas, 2017)

2.4 Gas-Liquid Mass Transfer

Understanding the gas-liquid mass-transfer process in (photo)bioreactors is a key to improved reactor designs and reactor operation as they are important to maximize efficiency and minimize costs. Because of the low solubility of most gases, the gas–liquid mass transfer often becomes the rate-limiting step for the overall reaction (Linek et al., 1996). Typically, a bioreactor for gas treatment is operating under mass transfer or kinetically limited conditions. Understanding the rate-limiting steps in such system, therefore, gives opportunities to optimize the design and operations of the system for a specific application. The overall volumetric mass-transfer rate (R) from the gas phase to the aqueous phase (where microorganisms are suspended or growing as a biofilm) follows the description in Eq. (5) (Kraakman et al., 2011).

$$R = k_L a(C_G/H - C_L) \tag{5}$$

where $k_L a$ is the volumetric mass-transfer coefficient, H is the Henry coefficient, and C_L and C_G are the pollutant concentrations in the liquid and gaseous phase, respectively.

The overall mass-transfer coefficient is a combination of a series of partial mass-transfer coefficients as shown in Figure 2.2. Normally, the overall mass-transfer rate is controlled by the liquid film resistances around bubbles. However, the liquid-side volumetric mass-transfer is difficult to estimate as it is affected by many factors, e.g., gas hold-up, bubble size, slip velocity and turbulent energy dissipation rate. Moreover, these factors are also depended on reactor operating conditions, geometry, and physical properties of the gas and liquid phases (Gao, 2016).

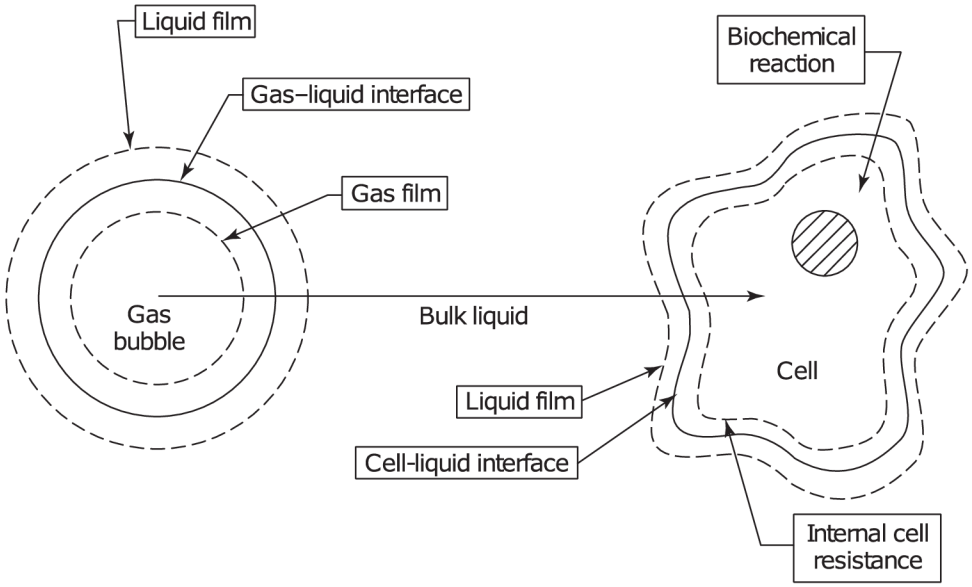

Figure 2.2 Mass transfer pathway (Kadic and Heindel, 2014)

Nevertheless, the overall mass-transfer coefficient is often reduced to a mass transfer rate coefficient for the gas phase (k_G), the mass transfer rate coefficient for the liquid phase (k_L), and the mass transfer rate coefficient for the biofilm (k_B). Furthermore, since the k_L coefficient is the most dominant, other coefficients are often neglected. The k_L coefficient is usually modulated by the specific gas–liquid interfacial area a, giving the volumetric mass-transfer coefficient $k_L a$.

There are different models available to predict the mass-transfer coefficient (Chisti, 1989):

- Two-film theory
- Penetration model
- Surface renewal model
- Eddy cell model

Models used the most often in works related to (photo)bioreactors are the Penetration model (Higbie, 1935) and the Eddy cell model (Lamont and Scott, 1970). The Penetration model in Eq. (6) assumes unsteady mass transfer only when a liquid element is in contact with bubbles and at equilibrium at the gas-liquid interface. The model is also characterised by the fact that each liquid element is in contact with the gaseous phase for the same time.

$$k_L = \mathrm{F}\sqrt{\frac{4D_L u_{slip}}{\pi d_b}} \tag{6}$$

In contrast to that, the Eddy cell model in Eq. (7) predicts the mass transfer based on the interfacial surface renewal by small scale eddies.

$$k_L = \mathrm{K}\sqrt{\frac{4D_L}{\pi}\sqrt{\frac{\varepsilon_L}{\nu_L}}} \tag{7}$$

In addition to the models presented in Chisti (1989), Gao et al. (2015a) introduced an adaptive model in Eq. (8) where the k_L coefficient is modelled according to the computed time and turbulent dissipation. This is presented in Figure 2.3 and Figure 2.4. However, this adaptive model was validated only for a semi-batch gas-liquid Taylor-Couette bioreactor. The reason is that the penetration model usually underpredicts the mass transfer for highly turbulent flows, while the eddy cell model tends to underpredict mass transfer for weakly turbulent flows. In addition to that, the interfacial contact time in the surface renewal model is strongly dependent on operational conditions and reactor geometry rendering it difficult to use as a scale-up guide (Kadic and Heindel, 2014).

$$k_L = \max\left(\mathrm{F}\sqrt{\frac{4D_L u_{slip}}{\pi d_b}}, \mathrm{K}\sqrt{\frac{4D_L}{\pi}\sqrt{\frac{\varepsilon_L}{\nu_L}}}\right) \tag{8}$$

In many cases, the k_L and a are difficult to obtain separately in experiments. However, $k_L a$ can be obtained from macroscopic measurements (Kadic and Heindel, 2014). Also, there are different semi-empirical correlations for gas hold-up in bioreactors available (Luo and Al-Dahhan, 2010).

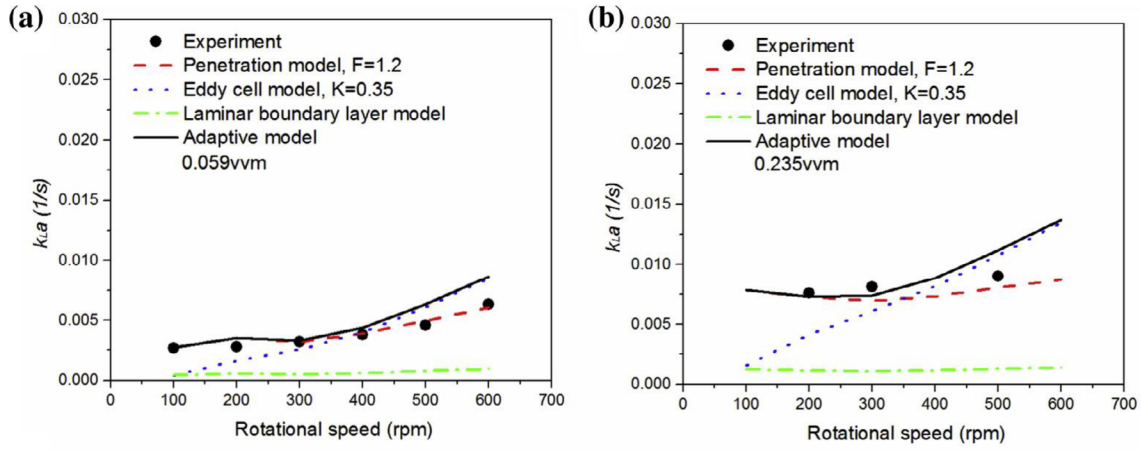

Figure 2.3 Comparison of predicted average volumetric mass transfer rate by different mass transfer models with experimental data under different rotational speeds (Gao et al., 2015a)

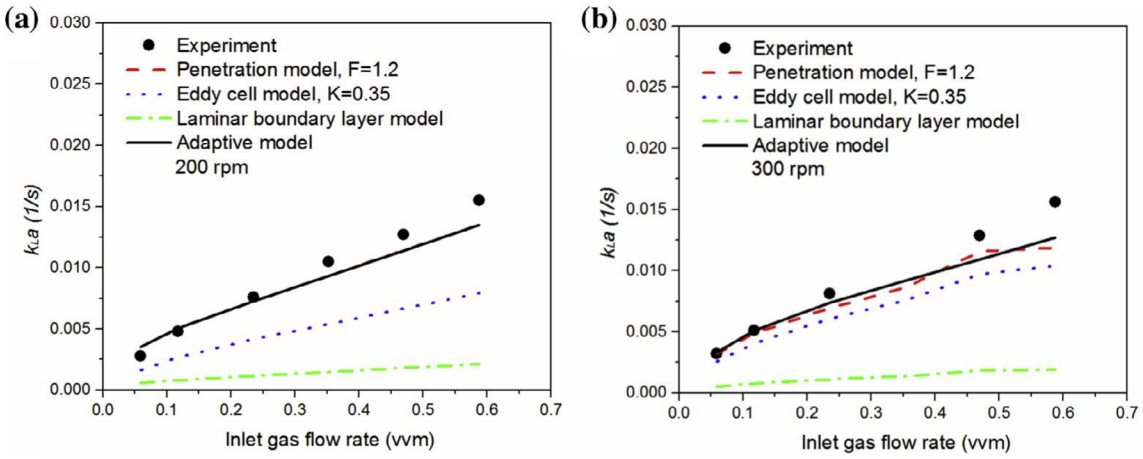

Figure 2.4 Comparison of predicted average volumetric mass transfer rate by different mass transfer models with experimental data under different inlet gas flow rates (Gao et al., 2015a)

2.5 Irradiation

For photoautotrophic microorganisms like microalgae, light is also required as a fundamental nutrient (Acién Fernández et al., 2013). As the light availability and light intensity are important factors in controlling cell growth, the low efficiencies may result from different light conditions due to the change of optical densities of the algae suspension during the cultivation process. This is schematically shown in Figure 2.5. Whereas diluted cultures with low biomass concentrations (less than 0.1 g l^{-1}) are only useful for basic research, the cultures in real applications are much more concentrated. Hence, mutual shading exists and the light intensity decreases exponentially from the illuminated surface to the core of the reactor.

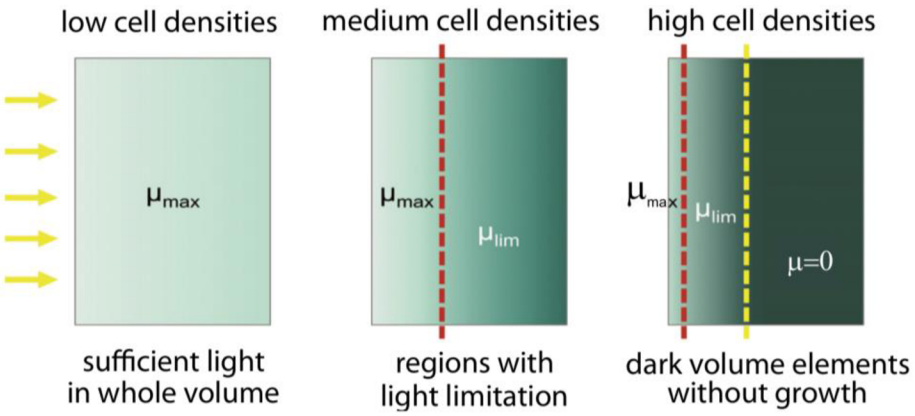

Figure 2.5 Schema of light conditions in a plate photobioreactor illuminated from one side at different cell densities, with μ_{max} maximum growth rate, μ_{lim} light limited growth rate, $\mu=0$ no cell growth (Jacob et al., 2012)

Moreover, the light availability and the light intensity can be impacted by optical properties of reactor walls (e.g., reflectance, refractive index), cell size and pigmentation, and the presence of gas bubbles. Thus, the photosynthesis rate can be expressed as a function of the irradiance to which the cells are exposed. The photosynthesis rate function of the irradiance is in Figure 2.6 where the three irradiance thresholds, the compensation irradiance (Ic), the saturation irradiance (Is) and the inhibition irradiance (Ii), can be culture specific (Acién Fernández et al., 2013).

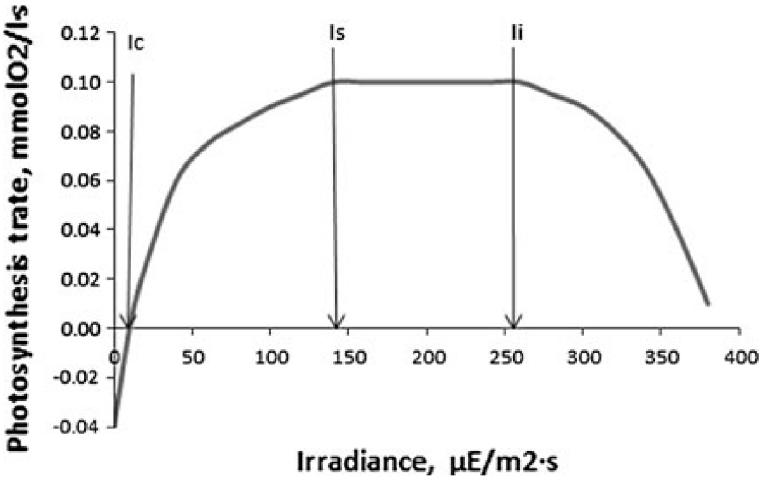

Figure 2.6 Relationship between photosynthesis rate and irradiance in microalgae-thin cultures under continuous light (Acién Fernández et al., 2013)

Numerical simulations of light distribution tend to be computationally intensive. In general, there are two common light modelling approaches: the Beer-Lambert Law model used in, e.g., Zhang et al. (2015), Ali et al. (2019), or Pozzobon and Perré (2020), and the General Radiative Transport Equation model used in, e.g., Soman and Shastri (2015), or McHardy et al. (2018). The Beer-Lambert law model is simple, one-dimensional irradiation model. The model basically relates the attenuation of light to the properties of the material through which the light is travelling. On the other hand, the General Radiative Transport Equation model offers more accurate, three-dimensional solution. The equation can be solved with the Monte Carlo method or a finite volume method, as well. The Monte Carlo method may be favourable for larger photobioreactors but, at the same time, its coupling to a fluid solver is difficult. Therefore, the finite volume method is commonly used, e. g. in Kong and Vigil (2014).

2.6 Biomass Growth

Since the application of CFD analyses to describe biological processes is considered as a less-explored field, the simulation of microalgal growth may be the last step to fully numerically characterize the photobioreactors (Pires et al., 2017). Authors in many

publications with CFD simulations of photobioreactors have usually focused on hydrodynamic factors, such as velocity field and turbulence characteristics. This way, the biomass productivity was estimated indirectly. To directly and quantitatively estimate biomass productivity, a microalgal growth model using culture conditions, such as light intensity, CO_2 concentration, and water temperature, should be adopted in the CFD simulation (Seo et al., 2014). The complexity of such models is therefore obvious. So, it can be expected that the coupling with other computational models, e.g. hydrodynamics, for reactor design and scale-up will be difficult.

The mechanistic growth models can be divided into two categories: physiological models and PSU-based model (Bernardi et al., 2014). The physiological model is extremely complex as it describes the dynamic behaviour of photosynthetic cells and approximates the actual mechanisms involved in the cell's growth. In contrast, photosynthetic unit (PSU) models provide simple systems of differential equations making them easier to couple to a full comprehensive model. The PSU-based model is a state-based model that assumes a hypothetical light-harvesting unit of photosynthesis that, in green plants, comprises about 300 light-absorbing molecules with a molecule of chlorophyll acting as the reaction centre. There are usually three or four states with different transition expressions and theories between them (Gao, 2016).

For instance, the PSU-based Eilers and Peeters model (Eilers and Peeters, 1993) assumes units in three possible states where dark and light reactions are modelled. Figure 2.7 shows how a PSU can travel between the states when it experiences exposure to light. The unit in the resting state x_1 can only go to the active state x_2. Next, the active-state unit can either return to the resting state x_1 and pass down the energy to start the dark phase of photosynthesis or be inhibited by capturing another number of photons and go to the inhibited state x_3. The PSUs in the inhibited state x_3 can eventually recover and go back to the resting state x_1.

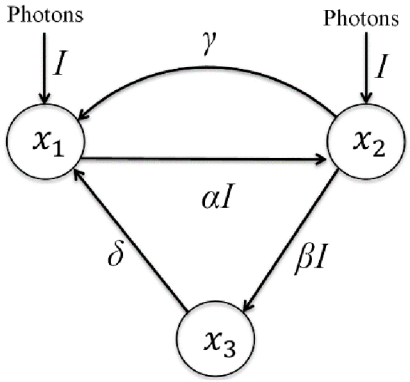

Figure 2.7 Scheme of Eilers-Peeters transition model. x_1, x_2, and x_3 represent the fractions of PSUs in resting, active and inhibited states, respectively (Gao, 2016)

3 Photobioreactors

There are different types of photobioreactors meeting different requirements of any targeted application or operation site. Open-air cultivation systems may offer lower investment and operational costs over the closed photobioreactor technologies when placed in the high solar exposure areas, see Figure 3.1. However, despite the cost of closed cultivation systems, they have major advantages over the open technical systems, e.g. more balanced control over light, temperature, and nutrients (Sukačová et al., 2021). Nevertheless, any cultivation system technology should satisfy following (Singh and Sharma, 2012):

- The reactor should be universal in cultivation of various microalgal species.
- The reactor design must provide uniform illumination of the culture surface.
- The reactor design must prevent or minimize fouling of the reactor since microalgae cells are highly adhesive to walls, particularly of its light transmitting surfaces.
- Targeting high mass transfer rates must not be at the expense of culture damage or growth suppression.
- The reactor should have minimum non-illuminated parts.

Figure 3.1 Open pond at Hamburg-Reitbrook, Germany (ABiRe, 2022)

Following text presents two photobioreactor types, the flat-panel photobioreactor and the tubular photobioreactor. These vessels were used for work in this dissertation thesis and were placed at the Institute of Process Engineering at Faculty of Mechanical Engineering at Brno University of Technology. The reader is recommended to see, e.g., Posten (2009), Singh and Sharma (2012), or Acién Fernández et al. (2013) for details about other cultivation technologies.

3.1 Flat-Panel Photobioreactor

The hydrodynamic model assessment was performed on the lab-scale cuvette of the photobioreactor shown in Figure 3.2. This cuvette was of a stirred flat-panel type with dimensions in Figure 3.3. The water free surface reached the height of 166 mm.

Figure 3.2 Photobioreactor FMT 150 (PSI, 2021)

Its interior was equipped with a U-shaped stainless-steel aerator tube, Teflon-coated stir bar, and two Ø 12 mm probes, a pH probe and a temperature probe. The U-shaped aerator tube delivered air near the cuvette bottom through four Ø 0.7 mm holes. The stir bar was

of a magnetic type and was placed at the front glass panel inside the vessel. There was no shaft that would introduce some features to the cuvette's glass panels so it could be easily exchanged or removed. Possible rotational speeds for the motor were between 120 and 600 revolutions per minute (rpm) yielding the Reynolds number in the range of 5,000 and 25,000, respectively. In addition to the temperature probe, the temperature could be controlled by a Peltier cell in the cuvette's base and the back wall could be lit with a LED array, see Figure 3.4 for the detail.

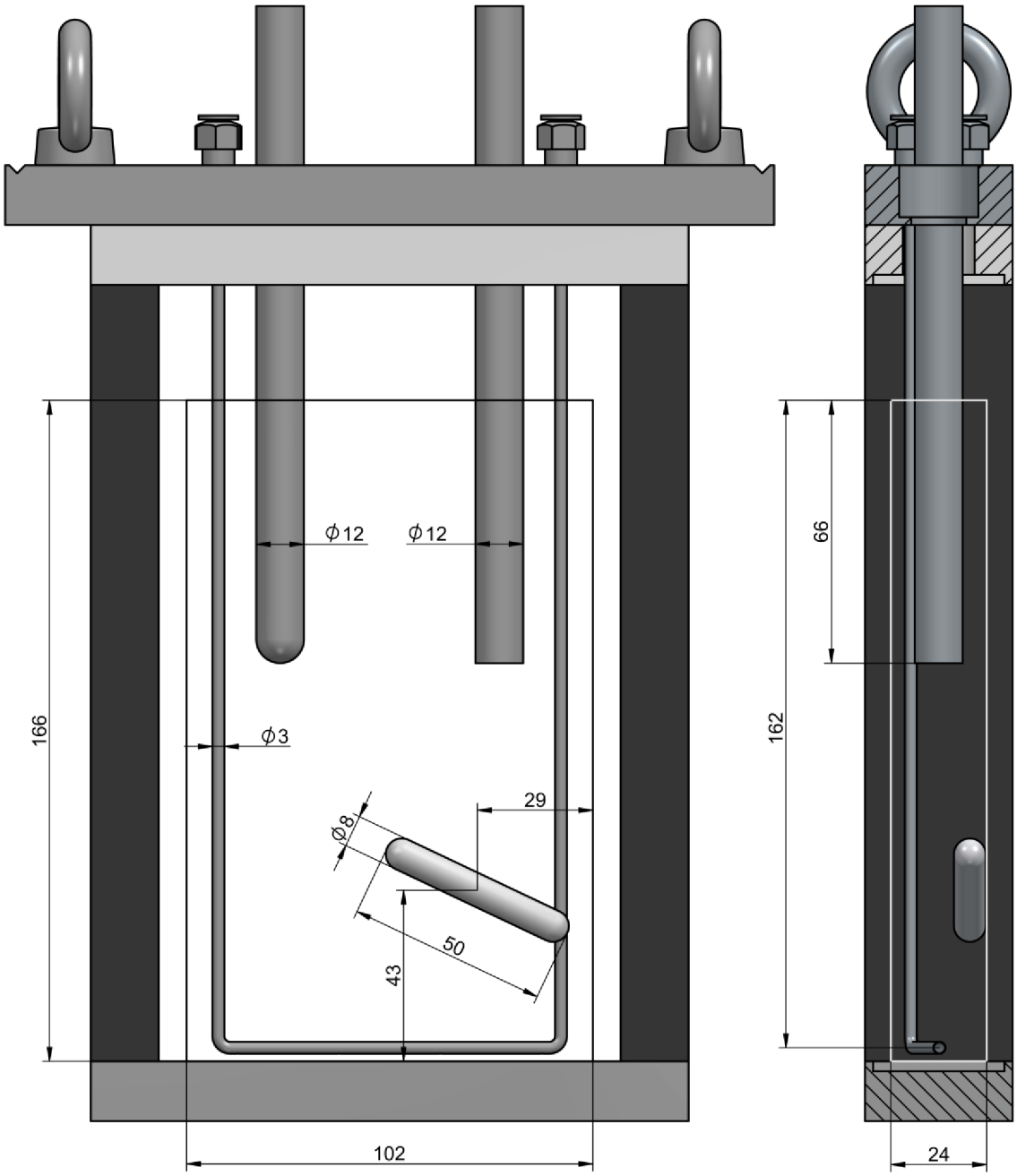

Figure 3.3 Orthographic view of the cuvette within its frame and with dimensions (in mm). The figure does not show glass panels. The rectangle marks its inner volume instead where the its height is limited to the water free surface.

Figure 3.4 Cuvette illuminated from the back with a white LED array (PSI, 2021)

The aeration gas flow through the cuvette was controlled by a flow controller and could reach up to 300 ml min^{-1} where the aeration gas was air enriched by 3 % CO_2. As shown in Figure 3.5, the flow of both phases inside this type of photobioreactor was affected by the stirrer and/or air sparging. The figure shows three flow snapshots in the cuvette, without agitation, with the minimal agitational speed (120 rpm), and with the maximal agitational speed (600 rpm). The stirrer-induced agitation formed the most intensive flow patterns that were able to break bubbles. Under non-agitated conditions, i.e., in a bubble rising regime, the bubbles could be as large as 5 mm in diameter and mostly of ellipsoid shape. This shape was also dominant under the low agitation speeds. At higher revolutions per minute, bubbles were broken down by the stirrer and appeared to be of a spherical shape.

In addition to the aeration, the cuvette could be irradiated with a LED array, as well. To study the cyanobacterial growth with dynamically induced state transitions, four blue LEDs interlaced with four orange LEDs arranged together into twelve rows could be used. To study photoinhibition, on the other hand, a panel of white LEDs could be used. Some additional information about the photobioreactor can be found in Nedbal et al. (2008) or PSI (2021).

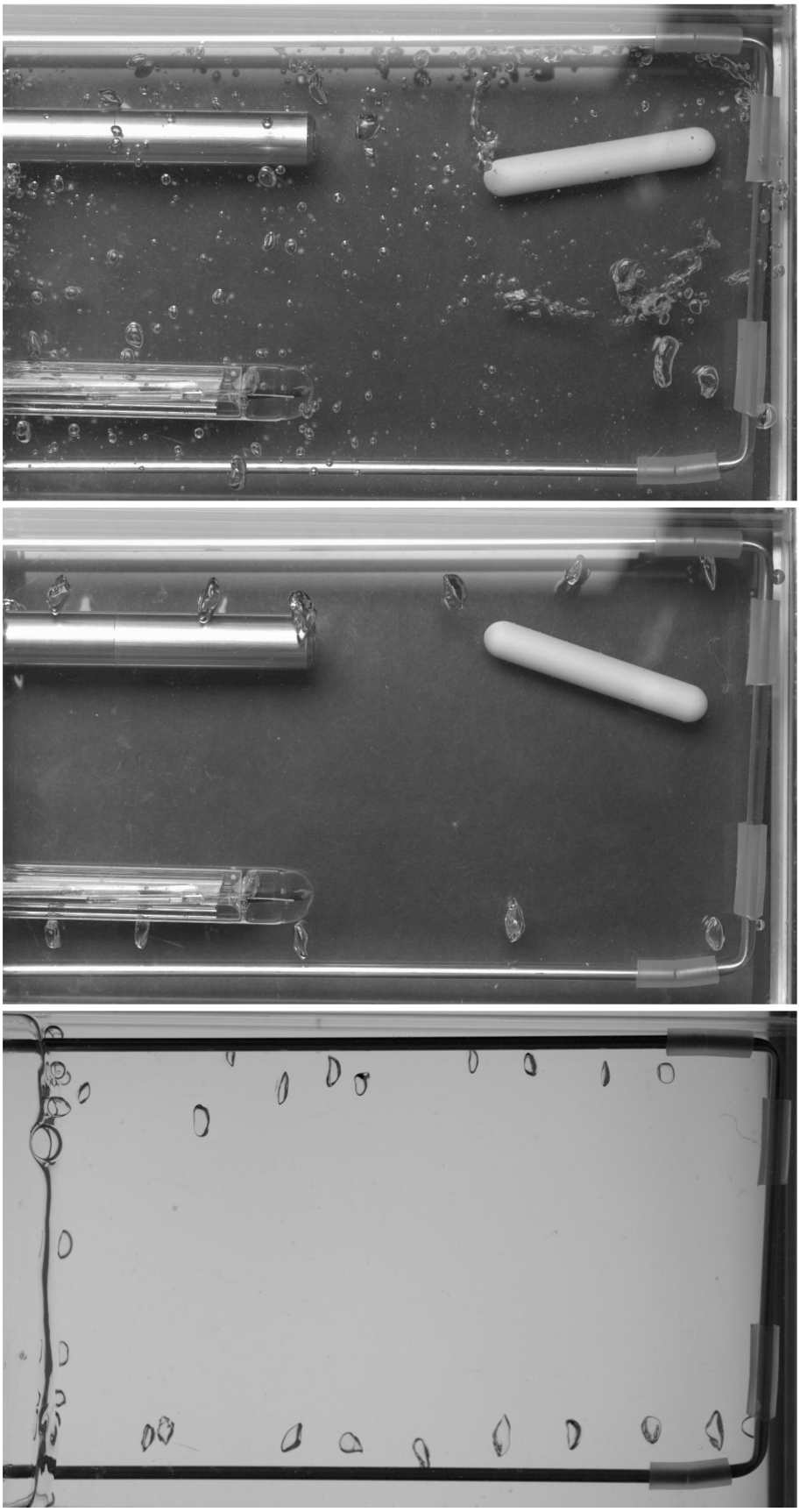

Figure 3.5 Snapshots of bubble sizes and shapes during operation
a) no agitation, b) 120 rpm, c) 600 rpm

3.2 Tubular Photobioreactor

For preliminary analyses of the mass transfer phenomena in photobioreactors, the vertical bubble-column cultivation system was used, see Figure 3.6. In this cultivation system, there were three main parts:

- two gas storage tanks,
- a buffer tank,
- three vertical tubes.

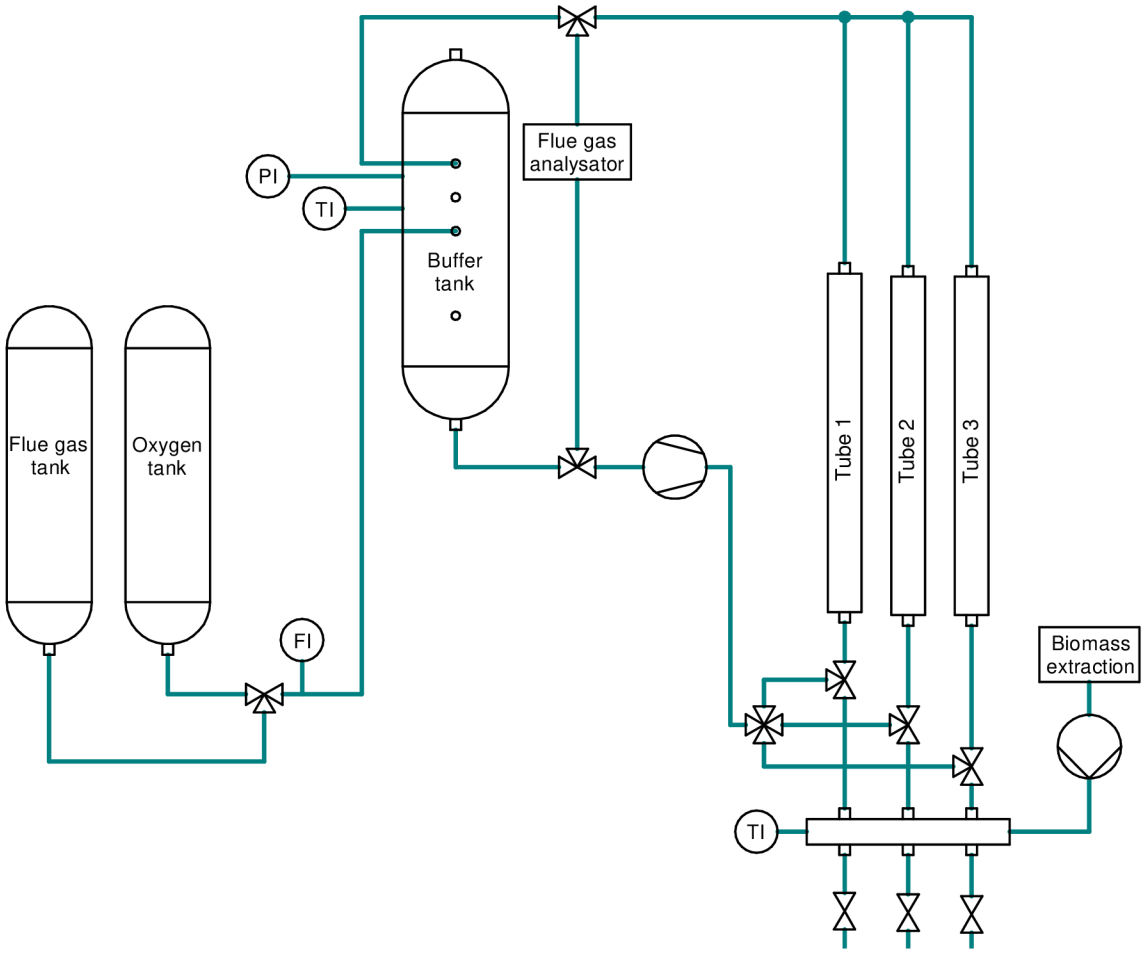

Figure 3.6 Schematic of the vertical buble-column cultivation system

The reactor vessel itself was made from three vertical tubes with a rectangular cross-section of dimensions 44x20 mm and rounded corners with 10 mm radius, see Figure 3.7 (left). The tubes were filled with 4.34 litres of water. In total, 105 litres of the aeration gas were fed to the reactor's loop from storage tanks with composition presented in Table 3.1. The cultivation medium in the reactor's tubes was aerated with the constant total airflow rate of 2 l min^{-1} at 165 mbar from the bottom of the tubes through the perforated inlet membrane. The airflow rate yielded the superficial velocity of 0.013 m s^{-1} placing the bubbly flow into the homogeneous regime (Joshi, 2001) with bubbles uniformly sized and dispersed, see Figure 3.7 (right).

Table 3.1 Aeration gas composition

Species	Amount
SO_2	50 $mg\ m_N^{-3}$
CO	50 $mg\ m_N^{-3}$
NO	200 $mg\ m_N^{-3}$
O_2	9 $\%_{vol.}$
CO_2	10 $\%_{vol.}$
N_2	81 $\%_{vol.}$

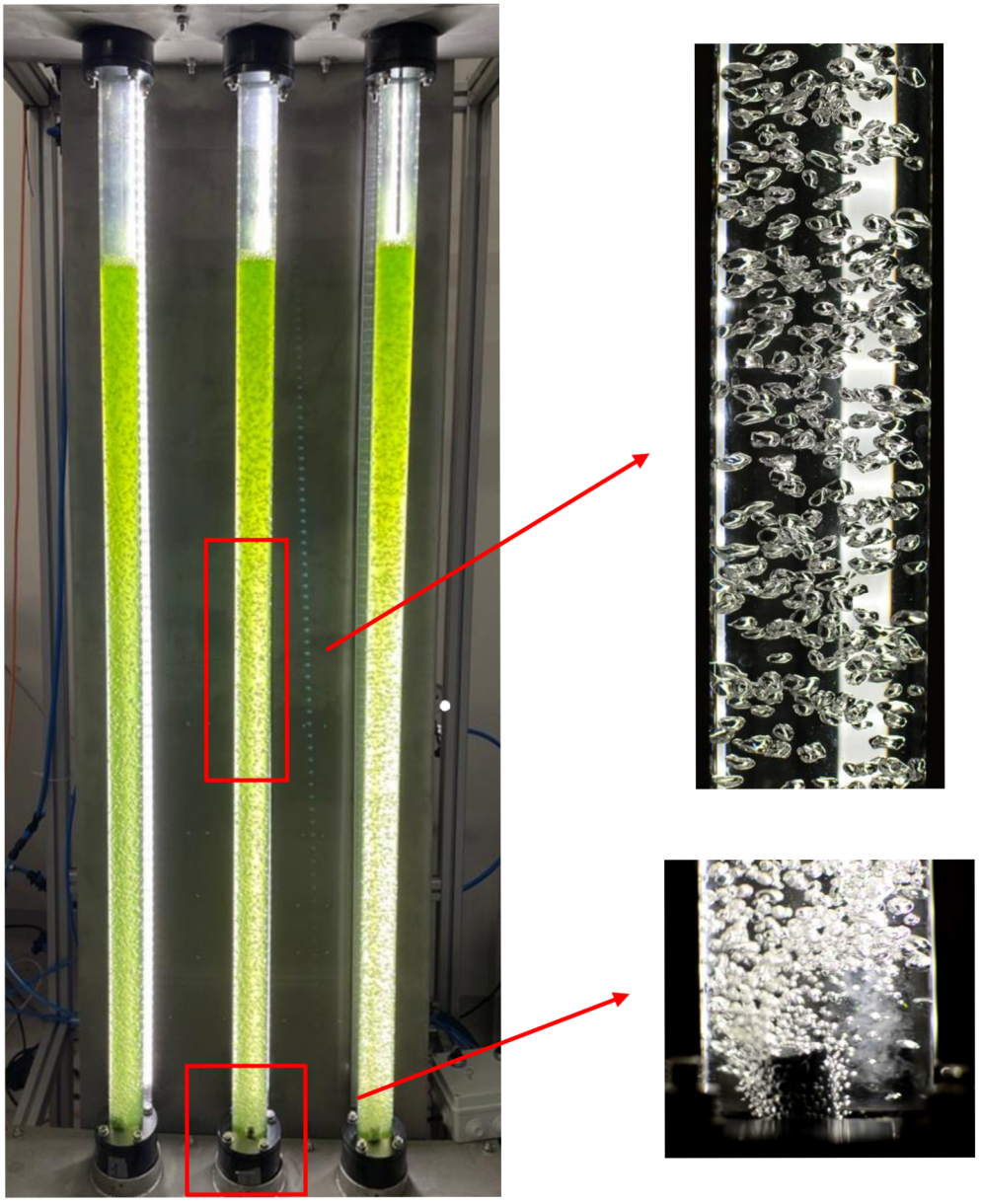

Figure 3.7 Aeration gas dispersed in the tubular photobioreactor;
tubular photobioreactor (left), mid-height (top right) and inlet section (bottom right)

4 Hydrodynamic Model

This chapter presents the hydrodynamic model used in the lab-scale cuvette. It describes the experimental methods used for flow measurements in the laboratory, the numerical model for computer simulations, and results of both scientific methods. However, preceding to any experiments and simulations, physical phenomena of the interest must be understood with regards to the time scale, spatial scale, and other specifics so that the numerical model is well-posed (Moukalled et al., 2016). This includes, e.g., mean bubble size, bubble behaviour due to sparging, or mixing time constants. For this reason, a number of laboratory observations and test simulations were done prior to planning the experiments and developing the numerical model.

Time constant for flow development was found with a single-phase CFD simulations of agitated water where the liquid velocity was monitored in selected points, see Figure 4.1a. Time constant for homogenisation, on the other hand, was found with an arbitrary trace pulse put into specific place in the domain and measuring the time required to achieve a specific degree of homogeneity, see Figure 4.1b.

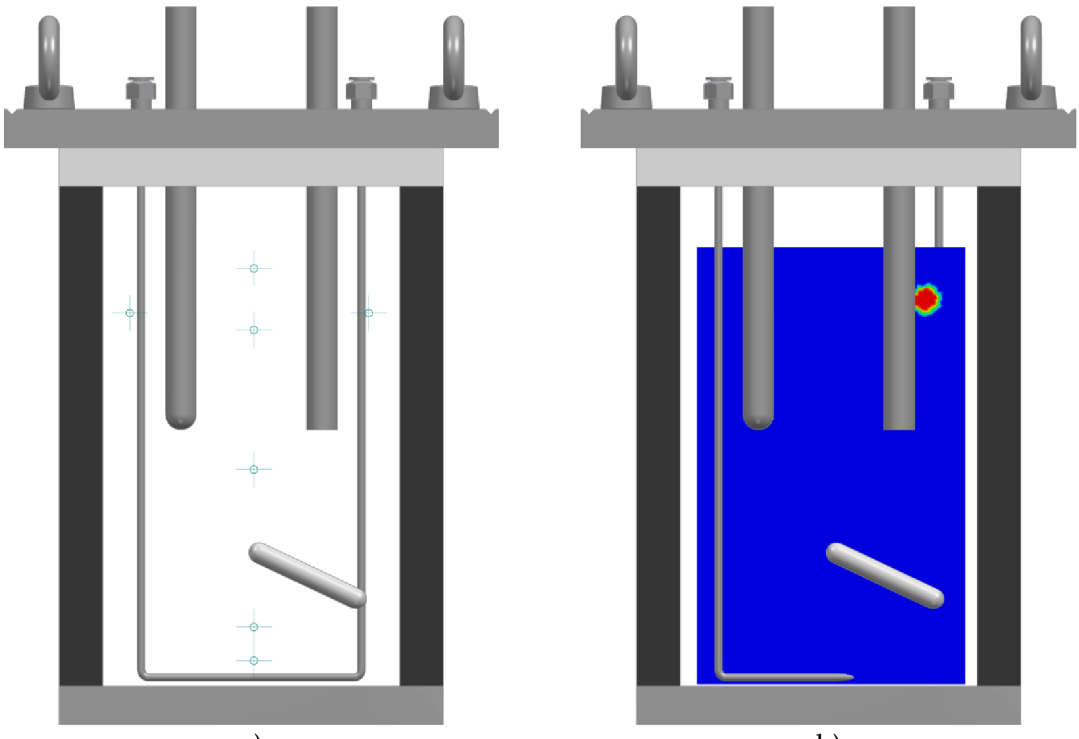

a) b)

Figure 4.1 a) Position of monitoring poins, b) Example of tracer position

This way, the secondary phase did not model a real mixture of liquids. The pulse was used for tracing purposes only, i.e., to measure time of convective homogenization. This procedure was repeated several times with different placements and with different agitation speeds. It led to a conclusion that it takes up to 10 seconds to develop flow patterns and to reach the homogeneous mixture, see Figure 4.2 and Figure 4.3. Similar results were observed with the cuvette in the laboratory. These findings were then considered for planning experiments and numerical simulations.

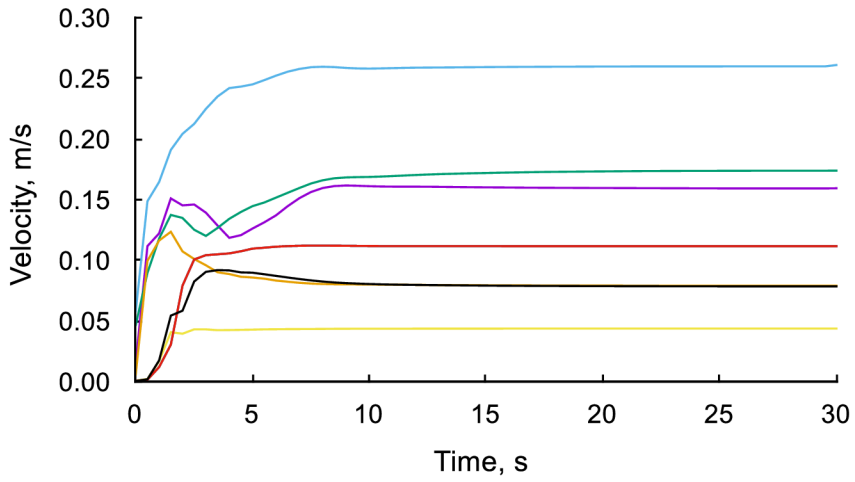

Figure 4.2 Flow development at 360 rpm

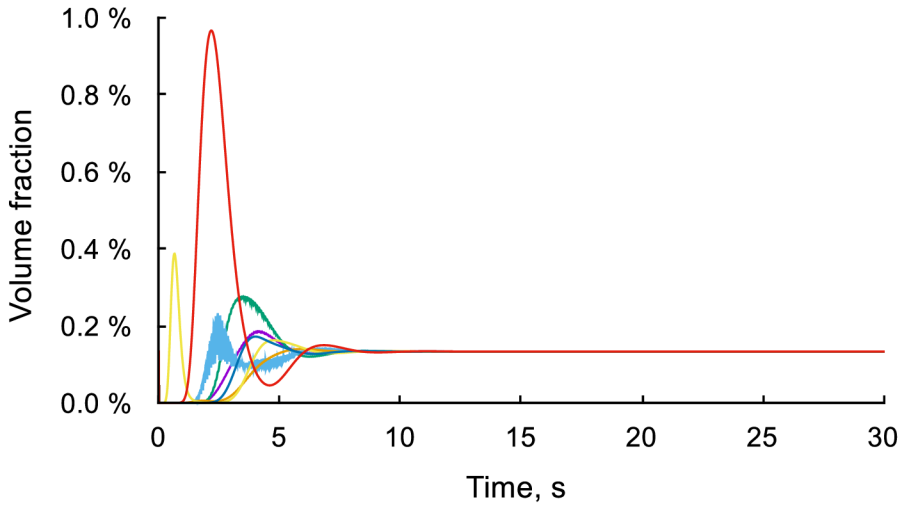

Figure 4.3 Flow homogenization at 360 rpm

The spatial scale for the numerical model was drawn from the Courant, Friedrichs, and Lewy (CFL) condition (Courant et al., 1928), and general recommendations found in the ANSYS Inc. (2020b). Details about time step size and mesh resolution are presented in following text. Inlet boundary condition and its effect on the formation of bubbles were studied in Rebej et al. (2021).

At first, the experimental method is presented with its setup and results. Next, the hydrodynamic multiphase numerical model is introduced with its results presented comparably to the experiments. The model is followed by an additional shear stress analysis. At last, a critical summary is given at the end of the chapter.

4.1 Experimental Work

There are various methods available for fluid flow measurement and validation of numerical simulations. The Particle Image Velocimetry (PIV) may be the most common method for measuring and visualizing fluid flow. In general, it is an optical method that uses tracer particles that follow the fluid flow. These particles are illuminated with a laser and tracked with a camera. As a result, this method can produce two- or three-dimensional velocity vector fields of these particles in motion. See Figure 4.4 for an experimental arrangement of a planar PIV measurement. The application of the PIV method to study other multiphase flows can be found, e.g., in Wu and Merchuk (2003), Liu et al. (2005), Dijkhuizen et al. (2010), or Murgan et al. (2017).

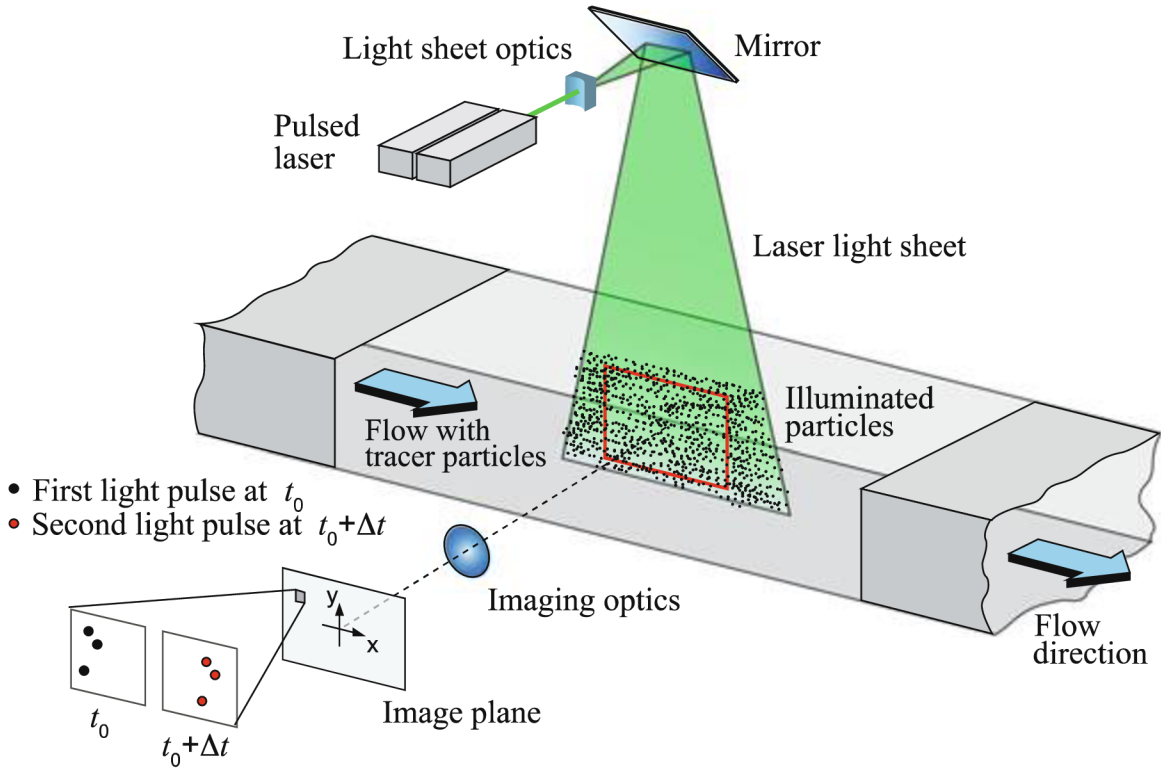

Figure 4.4 A typical setup for PIV recording of two velocity components. Illustration shows the flow field on a laser plane in a wind tunnel (Raffel et al., 2018)

In contrast to PIV, other available methods measure the fluid velocity at a specific point. These methods may include the Acoustic Doppler Velocimetry (ADV) or the Laser Doppler Anemometry (LDA). Compared to the ADV, LDA or other in-situ method with sensors, the PIV may be more suitable method to measure fluid dynamics since it does not bring any probe that could directly interfere with the flow patterns. Moreover, when applied to multiphase or bubbly flows, results from PIV measurements can include bubble rising velocity and induced flow structure, the bubble diameter variation, the interfacial area, and the bubble shape factor (Liu et al., 2005; Murgan et al., 2017).

4.1.1 Experimental Setup

The PIV system by Dantec Dynamics at the Technical University of Liberec was used for velocity measurements. The system consisted of a NewWave Gemini pulsed laser with 10 ns pulse length and frequency of 532 Hz. The images were captured by 5.5 Mpx Dantec Neo camera with a 50 mm focal length lens and 500 frames per second shutter speed.

The experimental setup with the cuvette is in Figure 4.5. The velocity field was measured in a vertical plane through the centre of the cuvette. However, in case of two-phase flow measurement without agitation, the cuvette was equipped only with the U-shaped aerator tube. In case of other measurements, the cuvette was fully equipped and in order to eliminate shadows from the suspended probes, the laser beam had to be split to form two coplanar laser planes. This setup then resulted in an inability to measure the region between the probes. Therefore, the data from this part were not used for the flow validation.

The water was seeded with 20 μm polyamide particles coated with a rhodamine layer. Reflection of light from the walls and accessories was eliminated using optical filters suitable for the wavelength emitted by the particles. Post-processing of the data was performed in the Dynamic Studio software. This included cross-correlation algorithms for the computation of velocity vector maps. Additionally, bubble rising velocities were calculated by tracking bubbles in digital images taken by the high-speed camera.

Depending on the operational regime, fluid flow inside the cuvette was a combination of forced agitation with the stirrer and/or flow induction from bubbles. Therefore, to measure the fluid flow, following step-by-step analysis was performed:

- Two-phase flow measurement with flow induced by bubbles only
  - Figure 4.6
- Single-phase flow measurement with flow induced by stirrer only
  - Figure 4.7 and Figure 4.8
- Two-phase flow measurement with flow induced by stirrer and bubbles
  - Figure 4.9 and Figure 4.10

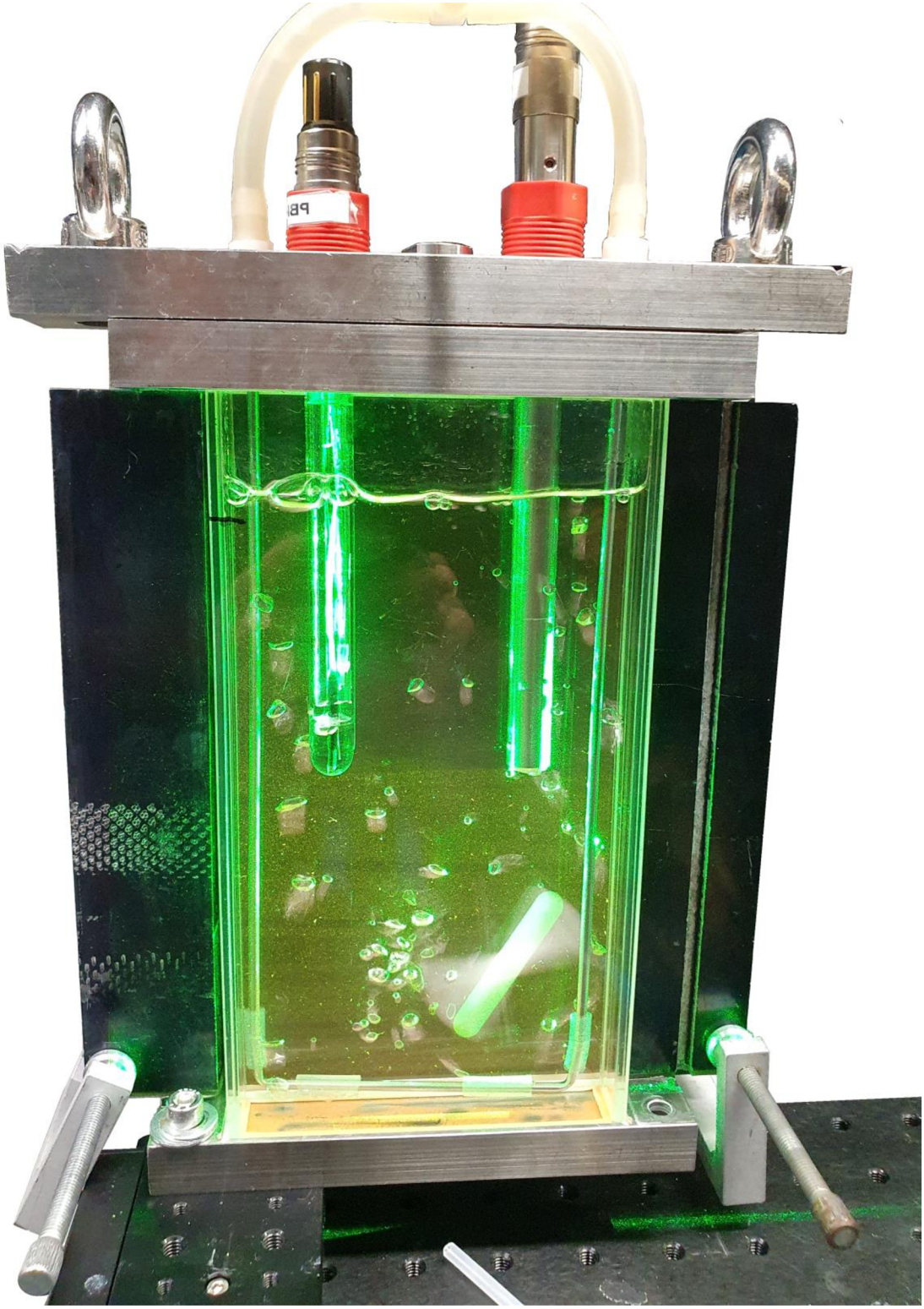

Figure 4.5 Experimental PIV setup – cuvette filled with water is aerated, agitated, and lit with laser planes.

4.1.2 Results

Two-phase flow measurement with flow induced by bubbles only

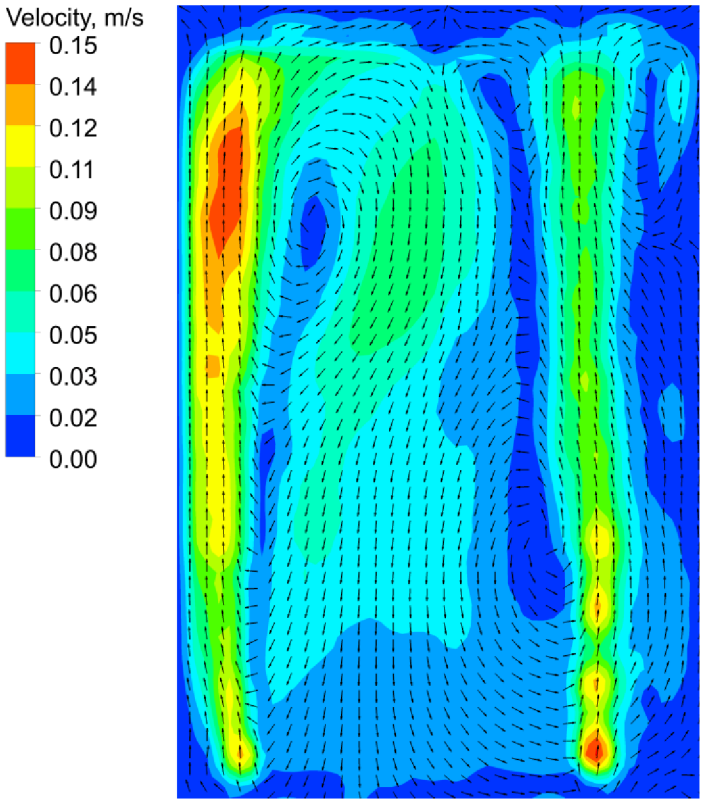

Figure 4.6 Velocity contour from PIV with 200 ml min^{-1} aeration rate and no agitation

In addition to PIV measurement of the liquid phase, measurements on the secondary phase were done by tracking bubbles with a high-speed camera, as well. Air flow rate of 200 ml min^{-1} was found to yield the 0.22 m s^{-1} bubble rising velocity. Considering the velocity field in Figure 4.6, the water in main streams is accelerated closely to this bubble velocity. Table 4.1 gives respective dimensional numbers for this type of the flow. Comparing it with the Grace diagram in Figure 2.1, the diagram predicts bubbles of wobbly-ellipsoidal shape. This is also in accordance with the Figure 3.5a.

Table 4.1 Dimensional numbers for two-phase flow without agitation

Eo	*Re*	*Mo*
1,7	766	2,7e-11

Single-phase flow measurement with flow induced by stirrer only

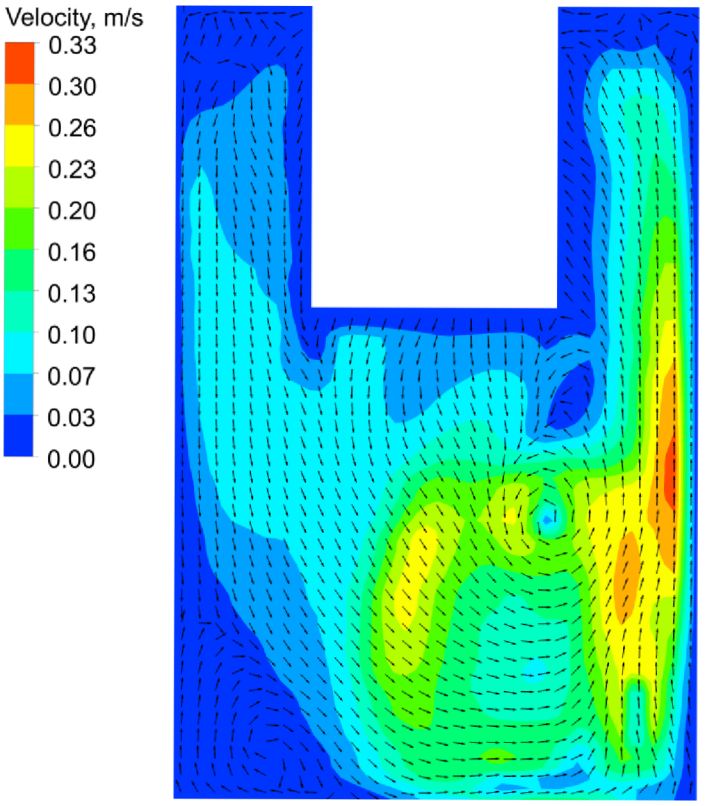

Figure 4.7 Velocity contour from PIV with no aeration at 360 rpm

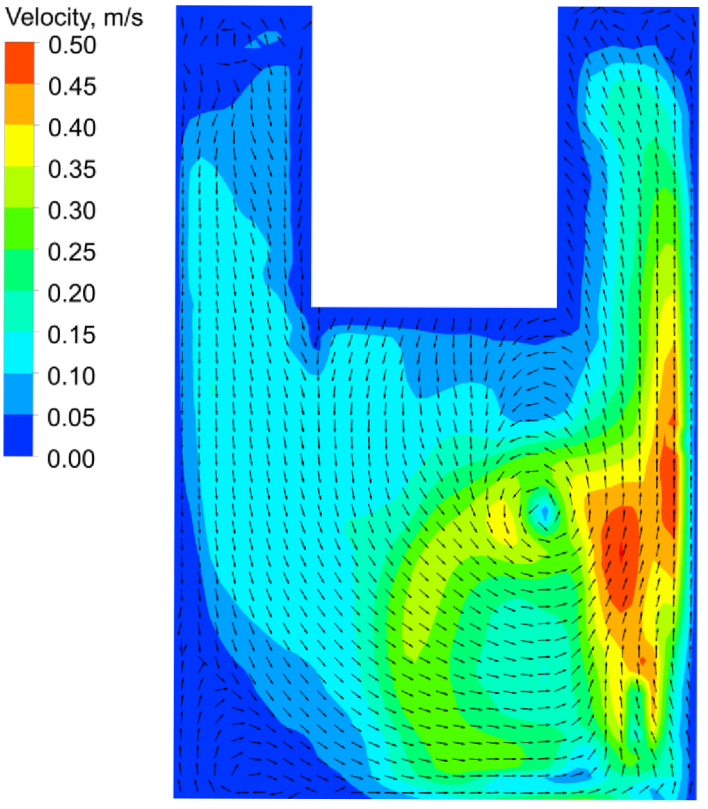

Figure 4.8 Velocity contour from PIV with no aeration at 480 rpm

Two-phase flow measurement with flow induced by stirrer and bubbles

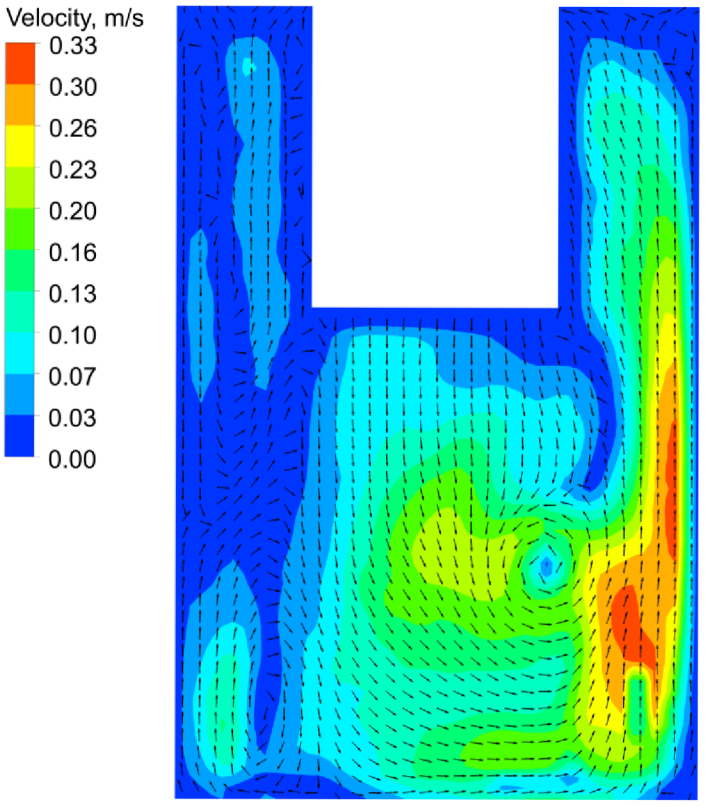

Figure 4.9 Velocity contour from PIV with 200 ml min^{-1} aeration rate at 360 rpm

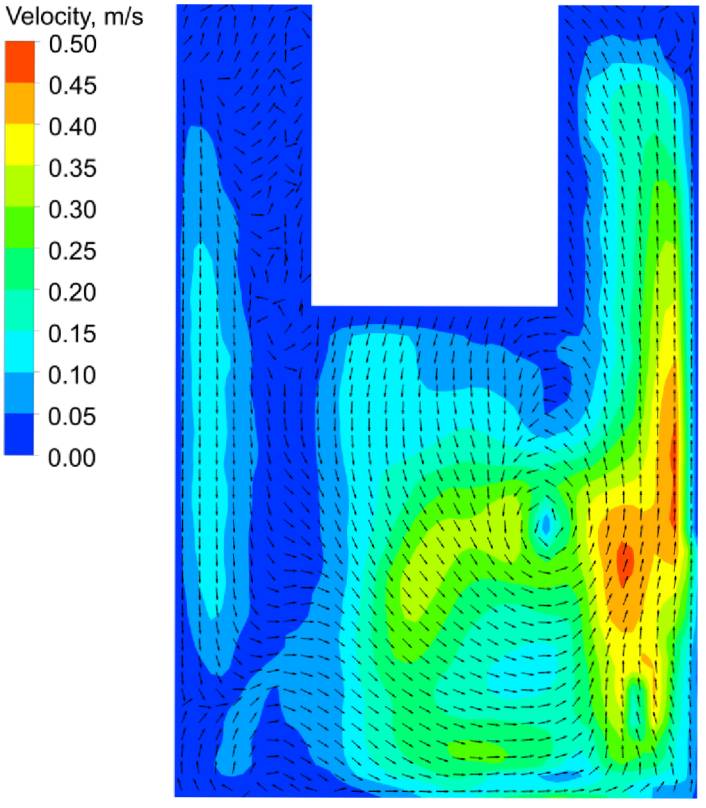

Figure 4.10 Velocity contour from PIV with 200 ml min^{-1} aeration rate at 480 rpm

4.2 Numerical Simulations

The computational domain used in numerical analysis resembles inner volume of the cuvette, as illustrated in Figure 3.3. Its 3D geometry is created in the ANSYS SpaceClaim and is divided into two main zones, stator and rotor. Numerical model is based on the literature research presented in Chapter 2.2 and author's test analyses introduced at the beginning of the chapter. Final setup is described in following text.

4.2.1 Numerical Model Setup

The CFD model was based on the two-fluid approach within Eulerian–Eulerian (E-E) framework with constitutive closures for interphase forces and liquid turbulence. The two-fluid environment was made from the liquid water and the gaseous air. Since the photobioreactor was generally operated at 20 °C, the corresponding values of material properties used in numerical simulations were the default values in the ANSYS Fluent, i.e., 998.2 kg m^{-3} in density and 1.003 mPa·s in viscosity for the liquid water, and 1.225 kg m^{-3} in density and 0.0179 mPa·s in viscosity for the injected gaseous air. The air-water surface tension is 0.072 N m^{-1}.

All phases combined in the E-E framework formed interpenetrating continua where the amount of each phase was determined by the volume fraction. The framework used a single pressure field that was shared among all phases. Momentum equations were calculated for the continuous and every dispersed phase separately, i.e., each phase had its own velocity field. Moreover, the turbulence was modelled in all simulations. Since the k-ε family of turbulence models was used the most often in simulations of photobioreactors (Table 2.2), its latest modification known as the Realizable k-ε Turbulence Model together with the Enhanced Wall Treatment was also considered in this work. Regarding the multiphase character of the flow and low gas volume fraction (ca. 0.6 %), the dispersed formulation of the turbulence model was employed, i.e., only the turbulence for the continuous phase was modelled. Turbulence modelling on the dispersed-phase side was possible with turbulence interaction terms. However, this possibility was often not considered (see Table 2.2) as it might not been an important phenomena and it could even cause a difficulty in convergence (ANSYS Inc., 2020b).

Regarding the phase interaction models, only the drag force modelling was included. The Grace drag model was selected as it is recommended for bubbles that can have different sizes and shapes (ANSYS Inc., 2020a). The applicability of suitable drag models was studied in Rebej et al. (2020). Other interaction models, e.g., lift force or virtual mass force, were not considered in simulations. The effect of such models was not found to bring any improvements in results. Moreover, the convergence and numerical stability was negatively affected. Also, as shown in the Table 2.2, necessity to implement these models is questioned among authors.

Nevertheless, the numerical model used the Phase Coupled SIMPLE algorithm to couple the phasic momentum equations, the continuity equation, and the phasic volume fraction equations. The spatial discretization for pressure field was employed with the Body Force Weighted scheme and the First Order Upwind scheme for the volume fraction equation. Other variables used the Second Order Upwind scheme. All numerical analyses were solved in the transient solver. Convergence was considered on the basis of residuals, levels below 10^{-3} were required. The time-step size varied between different sets of analyses. For simulations with only water agitation, the timestep size of 0.001 s was used. Other multiphase cases used the timestep size of 10^{-4} s.

In terms of operating conditions, the effect of the gravitational acceleration was included in the model. Moreover, to capture the buoyancy of the gaseous phase, the operating density was set to the density of air with the operating pressure of 101,325 Pa at the water free surface, i.e., top of the domain. This surface was treated as the degassing boundary condition, i.e., free-slip wall for the primary phase and the mass-sink for the secondary phase. The interface corresponding to the stationary and rotational zone was treated as the interior boundary. All other walls in the domain had the no-slip boundary condition. The treatment of the gas inlet condition was modelled with the mass-source term in the dedicated cell zones representing the inlet orifices. The cell zones were of the spherical shape with the same diameter as the real-world inlet orifices, i.e., 0.7 mm. The air flow-rate through the photobioreactor was 200 ml min^{-1}.

In total, there were three types of computational meshes analysed, different in the level of refinement. Their details are presented in Table 4.2. The relative cumulative frequency of y+ for the worst-case scenario (480 rpm), is in presented the Figure 4.11.

Table 4.2 Computational mesh types

Mesh	Boundary layers	Max. cell's edge size	Number of cells
Coarse	5 layers at stirrer	3.3 mm	Approx. 200k
Medium	5 layers at all walls	1.8 mm	Approx. 450k
Fine	15 layers on the stirrer 10 layers on other walls	1.3 mm	Approx. 1.1M

Numerical analyses followed the same step-by-step analysis as in the experimental flow measurement, see Chapter 4.1. The analyses of the single-phase flow induced by the rotating stirrer were carried out in two stages. In the first stage, there were 20,000 time-steps calculated yielding the end flow-time 20 s. The second stage continued with the same time-step size, but the data time-averaging was included for further post-processing. There were additional 10,000 time-steps calculated yielding the end flow-time 30 s. The duration of the first stage allowed the flow inside the cuvette to develop,

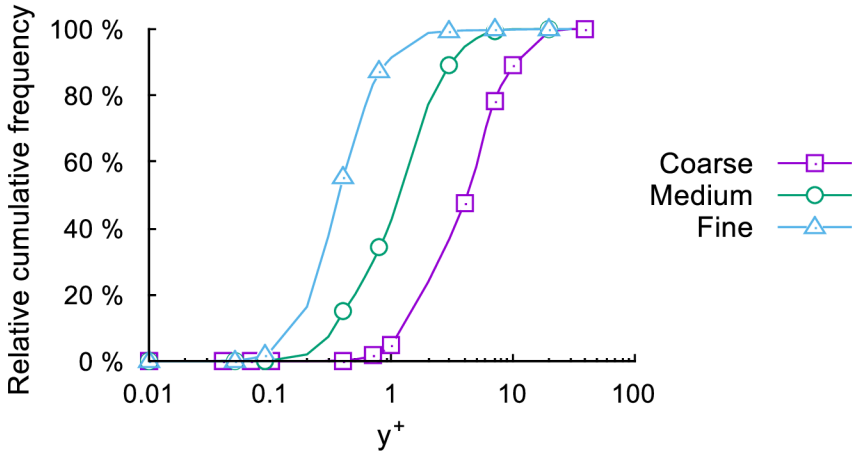

Figure 4.11 The relative cumulative frequency of y+ at 480 rpm

i.e., monitored velocities reached the stabilised value. Therefore, the data time-averaging was not affected by the initial state and inherent flow instabilities. This is presented in Figure 4.14 and Figure 4.15 in the following sub-chapter 4.2.2.

The two-phase flow analyses where the flow was induced by the stirrer and bubbles proceeded from the first stage of the respective single-phase analyses at the flow-time 20 s. At this point, flow patterns in water had already been formed and stabilised, so that the aeration of the cuvette could begin. Again, for these multi-phase analyses, additional 10,000 time-steps but with the time-step size of 10^{-4} s were calculated. In contrast to that, the two-phase flow analysis with the fluid flow induced by bubbles only started with the quiescent water, i.e., flow-time of 0 s. There were 5 s of flow-time calculated.

4.2.2 Results

Similarly to the experiments, numerical results were analysed in the vertical plane centred in the cuvette and analyses followed the same procedure as presented in the Chapter 4.1. At first, following text presents the results by means of velocity contours and plots for the two-phase flow simulations with flow induced by bubbles only, next it is the single-phase flow with agitation only, and at last, it is the two-phase flow with agitation and aeration.

Two-phase flow simulations with flow induced by bubbles only

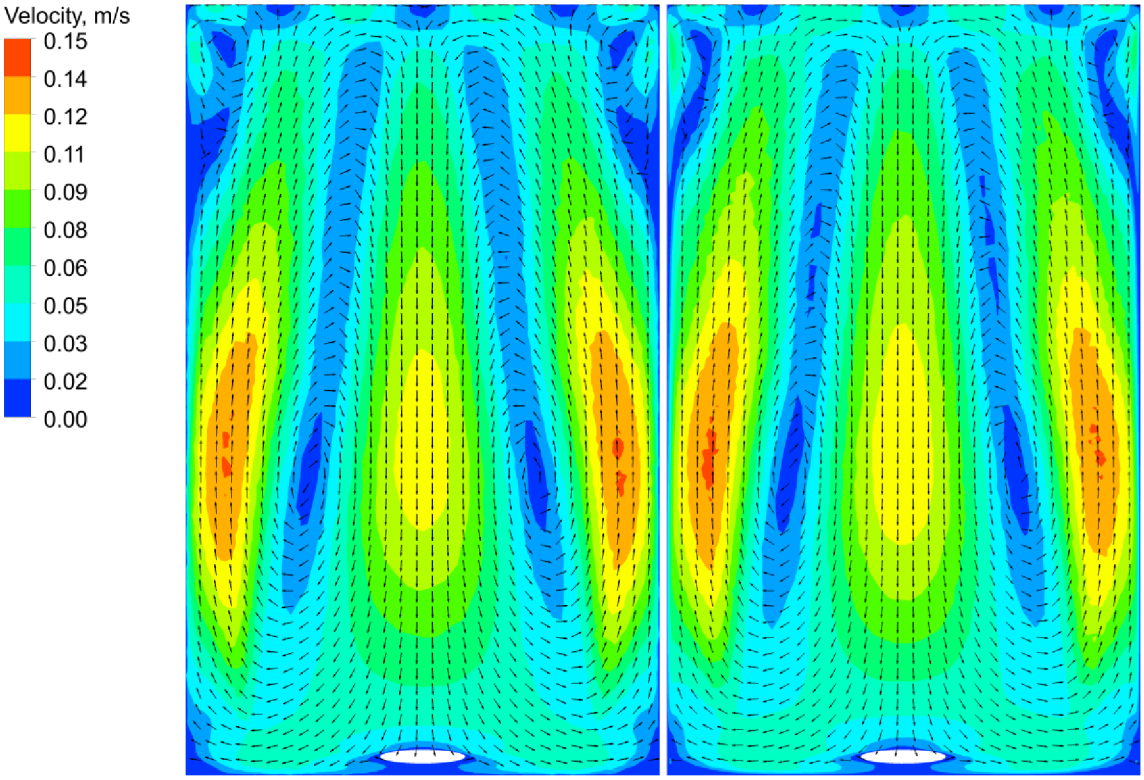

Figure 4.12 Velocity contours from CFD with 200 ml min^{-1} aeration rate and no agitation
left: coarse mesh, right: medium mesh

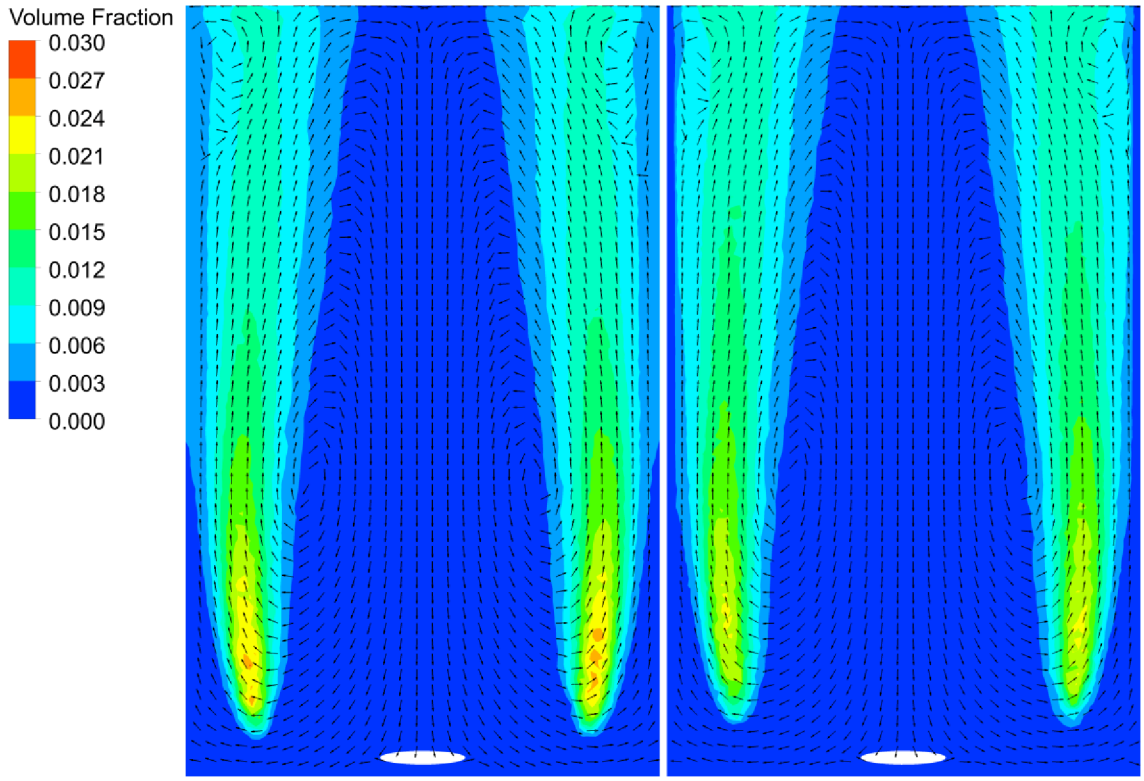

Figure 4.13 Secondary phase volume fraction contorus from CFD with 200 ml min^{-1} aeration rate and no agitation
left: coarse mesh, right: medium mesh

Single-phase flow simulations with flow induced by stirrer only

Figure 4.14 and Figure 4.15 show velocities in various monitoring points. See Figure 4.1a for their position inside the domain. From these figures, it can be observed that the flow has reached its stabilised state. The two stages for simulations of the single-phase flow are distinguished with colours. The green colour marks the data time-averaging period.

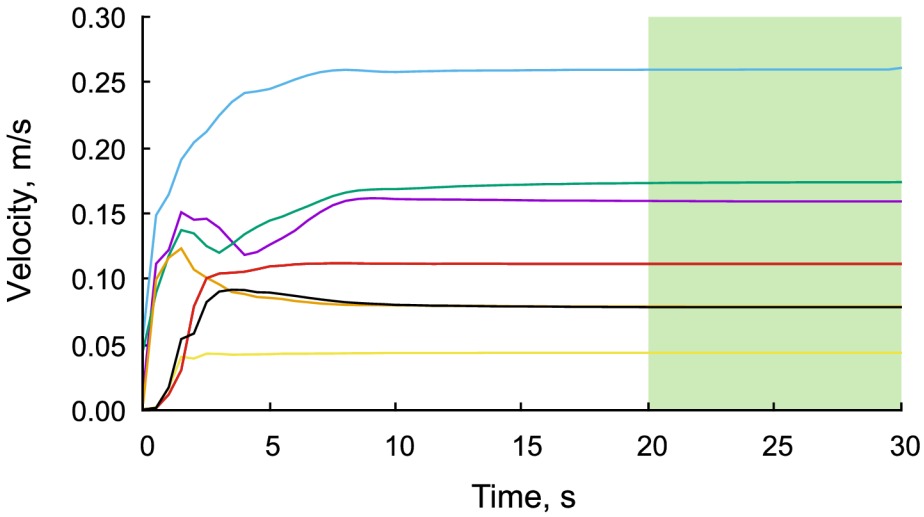

Figure 4.14 Velocity profile from monitoring points inside the domain, 360 rpm and no aeration

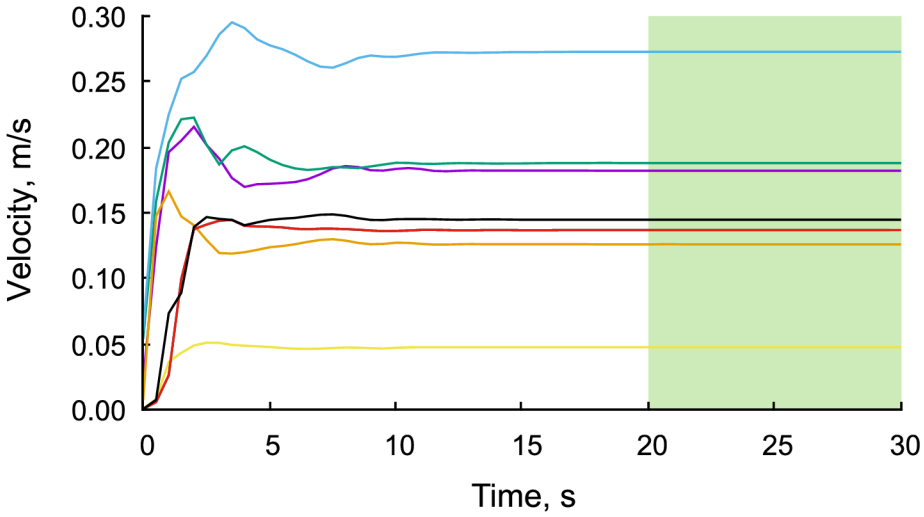

Figure 4.15 Velocity profile from monitoring points inside the domain, 480 rpm and no aeration

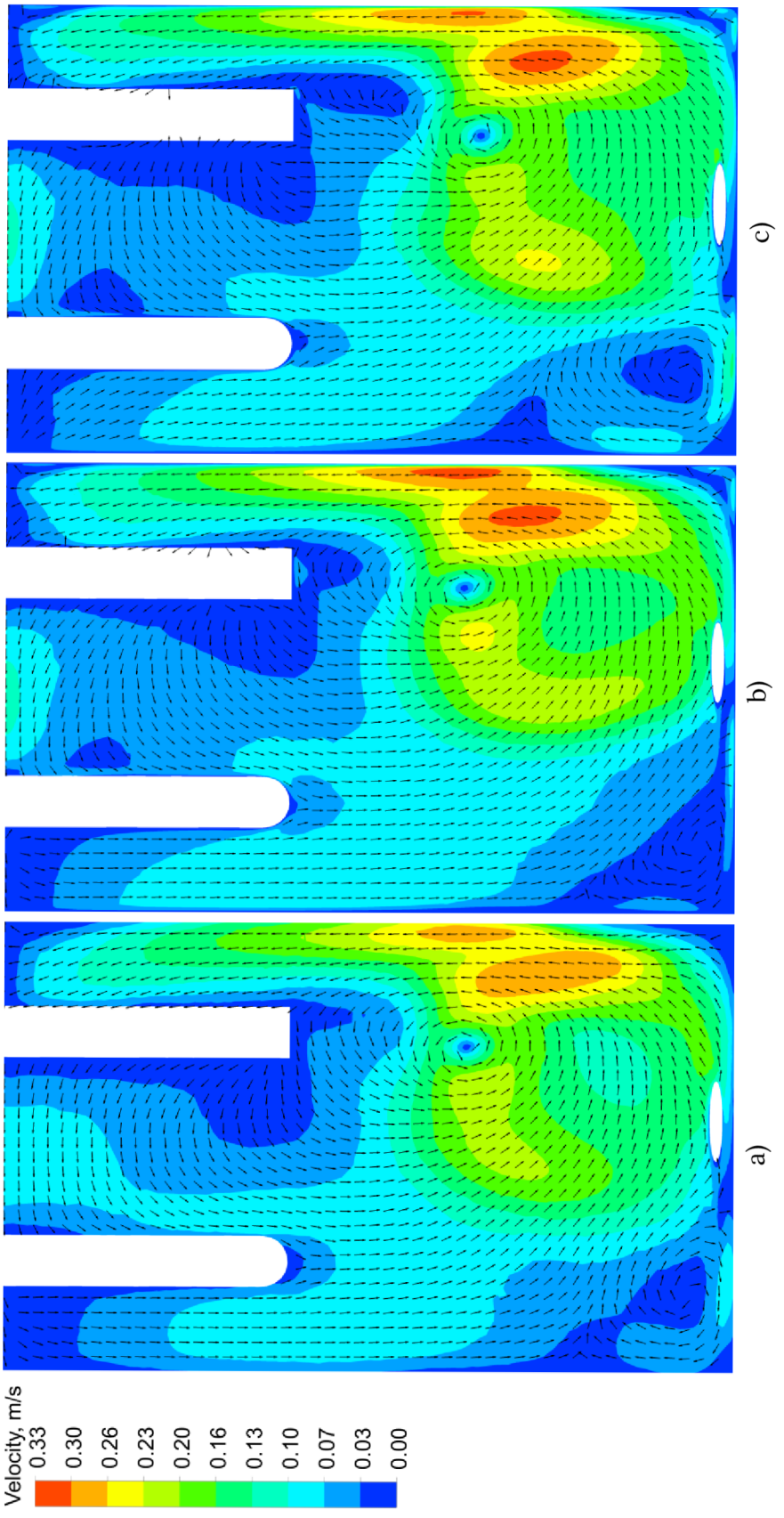

Figure 4.16 Velocity contours from CFD with no aeration at 360 rpm
a) coarse mesh, b) medium mesh, c) fine mesh

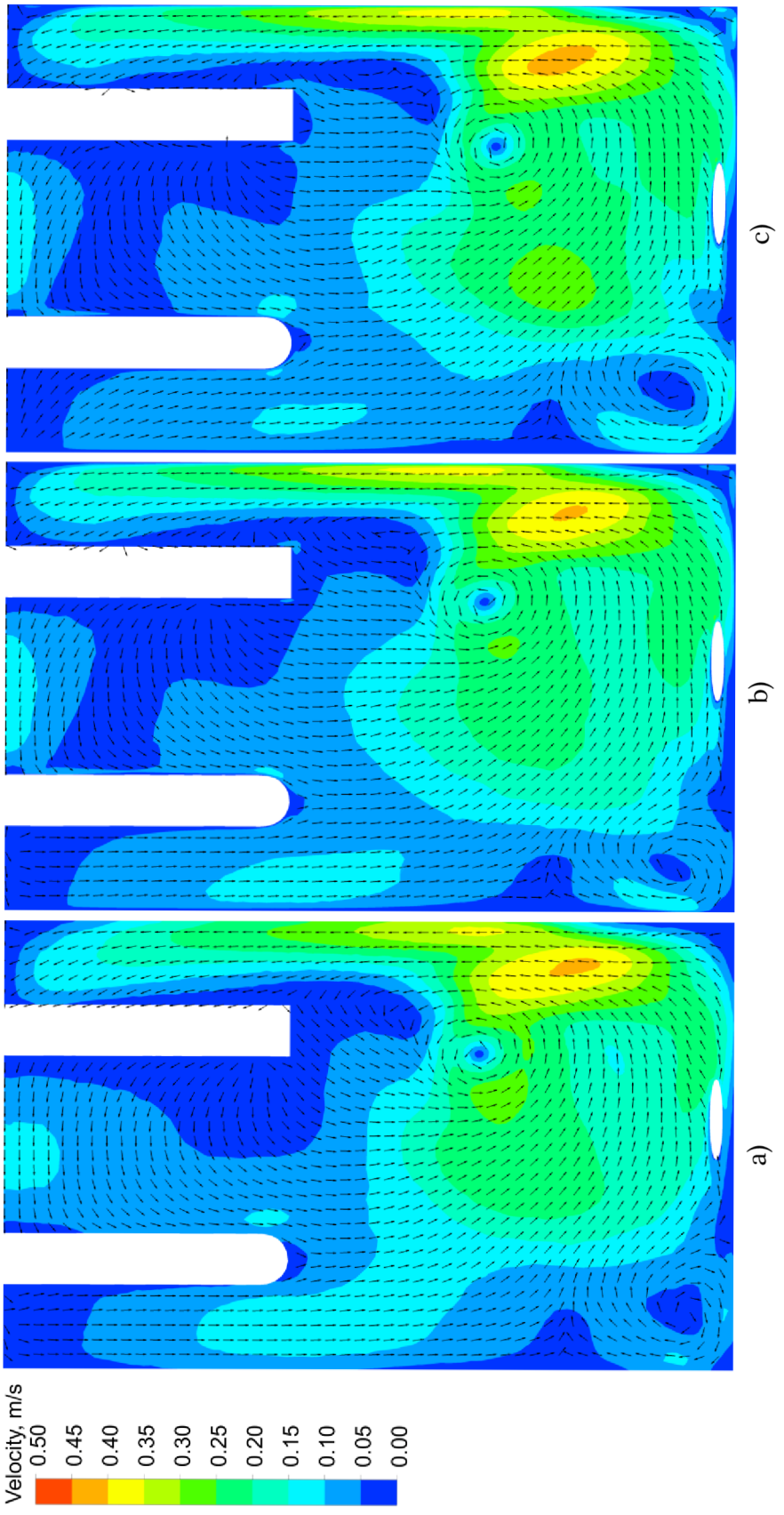

Figure 4.17 Velocity contours from CFD with no aeration at 480 rpm
a) coarse mesh, b) medium mesh, c) fine mesh

Additionally, accuracy of the numerical model was evaluated by the comparison of perpendicular velocity components along axes centred to the main vortex induced by the rotating stir bar. The illustration of vortex axes is in Figure 4.18. Coordinates x_V and y_V mark the distance of the vortex centre from beginning of the coordinate system in x- and y-direction, respectively. Figure 4.19 and Figure 4.22 show mean x- and y-velocities on local vertical and horizontal axes for both rotational speeds and for four different data, i.e., data from the PIV experiment and CFD data using three different mesh resolutions.

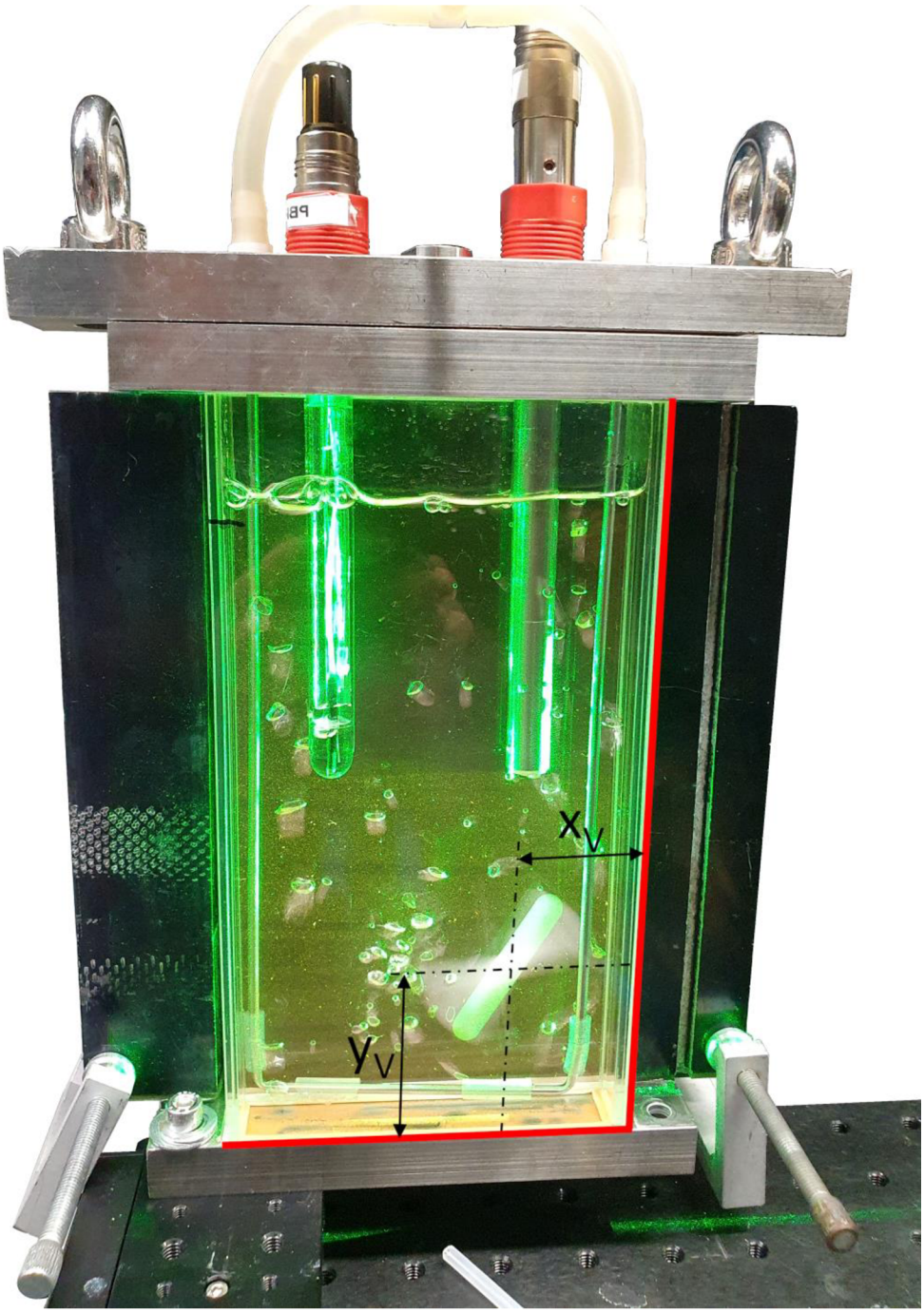

Figure 4.18 Vortex positon

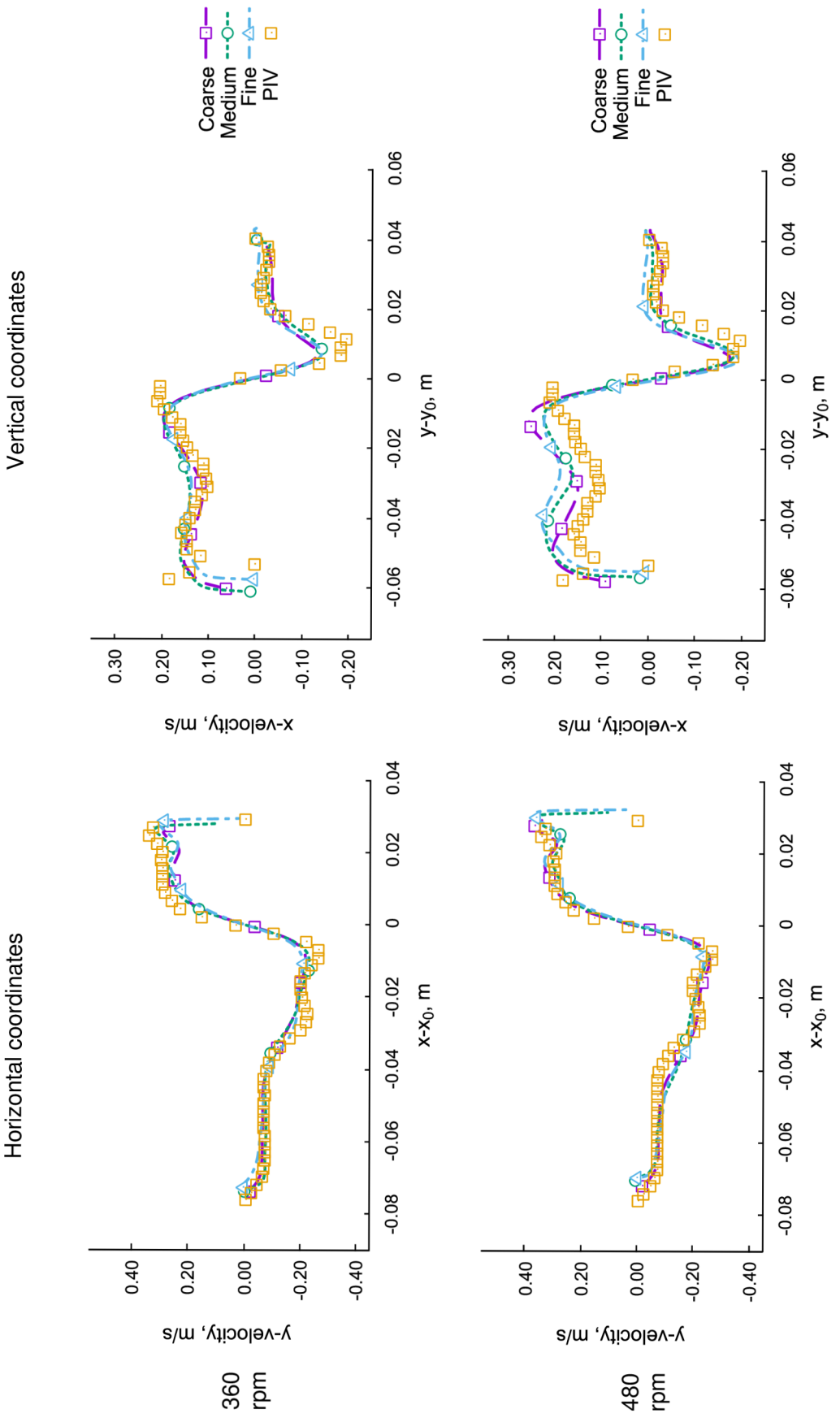

Figure 4.19 Horizontal and vertical velocity profiles in the main vortex with no aeration

Two-phase flow simulations with flow induced by stirrer and bubbles

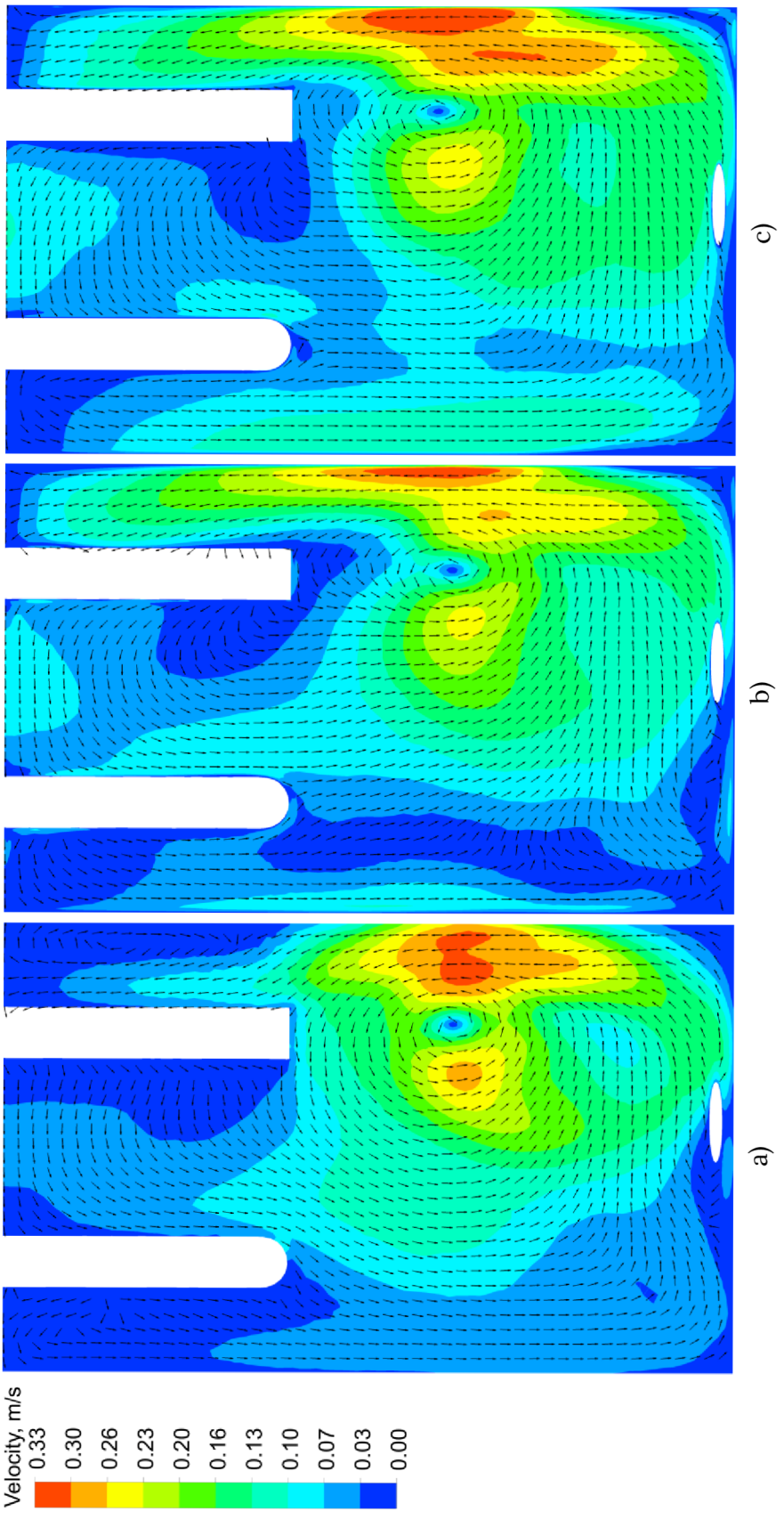

Figure 4.20 Velocity contour from CFD with 200 ml min^{-1} aeration rate at 360 rpm
a) coarse mesh, b) medium mesh, c) fine mesh

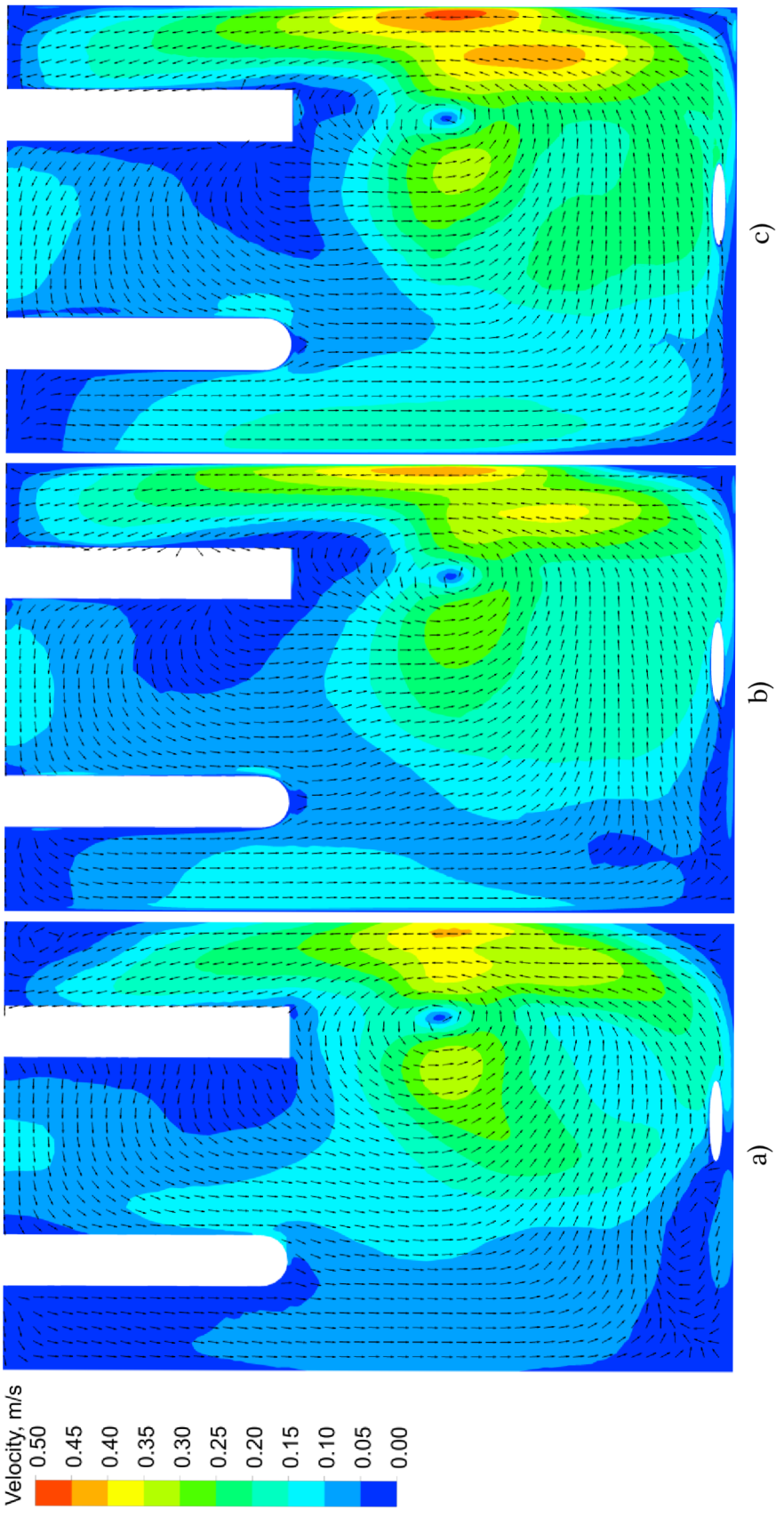

Figure 4.21 Velocity contour from CFD with 200 ml min^{-1} aeration rate at 480 rpm
a) coarse mesh, b) medium mesh, c) fine mesh

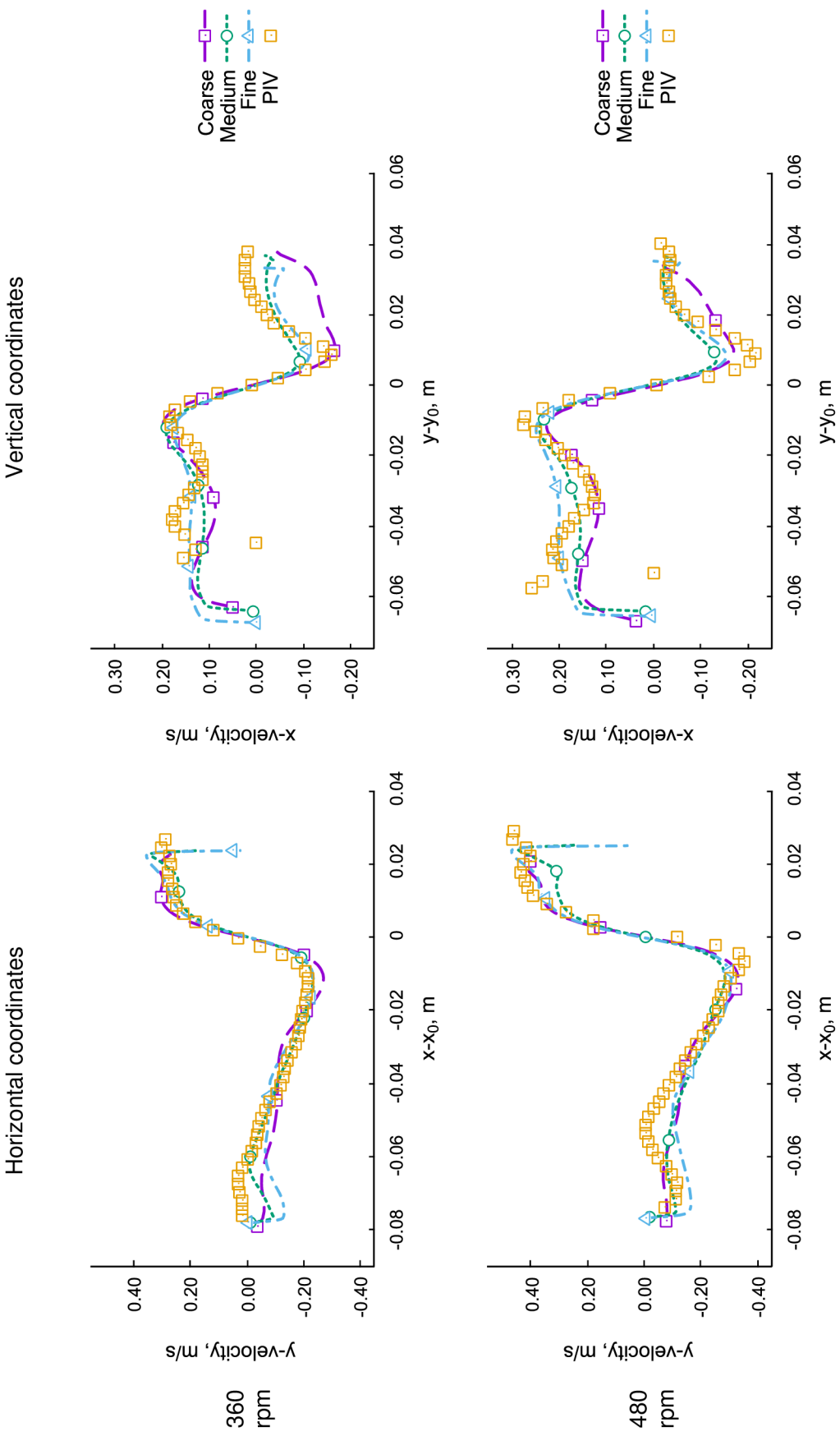

Figure 4.22 Horizontal and vertical velocity profiles in the main vortex with 200 ml/min aeration rate

Changes in the gas hold-up were observed under different operating conditions. Gas hold-up at the aeration flow rate of 200 ml min^{-1} for both agitation speeds and for the case without agitation is presented in Figure 4.23. Time-averaged volume fraction contour plot for both agitation speeds on the medium mesh is in Figure 4.24.

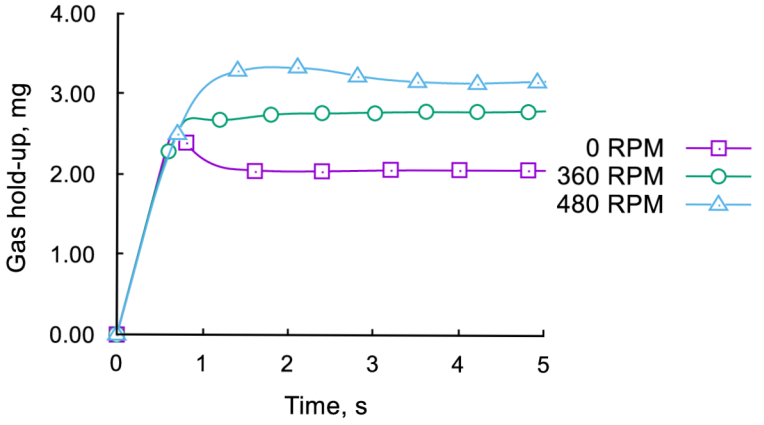

Figure 4.23 Gas hold-up from CFD using coarse mesh at different agitation speeds and with 200 ml min^{-1} aeration rate

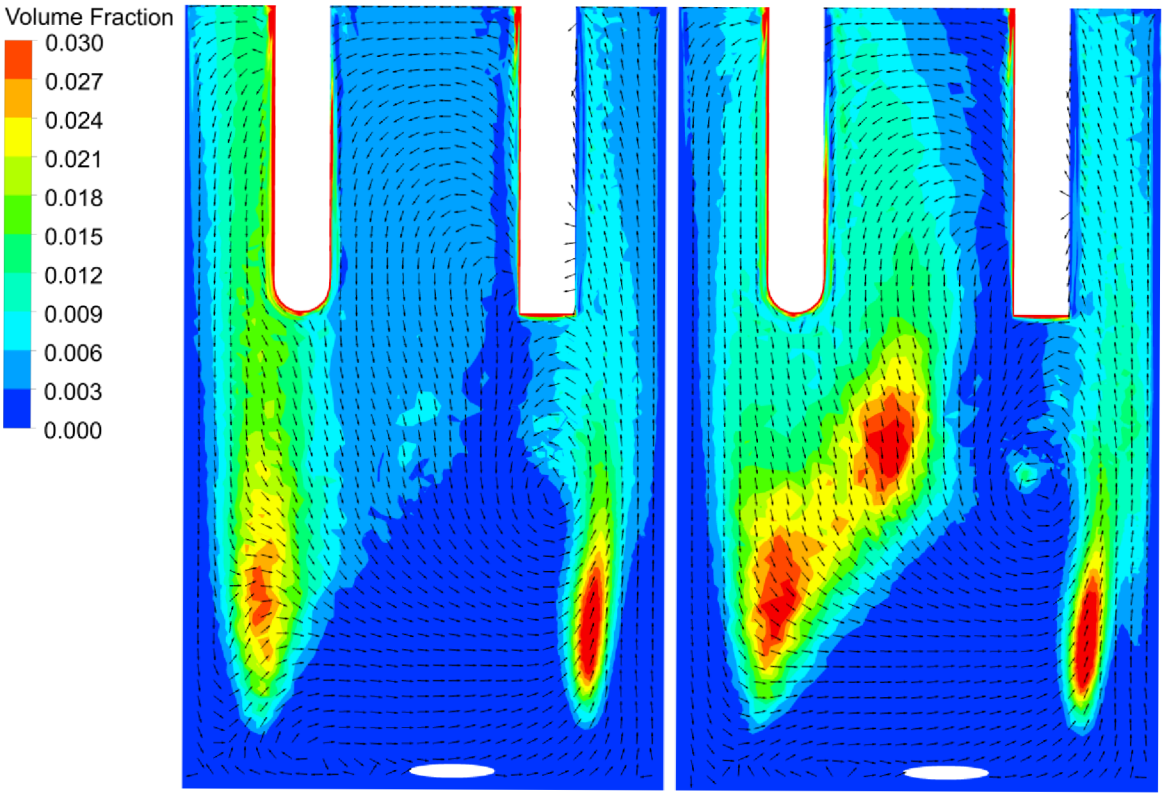

Figure 4.24 Volume fraction on medium mesh at 200 ml min^{-1}
left: 360 rpm, right: 480 rpm

4.3 Shear Stress Analysis

In the following text, shear stresses are presented under different agitation speeds, 360 rpm and 480 rpm, and with or without gas aeration. The CFD assessment in the photobioreactor was based on the time averaging of shear stresses on the medium mesh. Low shear values are desirable so that living microorganism are not harmed. Based on the Wang and Lan (2018), such critical threshold can be identified as 2 Pa for the studied species grown in PBRs. In the post-processing, shear stresses were categorised into 5 levels:

- Level 1: under 0.5 Pa
- Level 2: 0.5–1.0 Pa
- Level 3: 1.0–1.5 Pa
- Level 4: 1.5–2.0 Pa
- Level 5: above 2.0 Pa

Similarly to the preceding analyses, mean shear stresses were assessed on the cuvette's mid-plane and are plotted in Figure 4.25 and Figure 4.26. Proportionate coverage of the mid-plane area by shear stress levels is presented in a combined column graph in Figure 4.28. The effect of aeration on shear stresses is shown in Figure 4.29. In addition to that, wall shear stresses are also presented on walls of the inner equipment, see Figure 4.27. These figures depict wall shear stresses for the complete configuration, i.e., with agitation and aeration, as there was no major difference observed in cases without aeration. The highest wall shear stresses were found on the stir bar and were propagating to the region near-by.

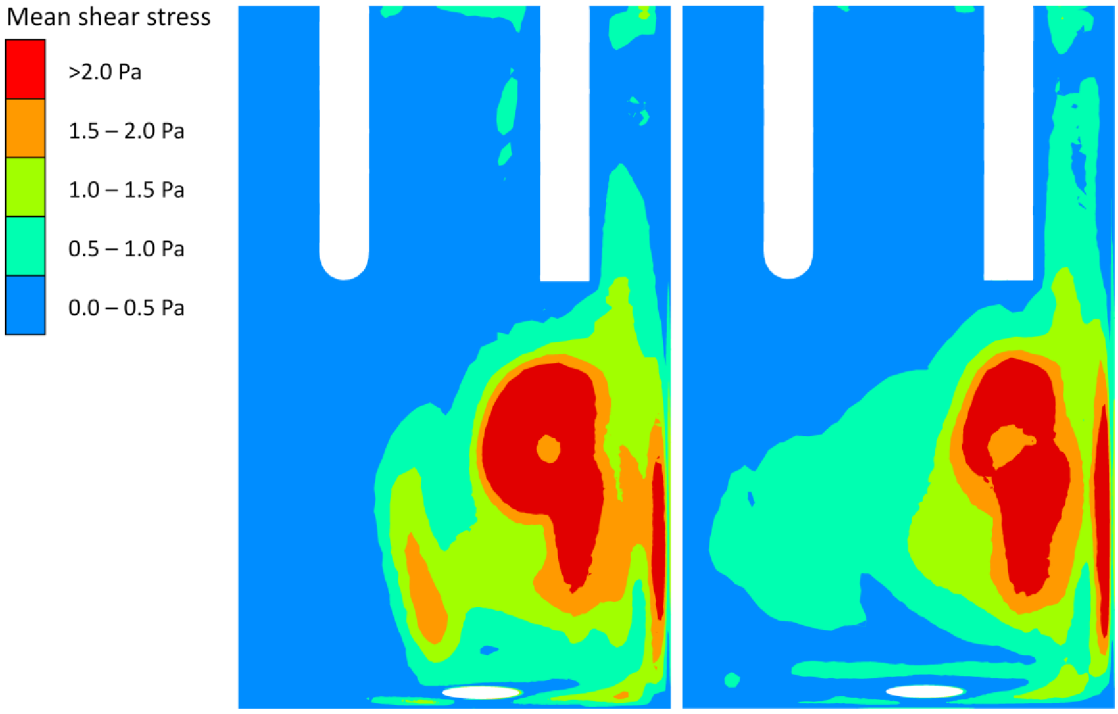

Figure 4.25 Mean shear stress at 360 rpm
left: 0 ml min^{-1}, right: 200 ml min^{-1}

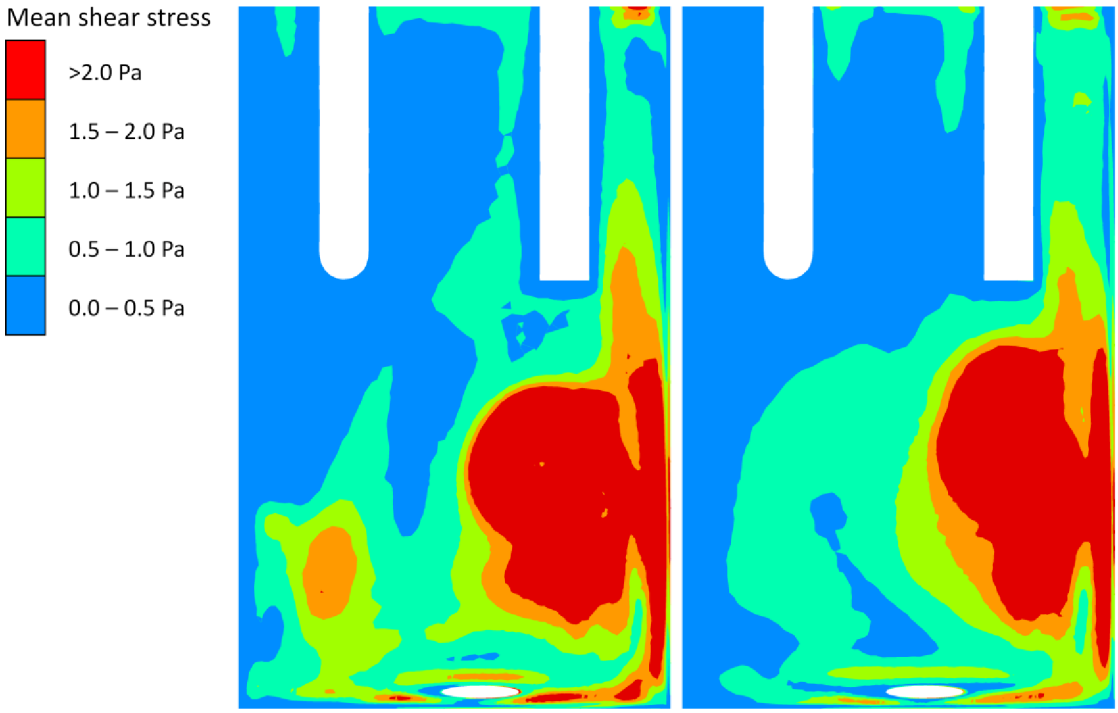

Figure 4.26 Mean shear stress at 480 rpm
left: 0 ml min^{-1}, right: 200 ml min^{-1}

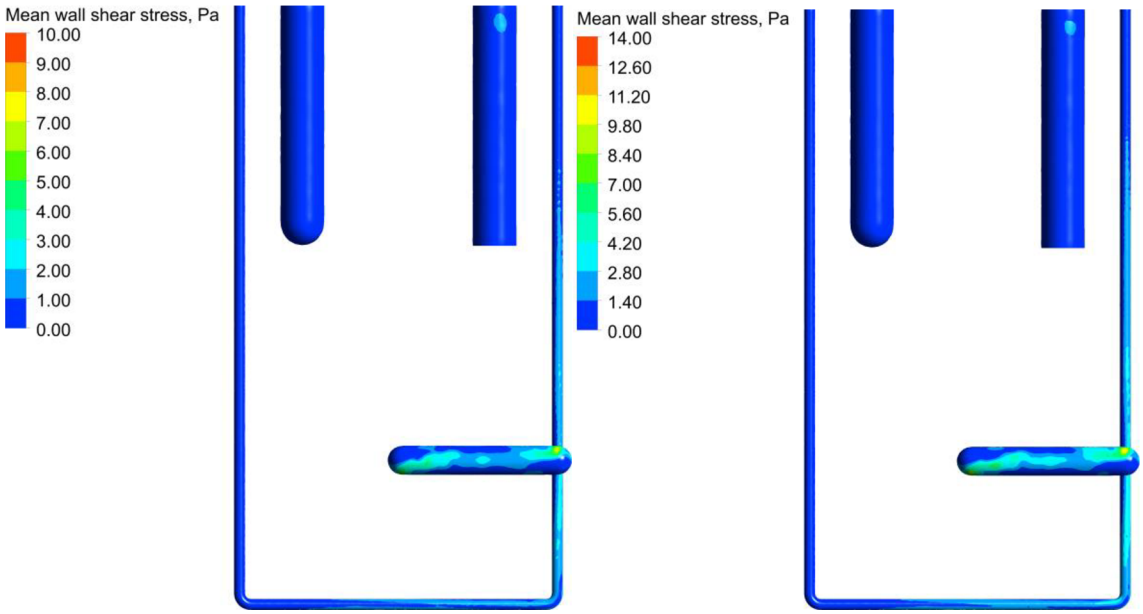

Figure 4.27 Mean wall shear stress at 200 ml min^{-1} aeration rate
left: 360 rpm, right: 480 rpm

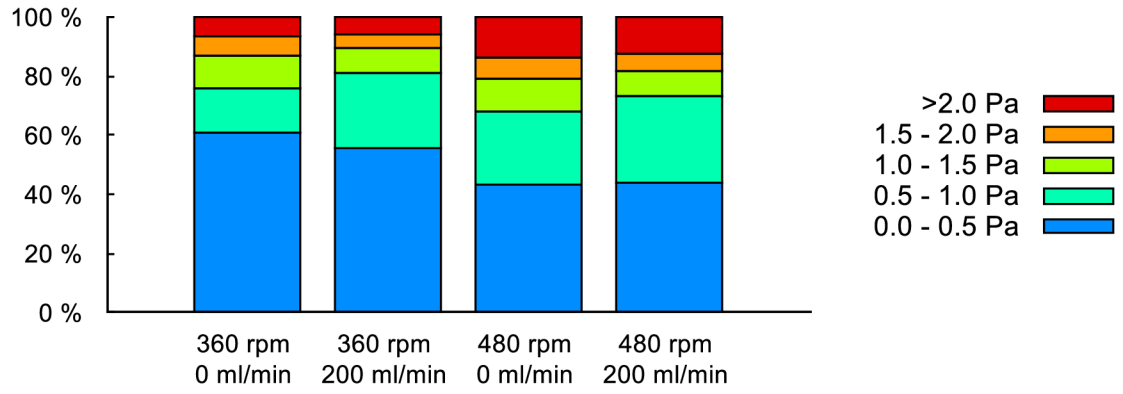

Figure 4.28 Relative coverage of shear stress levels

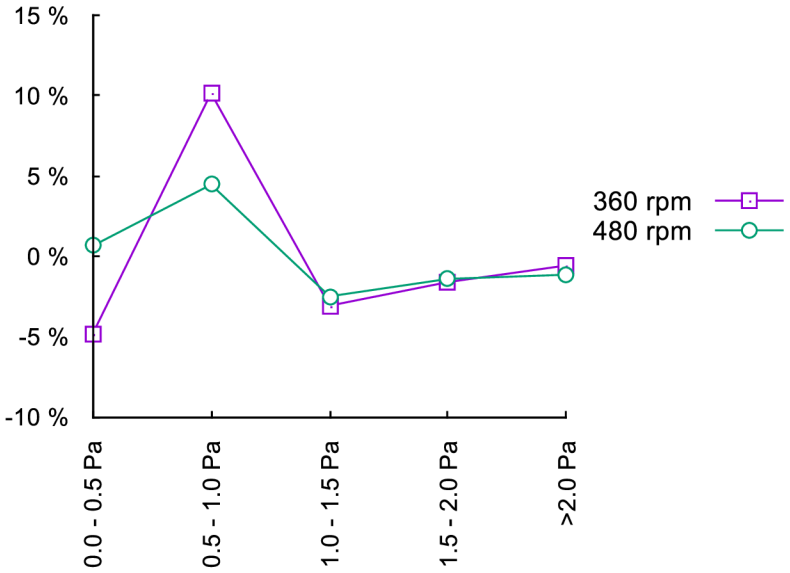

Figure 4.29 Difference in relative coverage of shear stress levels for selected agitation speeds when aeration is introduced

4.4 Hydrodynamic Model Summary

The hydrodynamic model of a stirred flat-panel photobioreactor was numerically analysed by 3D CFD simulations and compared with experimental measurements. The experimental results were obtained with the PIV method that was found suitable for the application. However, there was one limitation resulting from the cuvette's construction, i.e., the presence of both probes that did not allow to fully cover the inner domain with the laser plane, see Figure 4.5 for a detail. As a result, a small portion of the domain between the two probes rendered invalid data. Nevertheless, this invalid region was not crucial to measurements and subsequent assessment.

The assessment of the model was done with means of velocity contours and vector fields from time-averaged values on the cuvette's mid-plane, and velocity profiles in a local coordinate system placed in the main vortex. Furthermore, numerical model was built with three computational grids different in the refinement level. The comparison in previous figures and plots shows that even a coarse mesh was able to predict the most distinguished variations of the velocity field, e.g. the prediction of the position of local extrema. However, prediction of smaller, secondary, vortices was in some cases underestimated. In contrast, to that, the CFD data in Figure 4.19 and Figure 4.22 show that finer meshes tend to improve towards the PIV data. Nevertheless, going from medium to fine mesh was not found to justify the increased computational time. Hence, the medium mesh would be the choice for any subsequent work.

The increased agitation speeds yielded higher slip velocities between phases. Presented CFD simulations of the two-phase flows yielded slip velocities of 0.22 m s^{-1}, 0.23 m s^{-1}, and 0.24 m s^{-1} for the aerated operating regime without aeration, the aerated operating regime at 360 rpm, and the aerated operating regime at 480 rpm, respectively. Consequently, this yielded different Eötvös and Reynolds numbers and, therefore, there was the transition from the wobbling-ellipsoid to spherical bubble shape in the Grace diagram in Figure 2.1. This effect is also captured in Figure 3.5b and c.

Local velocity profiles in Figure 4.19 and Figure 4.22 show that the main vortex tends to travel horizontally with increased rotational speeds of the stirrer. The horizontal distance of the vortex from the bottom of the cuvette increases by about 9 mm.

In addition to velocity field, the gas hold-up in the aerated operating regimes was monitored, as well. The total air mass in the cuvette reached a pseudo-steady state in 2 – 4 s, depending on the rotational speed of the stirrer, see Figure 4.23. It was found that the gas hold-up increases with the rotational speed. This was also observed in experiments with the high-speed camera, as shown in Figure 3.5. It can be assumed that under no agitation, the bubble size was the largest and the buoyancy force was the most dominant force acting upon bubbles. When agitation was introduced, however, bubbles were broken into smaller bubbles and the buoyancy force got smaller. In addition to that, bubbles might get trapped in the swirling patterns caused by the rotating stir bar and, therefore, their residence time was longer.

For the case with the aeration only, the images from the high-speed camera were also used for an image analysis to estimate the mean bubble rising velocity. The velocity was found to be 0.22 m s^{-1}. A volume-averaged velocity of the air phase in CFD simulations was 0.21 m s^{-1} while induced water velocity reached up to 0.15 m s^{-1}, as show in Figure 4.6 and Figure 4.12, respectively.

The hydrodynamic model validation was followed-up with the shear stress analysis. Again, the assessment of shear stresses was based on their time averaging on the photobioreactor's mid-plane and on internal walls. Next, shear stresses were categorised into 5 levels with 0.5 Pa step and reaching the maximum threshold of 2 Pa. The threshold

was selected as a reference value based on the work of Wang and Lan (2018). However, the threshold can vary between microalgae species.

In case of the 360 rpm agitation speed, the shear stresses up to 1 Pa, i.e. Level 1 and Level 2, gave the greatest coverage, approx. 80 %, while the shear stresses from Level 3 and above were present only in the stir bar region occupying approx. 20 % of the mid-plane area. This 80/20 distribution was found regardless of the aeration. However, the introduction of the aeration added 10 % of Level 2 shear stresses at the expense of the Level 1. So, there was no effect of aeration on higher levels of shear stress observed. There was less than 2 % difference in shear stresses, see Figure 4.29.

Similarly in cases with the 480 rpm agitation speed, the Level 1 and Level 2 shear stresses occupied the largest area of the mid-plane, ca. 70 %, while the highest shear stress levels (above the critical shear stress) covered more than 10 % of the area and spread further from the stirrer. Moreover, the secondary vortex formed in the lower left corner gained on the intensity and created another high-risk area for the culture. The presence of the gas flow had very little effect on shear stresses in this case, see Figure 4.29. Therefore, with this agitation speed, the main cause of high shear stresses was the stir bar and velocity gradients it produced. Figure 4.27 shows that the in-volume shear stresses were the highest around the stirrer as on the bar itself the wall shear stresses reached its maximum 13 Pa. However, the stirrer area was relatively small with respect to the overall reactor volume.

5 Mass Transfer Model

Numerical simulations of the mass transfer model presented in this chapter were applied to both types of photobioreactor discussed in this thesis. At first, spatial and temporal scales of the mass transfer phenomenon were analysed on the tubular reactor. Then, the findings were applied to the flat-panel reactor. Objective in development of the mass transfer model was to predict the mass transfer coefficient k_L, and to validate the numerical results with the experimental data.

5.1 Preliminary Simulations

All preliminary mass-transfer simulations were performed on the tubular photobioreactor presented in the Chapter 3.2 and were published in greater detail in Rebej et al. (2022a) and Rebej et al. (2022b).

The 3D CAD geometry and the computational mesh of the tubular reactor were made in the ANSYS SpaceClaim. However, to simplify the numerical model, only one tube was modelled. Similarly to the flat-panel photobioreactor, the computational geometry was divided into two cell zones, the inlet zone and the domain zone. This simplification was based on the fact that the uniform bubbly flow had developed shortly after the air injection, see details in Figure 3.7. The modification then allowed to neglect the geometry of the perforated inlet membrane and to model the inlet boundary condition as a mass source term. The domain cell zone filled the rest of the plain inner volume of a tube.

The numerical model was based on the Eulerian-Eulerian multiphase framework in the ANSYS Fluent 2021 R2. The framework used two phases, the primary phase with liquid water and liquid CO_2, and the secondary phase with the aeration gas. However, to further simplify the numerical model, the modelled composition of the aeration gas neglected the three least frequent components. Individual mass diffusion coefficients are listed in Table 5.1. Respective material properties were taken from the material library in the ANSYS Fluent. The gaseous phase was based on the incompressible ideal gas, whereas the density method for the primary phase was based on the volume mixing law.

The interphase equilibrium model for the interphase species mass transfer employed the Henry's law formulation and the molar concentration was 3,030,300 Pa m^3 $kmol^{-1}$ (Sander, 2015). Next, the Penetration model in Eq. (6) (Higbie, 1935) was used to determine the mass transfer coefficient.

Table 5.1 Diffusion coefficients

Species pair	Diffusion coefficient, $cm^2 s^{-1}$
CO_2 – O_2 (g)	0.156
CO_2 – N_2 (g)	0.165
N_2 – O_2 (g)	0.220
H_2O – CO_2 (l)	1.92e-5

In case of the tubular photobioreactor, the penetration model yielded the mass transfer coefficient of 8.5·10-5 m s^{-1} while the bubble rising velocity in water for bubbles 4.5 mm large in diameter was around 0.35 m s^{-1}. The reactor gave good results in reaching the homogeneity of the mixture, as well, see Figure 5.1. As a result, the hydrodynamic phenomenon was considered to define the spatial discretization of the numerical model. Nevertheless, the mass transfer phenomenon defined the time scale, see Figure 5.2 where it took 15 minutes to reach saturated state.

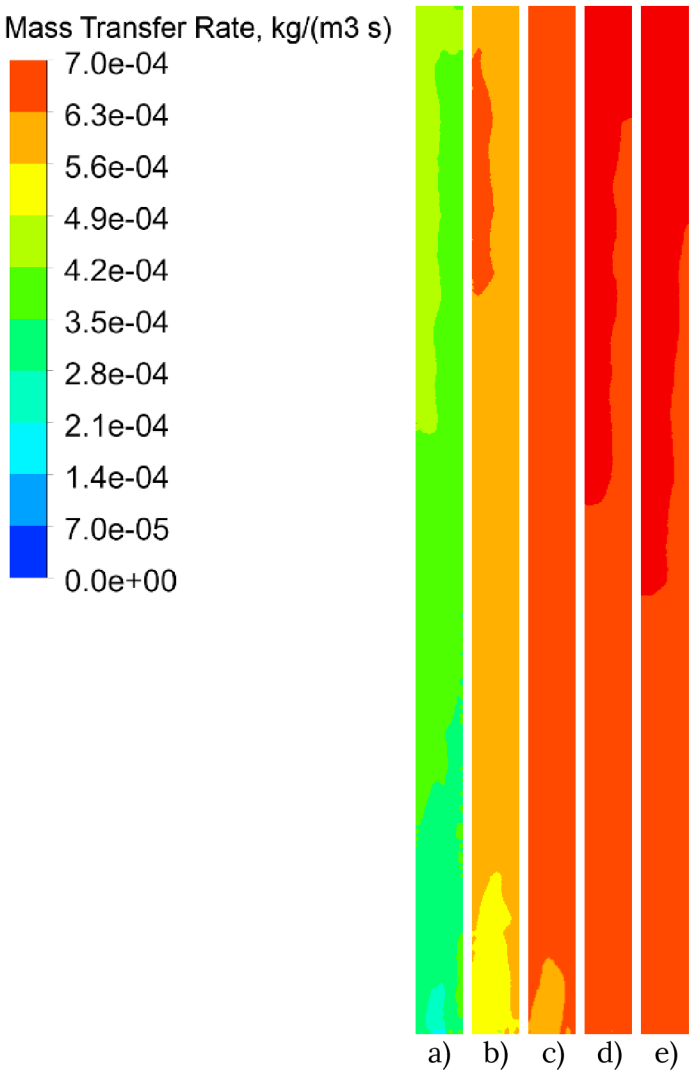

Figure 5.1 Mass transfer rate at different time steps,
a) 3 min, b) 6 min, c) 9 min, d) 12 min, e) 15 min.

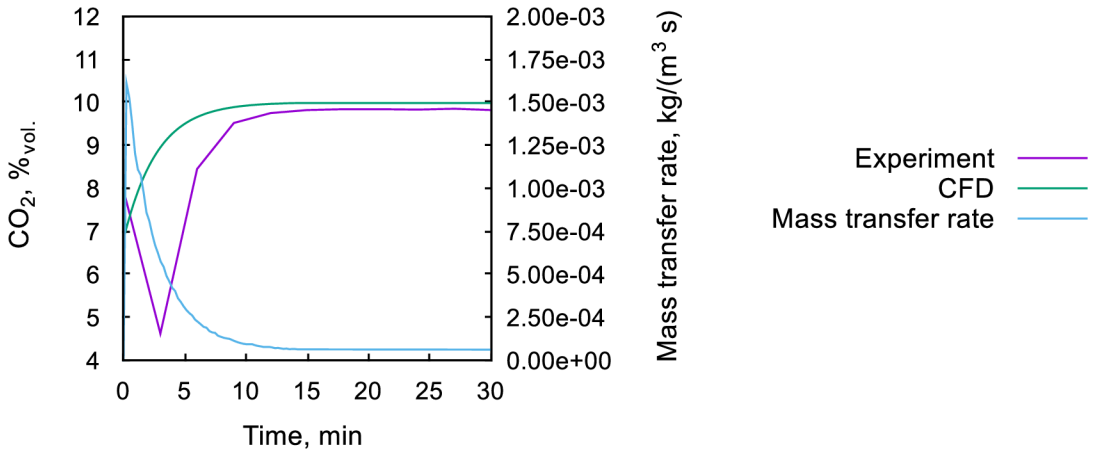

Figure 5.2 Volume fraction of CO_2 and mass transfer rate in the vertical bubble-column photobioreactor

5.2 Numerical Simulations

The application of the mass transfer model on the previously validated hydrodynamic model was another step in the development of the comprehensive model of the photobioreactor. Following chapter presents its setup and results.

5.2.1 Numerical Model Setup

The mass transfer model applied to the flat-panel photobioreactor followed the work that had already been presented, i.e., it used the medium mesh of the flat-panel photobioreactor and extended its validated hydrodynamic model. It was also based on the preliminary work on the mass transfer model in the ANSYS Fluent using the vertical bubble-column photobioreactor. The flat-panel reactor was aerated with the aeration gas flow rate of 200 ml min^{-1} and the aeration gas was air enriched with 3 % of CO_2. Experiments were performed with the 360 rpm agitation speed.

The interphase species mass transfer employed the Henry's law formulation. However, in contrast to the fluid flow induced by bubbles in case of the bubble-column photobioreactor, forced agitation in the flat-panel photobioreactor yields flow with a turbulent region that may be suitable for the Eddy cell model. Therefore, in addition to the Penetration model, the Eddy cell model was implemented into the ANSYS Fluent with the user-defined function (UDF), as well. The difference between models is in the definition of the contact time where the Eddy cell model estimates the contact time at the gas-liquid interface with the turbulent dissipation rate rather than with the slip velocity. Model constants F and K were obtained by fitting simulation predictions for the Penetration model and the Eddy cell model to the experimental data.

Next, in terms of discretization schemes and operating conditions, this setup copied the setup presented in the hydrodynamic model. Similarly, convergence was reached when

residuals were below 10^{-3} levels. In addition to that, the approach presented in Ndiaye et al. (2018) was followed so that once the momentum, turbulence, and volume fraction equations were converged and stabilized, their calculation was disabled and the mass transfer was calculated on the frozen hydrodynamic field only. This approach allowed to get the benefit of a larger time step size and to proceed through the required time interval faster. The time step size of 1 s yielded the CFL of approx. 0.45 for the expected volume-averaged k_L of $0.4 \cdot 10^{-3}$ m s^{-1}.

5.2.2 Results

This chapter presents the results of the mass transfer. Laboratory data were provided by a project partner in the form of pH in time. The correlation with the dissolved CO_2 was found with the Eq. (9) (Cupp et al., 2017). Measured pH values and corresponding saturation of CO_2 in the liquid are presented in Figure 5.3.

$$C_{CO_2} = 10^8 \cdot e^{-2.212 \cdot pH} \tag{9}$$

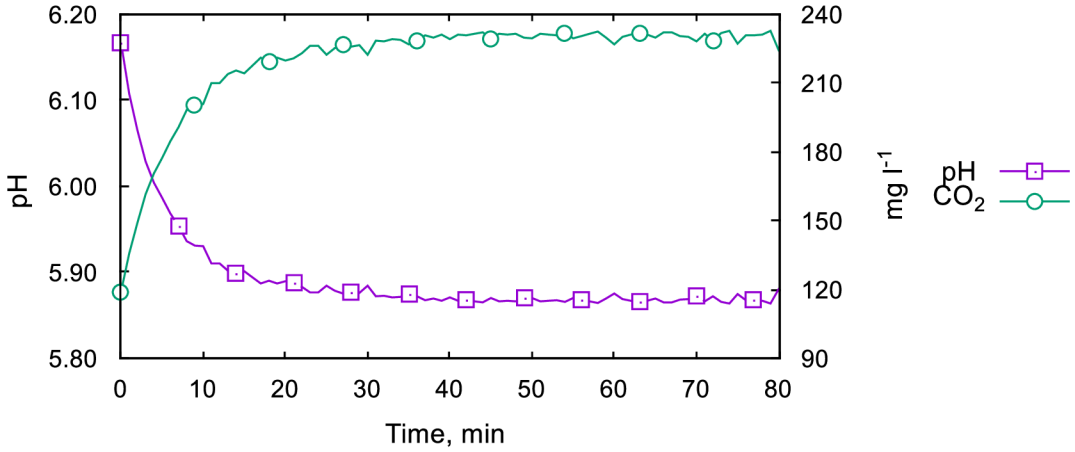

Figure 5.3 Laboratory data

In Figure 5.4, the concentration of CO_2 was monitored for both mass transfer coefficient models. In addition to that, the figure also shows the concentration of CO_2 found in the experiments. The CO_2 saturation concentration found in the experiment was approx. 235 mg l^{-1} and was predicted the most accurately by the Penetration model. The Eddy cell model overpredicted this value by more than 50 %. The maximum estimated values for the mass transfer coefficient were $0.58 \cdot 10^{-3}$ m s^{-1} and $2.2 \cdot 10^{-3}$ m s^{-1} for the Penetration model and the Eddy cell model, respectively. A detailed contour plots on the cuvette's mid-plane are in Figure 5.5 and Figure 5.6.

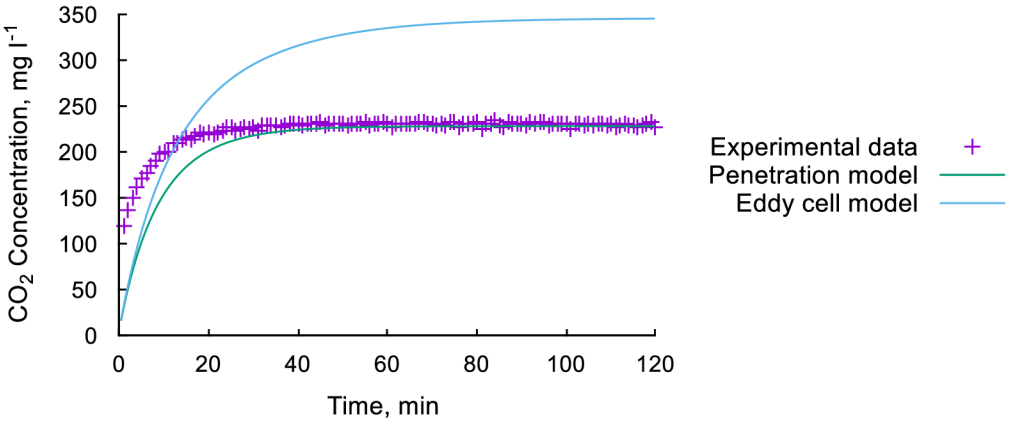

Figure 5.4 CO_2 concentration in the liqud phase

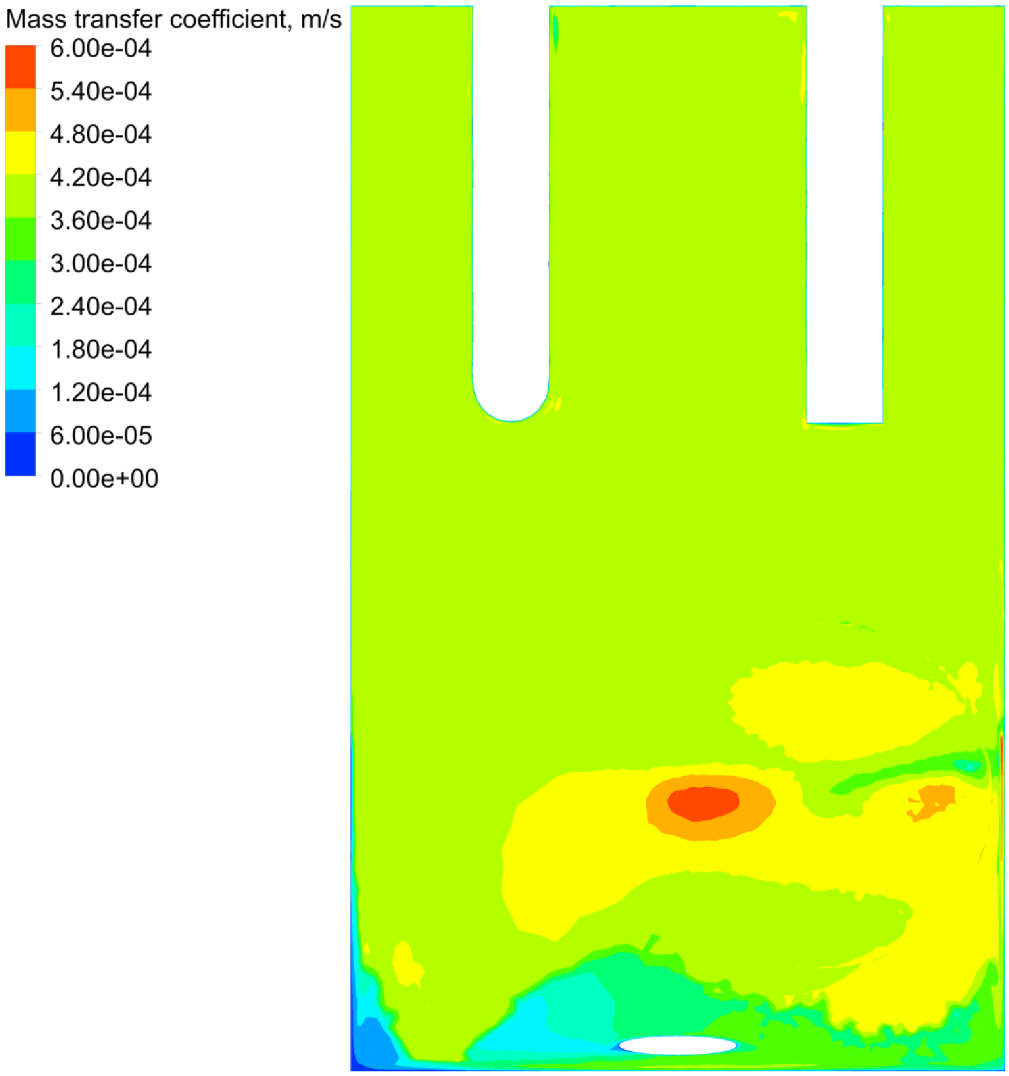

Figure 5.5 Mass transfer coefficient with the Penetration model.

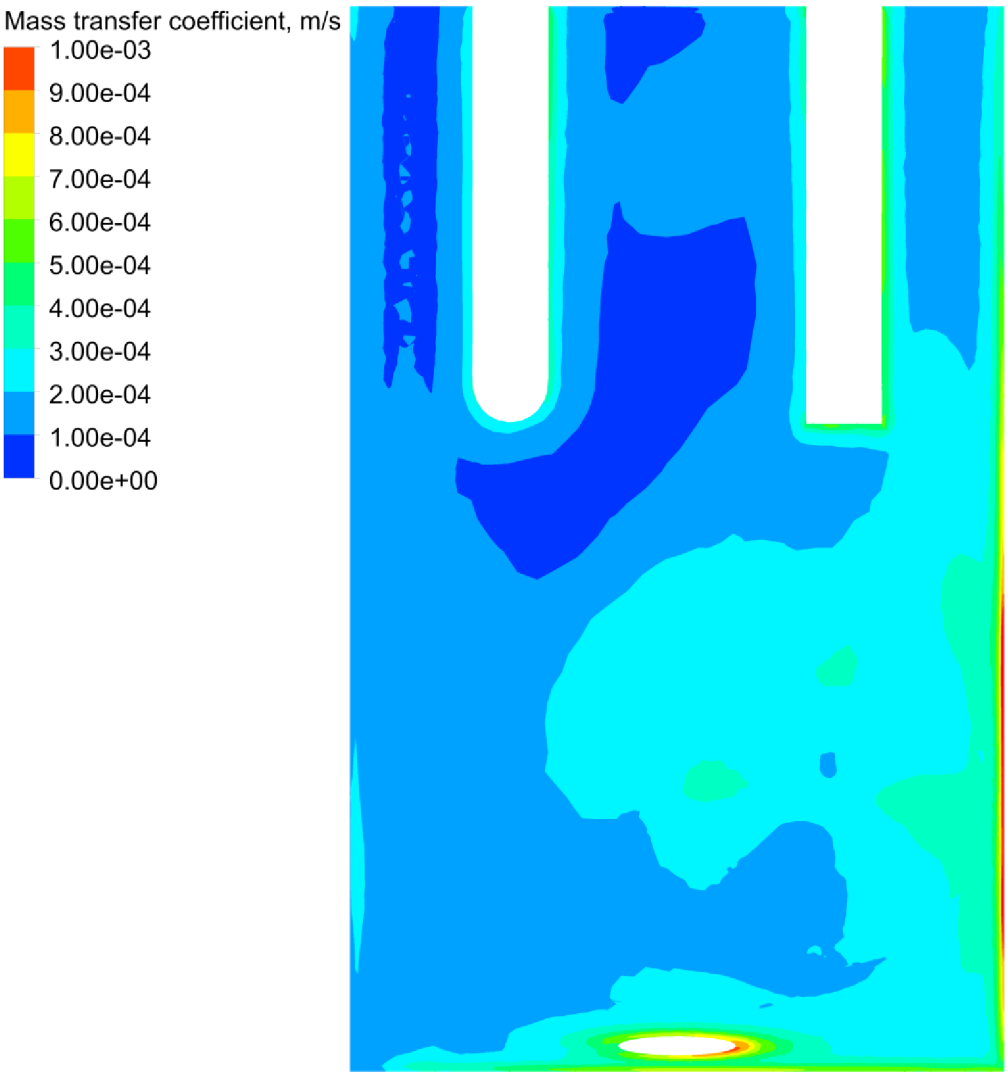

Figure 5.6 Mass transfer coefficient with the Eddy cell model.
The contour is limited to 0.001 m s^{-1}.

5.3 Mass Transfer Model Summary

This chapter presented numerical mass transfer simulations of two selected photobioreactors. At first, the vertical tubular photobioreactor from the laboratory at the Institute of Process Engineering was used to study the scales of the mass transfer phenomenon. Next, the previously validated hydrodynamic model of the flat-panel photobioreactor was extended with the mass transfer model. Both photobioreactors were simulated with the 3D CFD simulations in the Eulerian-Eulerian modelling framework. In addition to that, two mas transfer coefficient models were used.

Results from the numerical simulations were compared with the experimental data provided either by another research group at the institute in case of the tubular photobioreactor, or by the project partner in case of the flat-panel photobioreactor. The experimental data were also used to set-up and tweak the model and its constants.

Model constants F and K were specified with values $F = K = 1.0$. These values were selected based on the several mass transfer simulations using the specified model where simulations with different values of the respective model constant were performed. The Penetration model yielded the most accurate results for the $F = 1.0$. However, for a wide range of K values, the Eddy cell model yielded either unrealistic results or its convergence was negatively affected. Even though the model with value $K = 1.0$ still overpredicted the mass transfer coefficient, this value was selected as the final value since the simulation was numerically stable and the problem converged.

The Penetration model showed a good fit in the evolution of CO_2 concentration in the liquid phase of the flat-panel photobioreactor. The experimental data showed that the concentration in the cuvette reached its maximum value in approx. 40 minutes while the Penetration model predicted the saturation in approx. 60 minutes, see Figure 5.4. The difference could be due to the applied under-relaxation factors of 0.5 and 0.8 for the species in the liquid and the gaseous phase, respectively. The Eddy cell model, on the other hand, reaches its maximum of more than 320 mg l^{-1} in approx. 100 minutes.

In case of the Penetration model, the volume-averaged mass transfer coefficient was approx. $0.41 \cdot 10^{-3}$ m s^{-1} and, as shown in the Figure 5.5, the model shows uniform distribution of the mass transfer coefficient there. The maximum of $0.58 \cdot 10^{-3}$ m s^{-1} was in the region close to the stir bar where slip velocity was the largest. In contrast to that, the volume-averaged mass transfer coefficient in the Eddy cell model in Figure 5.6 was $0.14 \cdot 10^{-3}$ m s^{-1} with the maximum of $2.2 \cdot 10^{-3}$ m s^{-1} at the side wall close to the stir bar.

Since the Eddy cell model did not yield valid results and the Penetration model itself yielded satisfactory mass transfer predictions, no additional modification of any mass transfer coefficient model, e.g. the Adaptive model presented by Gao et al. (2015a), were not considered.

6 Comprehensive Model of a Photobioreactor

This chapter demonstrates the next stage in the development of the comprehensive photobioreactor model that involves implementation of the irradiance model. The objective was to test the model coupling and to possibly analyse the light intensity distribution within the aerated medium. The irradiance model presented in this chapter was based on the model presented in a greater detail in Juřena et al. (2020).

6.1 Numerical Model Setup

The hydrodynamics, mass transfer, and irradiance model combination were used in the stirred flat-panel photobioreactor in the ANSYS Fluent. The model consisted of two phases, the gaseous phase with the 3 % CO_2 aeration gas and the liquid phase with water and CO_2. There was no solid phase to model the microalgae.

The effect of microalgae on light attenuation was simplified and accounted by an increased absorption coefficient in water only. This coefficient was set to the value of 10 m^{-1} for the 635 nm wavelength. The absorption of light in the gas phase was neglected. However, the light scattering from bubbles was modelled with a UDF. Radiation energy transfer was modelled using the Non-Grey Discrete Ordinates radiation model. The model solves the radiative transfer equation for a finite number of discrete solid angles. The angular discretization of 4 × 4 was used in the model. Next, there were two wavelength bands defined, the monochromatic light emitted by diodes with 635 nm wavelength and the light with longer wave spectra. As the cuvette is equipped on its back wall with LEDs with the intensity of 200 mole m^{-2} s^{-1}, the light source in the model was set to the respective intensity of 36.7 W m^{-2}.

Transient numerical simulations were performed on the converged velocity field where only transport equations for mass transfer and irradiation were solved. This approach followed the previous work and again allowed to proceed through the required time span with the 1 s time step size, i.e. neglecting small and short velocity fluctuations.

6.2 Results

Numerical simulation with the multiphase hydrodynamic model, the mass transfer model, and the irradiance model were performed for the total flow time of 80 minutes. Figure 6.1 shows the cuvette's depth-wise irradiance with the 635 nm wavelength light. However, as there was no microalgae present, there were no changes observed in the irradiance levels at different CO_2 concentrations during the simulated time span. Therefore, the irradiance model should be also combined with the third phase, i.e., the microalgae.

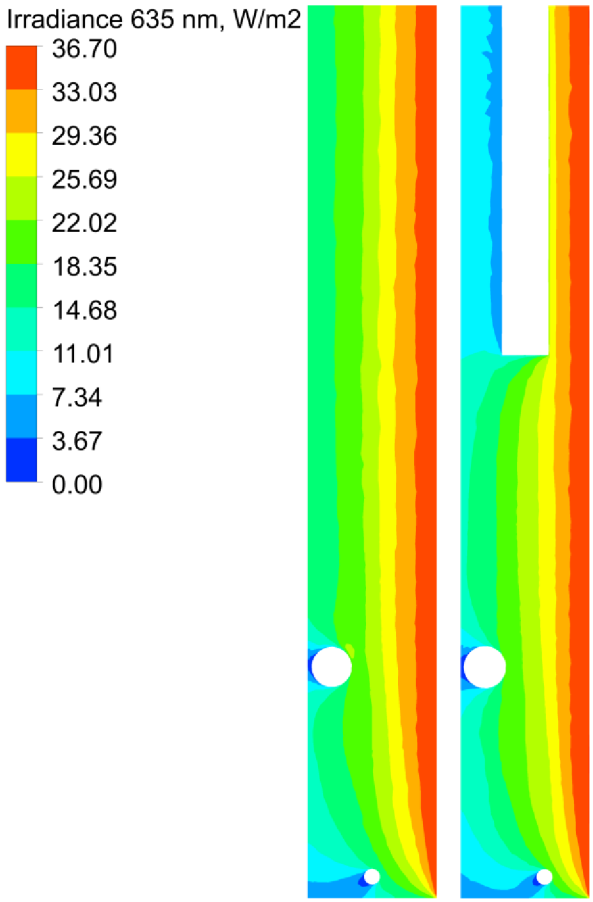

Figure 6.1 Irradiance contour plots with the 635 nm wavelength light at 80 min flow time.
Left: interrogation plane centred to the cuvette centre
Right: interrogation plane centred to the stirrer.

7 Summary

My doctoral dissertation thesis dealt with numerical simulations of photobioreactors. The first part of this thesis reviewed the research in numerical modelling of culturing systems. The review presented the most common CFD codes that were used in some recent publications. Essential numerical models for hydrodynamics, mass transfer, irradiation, and microalgae growth in photobioreactors were summarized there with an overview of the models used in these publications. It was found that authors were often divided in the necessity to include individual meso-scale models that describe the interaction of phases and that the numerical model verification is still crucial for the prospective scale-up applications. Moreover, it was found that there is still a need for a significant development and validation of such sub-models and coupling methods.

The second part of the thesis presented the laboratory photobioreactors used at the Institute of Process Engineering to develop the multiphase hydrodynamic model and the mass transfer model. There were two types of reactors, the flat-panel photobioreactor and the vertical column photobioreactor. The reactors were used for laboratory measurements of the fluid flow and CO_2 absorption, and their computer models were used for numerical simulations.

The Particle Image Velocimetry method was used to measure multiphase velocity fields induced by the stirrer and/or bubbles under different operating conditions in the flat-panel photobioreactor. Comparatively, the multiphase hydrodynamic model of the flat-panel photobioreactor under these operating conditions was developed in the ANSYS Fluent software. The model validation was based on the results of velocity profiles in monitored points, velocity profiles along axes centred to the vortex induced by the rotating stir bar, and velocity contour plots. In addition to that, numerical analyses were carried out on three meshes different in the level of refinement so that the grid independence could be considered. The mesh with the medium level of refinement was considered optimal.

Next part of the thesis covered the species mass transfer model that extended the previously validated multiphase hydrodynamic model. There were two mass transfer coefficient models analysed on both types of photobioreactors discussed. The bubble-column type photobioreactor was used to study time and spatial scales of the problem. Next, the mass transfer model was tailored to the flat-panel photobioreactor type, mainly through its model constants. Its validation was then based on comparison of the absorbed

CO_2 in the liquid phase. Finally, the Penetration model-based mass transfer model would be the choice for any future mass transfer simulations.

At last, a brief demonstration of the irradiation model was given. The model was primarily used to test the coupling of individual numerical models in the ANSYS Fluent and to see the possible effect of absorbed CO_2 in the liquid phase on the light distribution. However, the model did not predict any significant changes in the light attenuation when the CO_2 got absorbed into the liquid phase. The presence of microalgae at concentration greater than 0.5 g l^{-1}, on the other hand, should have a stronger effect (Wheaton and Krishnamoorthy, 2012). At lover concentrations, only internal equipment had significant effect on the light attenuation.

In total, the photobioreactor model presented in this thesis followed the sequence in Figure 7.1. At first, the multiphase hydrodynamics model predicted the flow hydrodynamics for both phases, i.e., positional ($\vec{X}_{(l)}$ and $\vec{X}_{(g)}$) and velocity vectors ($\vec{U}_{(l)}$ and $\vec{U}_{(g)}$), specific interfacial area (a), and volume fractions (α). Second, the mass transfer model simulated the species transport and mass transfer between gas and liquid species. This yielded the mass transfer coefficient (k_L) and concentrations of individual species in both phases (c_L^i and c_G^i). Additionally, the irradiation model should simulate the light distribution, i.e., the intensity (I) and scattering (β) with the respect of the CO_2 concentration in the liquid phase.

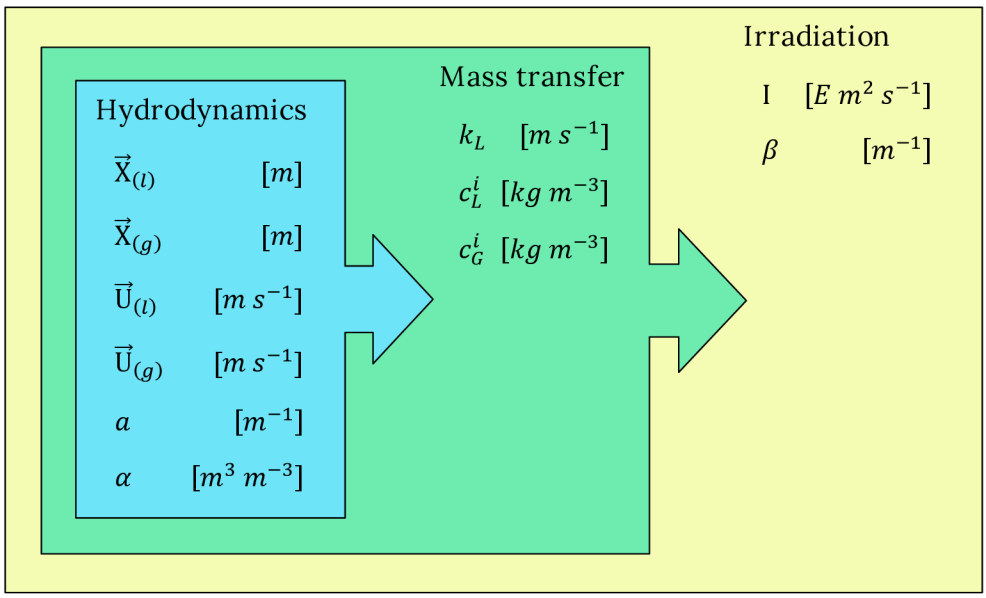

Figure 7.1 Photobioreactor model sequence

7.1 Future Work

The work in this thesis was to develop and validate computational models with an interplay between fluid hydrodynamics and species mass transfer. In addition to that, coupling with radiation transport was demonstrated, as well. Future work should, therefore, include an algae growth model that would predict biomass growth rates needed to determine the performance and scalability of a photobioreactor. Specifically, following work could be done with the current photobioreactor model:

- Analyse shear stresses at different agitation speeds, gas aeration rates, and stirrer sizes
- Extend the gas phase of the multiphase hydrodynamic model with the population balance equation to account for different bubble sizes
- Extend the multiphase hydrodynamic model with the solid phase to account for the microalgae
- Extend the mass transfer model to transfer of other species, e.g. O_2
- Validate the irradiation model with the laboratory experiments
- Link the multiphase hydrodynamic model and the species mass transfer model with the biomass growth model

Bibliography

ABiRe (2022). *Photos*. Available at: https://www.abire.org/publications/photos [Accessed May 13, 2022].

Acién Fernández, F. G., Fernández Sevilla, J. M., and Molina Grima, E. (2013). Photobioreactors for the production of microalgae. *Rev. Environ. Sci. Biotechnol.* 12, 131–151. doi: 10.1007/s11157-012-9307-6.

Ali, H., Solsvik, J., Wagner, J. L., Zhang, D., Hellgardt, K., and Park, C. W. (2019). CFD and kinetic-based modeling to optimize the sparger design of a large-scale photobioreactor for scaling up of biofuel production. *Biotechnol. Bioeng.* 116, 2200–2211. doi: https://doi.org/10.1002/bit.27010.

Almani, S., Blel, W., Gadoin, E., and Gentric, C. (2021). Investigation of single bubbles rising in Newtonian and non-Newtonian fluids inside a thin-gap bubble column intended for microalgae cultivation. *Chem. Eng. Res. Des.* 167, 218–230. doi: 10.1016/j.cherd.2021.01.010.

Amini, H., Wang, L., Hashemisohi, A., Shahbazi, A., Bikdash, M., Kc, D., et al. (2018). An integrated growth kinetics and computational fluid dynamics model for the analysis of algal productivity in open raceway ponds. *Comput. Electron. Agric.* 145, 363–372. doi: 10.1016/j.compag.2018.01.010.

ANSYS Inc. (2020a). ANSYS Fluent Theory Guide, Release 2020 R2.

ANSYS Inc. (2020b). ANSYS Fluent User's Guide, Release 2020 R2.

Bernardi, A., Perin, G., Sforza, E., Galvanin, F., Morosinotto, T., and Bezzo, F. (2014). An Identifiable State Model To Describe Light Intensity Influence on Microalgae Growth. *Ind. Eng. Chem. Res.* 53, 6738–6749. doi: 10.1021/ie500523z.

Bitog, J. P., Lee, I.-B., Lee, C.-G., Kim, K.-S., Hwang, H.-S., Hong, S.-W., et al. (2011). Application of computational fluid dynamics for modeling and designing photobioreactors for microalgae production: A review. *Comput. Electron. Agric.* 76, 131–147. doi: 10.1016/j.compag.2011.01.015.

Bitog, J. P. P., Lee, I.-B., Oh, H.-M., Hong, S.-W., Seo, I.-H., and Kwon, K.-S. (2014). Optimised hydrodynamic parameters for the design of photobioreactors using computational fluid dynamics and experimental validation. *Biosyst. Eng.* 122, 42–61. doi: 10.1016/j.biosystemseng.2014.03.006.

Buffo, A., and Marchisio, D. L. (2014). Modeling and simulation of turbulent polydisperse gas-liquid systems via the generalized population balance equation. *Rev. Chem. Eng.* 30, 73–126. doi: 10.1515/revce-2013-0015.

Cappello, V., Plais, C., Vial, C., and Augier, F. (2021). Scale-up of aerated bioreactors: CFD validation and application to the enzyme production by Trichoderma reesei. *Chem. Eng. Sci.* 229, 116033. doi: 10.1016/j.ces.2020.116033.

Chen, Z., Jiang, Z., Zhang, X., and Zhang, J. (2016). Numerical and experimental study on the CO2 gas–liquid mass transfer in flat-plate airlift photobioreactor with different baffles. *Biochem. Eng. J.* 106, 129–138. doi: 10.1016/j.bej.2015.11.011.

Chisti, M. Y. (1989). *Airlift Bioreactors*. London: Elsevier Applied Science.

Courant, R., Friedrichs, K., and Lewy, H. (1928). Über die partiellen Differenzengleichungen der mathematischen Physik. *Math. Ann.* 100, 32–74. doi: 10.1007/BF01448839.

Cupp, A., Tix, J., Smerud, J., Erickson, R., Fredricks, K., Amberg, J., et al. (2017). Using dissolved carbon dioxide to alter the behavior of invasive round goby. *Manag. Biol. Invasions* 8, 567–574. doi: 10.3391/mbi.2017.8.4.12.

Darpito, C., Shin, W.-S., Jeon, S., Lee, H., Nam, K., Kwon, J.-H., et al. (2015). Cultivation of Chlorella protothecoides in anaerobically treated brewery wastewater for cost-effective biodiesel production. *Bioprocess Biosyst. Eng.* 38, 523–530. doi: 10.1007/s00449-014-1292-4.

Dijkhuizen, W., van Sint Annaland, M., and Kuipers, J. A. M. (2010). Numerical and experimental investigation of the lift force on single bubbles. *Chem. Eng. Sci.* 65, 1274–1287. doi: 10.1016/j.ces.2009.09.084.

Eilers, P. H. C., and Peeters, J. C. H. (1993). Dynamic behaviour of a model for photosynthesis and photoinhibition. *Ecol. Model.* 69, 113–133. doi: 10.1016/0304-3800(93)90052-T.

Farhadian, N., Behin, J., and Parvareh, A. (2018). Residence time distribution in an internal loop airlift reactor: CFD simulation versus digital image processing measurement. *Comput. Fluids* 167, 221–228. doi: 10.1016/j.compfluid.2018.02.030.

Gao, X. (2016). Advanced CFD model of multiphase photobioreactors for microalgal derived biomass production.

Gao, X., Kong, B., Ramezani, M., Olsen, M. G., and Vigil, R. D. (2015a). An adaptive model for gas-liquid mass transfer in a Taylor vortex reactor. *Int. J. Heat Mass Transf.* 91, 433–445. doi: 10.1016/j.ijheatmasstransfer.2015.07.125.

Gao, X., Kong, B., and Vigil, R. D. (2015b). CFD investigation of bubble effects on Taylor–Couette flow patterns in the weakly turbulent vortex regime. *Chem. Eng. J.* 270, 508–518. doi: 10.1016/j.cej.2015.02.061.

Gao, X., Kong, B., and Vigil, R. D. (2018a). Multiphysics simulation of algal growth in an airlift photobioreactor: Effects of fluid mixing and shear stress. *Bioresour. Technol.* 251, 75–83. doi: 10.1016/j.biortech.2017.12.014.

Gao, X., Kong, B., and Vigil, R. D. (2018b). Simulation of algal photobioreactors: recent developments and challenges. *Biotechnol. Lett.* 40, 1311–1327. doi: 10.1007/s10529-018-2595-3.

Grace, J. R., Wairegi, T., and Nguyen, T. H. (1976). Shapes and velocities of single drops and bubbles moving freely through immiscible liquids. *Trans. Inst. Chem. Eng.*, 167–173.

Guler, B. A., Deniz, I., Demirel, Z., and Imamoglu, E. (2020). Evaluation of scale-up methodologies and computational fluid dynamics simulation for fucoxanthin production in airlift photobioareactor. *Asia-Pac. J. Chem. Eng.* 15, e2532. doi: 10.1002/apj.2532.

Han, S.-F., Jin, W., Tu, R., Abomohra, A. E.-F., and Wang, Z.-H. (2016). Optimization of aeration for biodiesel production by Scenedesmus obliquus grown in municipal wastewater. *Bioprocess Biosyst. Eng.* 39, 1073–1079. doi: 10.1007/s00449-016-1585-x.

He, L., Yang, W., Guan, C., Yan, H., and Fu, P. (2017). Microalgal cultivation and hydrodynamic characterization using a novel tubular photobioreactor with helical blade rotors. *Bioprocess Biosyst. Eng.* 40, 1743–1751. doi: http://dx.doi.org/10.1007/s00449-017-1829-4.

Heo, S.-W., Ryu, B.-G., Nam, K., Kim, W., and Yang, J.-W. (2015). Simultaneous treatment of food-waste recycling wastewater and cultivation of Tetraselmis suecica for biodiesel production. *Bioprocess Biosyst. Eng.* 38, 1393–1398. doi: 10.1007/s00449-015-1380-0.

Higbie, R. (1935). The rate of absorption of a pure gas into still liquid during short periods of exposure. *Trans. Am. Inst. Chem. Eng.* 31, 365–377.

Huang, J., Kang, S., Wan, M., Li, Y., Qu, X., Feng, F., et al. (2015a). Numerical and experimental study on the performance of flat-plate photobioreactors with different inner structures for microalgae cultivation. *J. Appl. Phycol.* 27, 49–58. doi: 10.1007/s10811-014-0281-y.

Huang, J., Qu, X., Wan, M., Ying, J., Li, Y., Zhu, F., et al. (2015b). Investigation on the performance of raceway ponds with internal structures by the means of CFD simulations and experiments. *Algal Res.* 10, 64–71. doi: 10.1016/j.algal.2015.04.012.

Ishii, M., and Zuber, N. (1979). Drag coefficient and relative velocity in bubbly, droplet or particulate flows. *AIChE J.* 25, 843–855. doi: 10.1002/aic.690250513.

Jacob, A., Bucharsky, E. C., and GuenterSchell, K. (2012). The Application of Transparent Glass Sponge for Improvement of Light Distribution in Photobioreactors. *J. Bioprocess. Biotech.* 02. doi: 10.4172/2155-9821.1000113.

Jin, Y., Liu, C.-L., Song, X.-F., and Yu, J.-G. (2019). Computational fluid dynamics simulation as a tool for optimizing the hydrodynamic performance of membrane bioreactors. *RSC Adv.* 9, 32034–32046. doi: 10.1039/C9RA06706J.

Joshi, J. B. (2001). Computational flow modelling and design of bubble column reactors. *Chem. Eng. Sci.* 56, 5893–5933. doi: 10.1016/S0009-2509(01)00273-1.

Juřena, T., Vondál, J., Rebej, M., and Jegla, Z. (2020). Eulerian tracking of cumulative light dose in microalgal photobioreactor. in *Proceedings of the Engineering Mechanics 2020* 1. (Online: Brno University of Technology, Institute of Solid Mechanics, Mechatronics and Biomechanics), 254–257. doi: 10.21495/5896-3-254.

Kadic, E., and Heindel, T. J. (2014). *An Introduction to Bioreactor Hydrodynamics and Gas-Liquid Mass Transfer*. 1st ed. Hoboken, New Jersey: John Wiley & Sons, Inc.

Kong, B., and Vigil, R. D. (2014). Simulation of photosynthetically active radiation distribution in algal photobioreactors using a multidimensional spectral radiation model. *Bioresour. Technol.* 158, 141–148. doi: 10.1016/j.biortech.2014.01.052.

Kraakman, N. J. R., Rocha-Rios, J., and van Loosdrecht, M. C. M. (2011). Review of mass transfer aspects for biological gas treatment. *Appl. Microbiol. Biotechnol.* 91, 873–886. doi: 10.1007/s00253-011-3365-5.

Lamont, J. C., and Scott, D. S. (1970). An eddy cell model of mass transfer into the surface of a turbulent liquid. *AIChE J.* 16, 513–519. doi: 10.1002/aic.690160403.

Linek, V., Moucha, T., and Sinkule, J. (1996). Gas-liquid mass transfer in vessels stirred with multiple impellers—I. Gas-liquid mass transfer characteristics in individual stages. *Chem. Eng. Sci.* 51, 3203–3212. doi: 10.1016/0009-2509(95)00395-9.

Liu, Z., Zheng, Y., Jia, L., and Zhang, Q. (2005). Study of bubble induced flow structure using PIV. *Chem. Eng. Sci.* 60, 3537–3552. doi: 10.1016/j.ces.2004.03.049.

López-Rosales, L., Sánchez-Mirón, A., Contreras-Gómez, A., García-Camacho, F., Battaglia, F., Zhao, L., et al. (2019). Characterization of bubble column photobioreactors for shear-sensitive microalgae culture. *Bioresour. Technol.* 275, 1–9. doi: 10.1016/j.biortech.2018.12.009.

Luo, H.-P., and Al-Dahhan, M. H. (2010). Local gas holdup in a draft tube airlift bioreactor. *Chem. Eng. Sci.* 65, 4503–4510. doi: 10.1016/j.ces.2010.04.037.

Marella, T. K., and Tiwari, A. (2020). Marine diatom Thalassiosira weissflogii based biorefinery for co-production of eicosapentaenoic acid and fucoxanthin. *Bioresour. Technol.* 307, 123245. doi: 10.1016/j.biortech.2020.123245.

McClure, D. D., Norris, H., Kavanagh, J. M., Fletcher, D. F., and Barton, G. W. (2014). Validation of a Computationally Efficient Computational Fluid Dynamics (CFD) Model for Industrial Bubble Column Bioreactors. *Ind. Eng. Chem. Res.* 53, 14526–14543. doi: 10.1021/ie501105m.

McHardy, C., Luzi, G., Lindenberger, C., Agudo, J. R., Delgado, A., and Rauh, C. (2018). Numerical analysis of the effects of air on light distribution in a bubble column photobioreactor. *Algal Res.* 31, 311–325. doi: 10.1016/j.algal.2018.02.016.

Moukalled, F., Mangani, L., and Darwish, M. (2016). *The Finite Volume Method in Computational Fluid Dynamics*. 1st ed. Switzerland: Springer International Publishing.

Murgan, I., Bunea, F., and Ciocan, G. D. (2017). Experimental PIV and LIF characterization of a bubble column flow. *Flow Meas. Instrum.* 54, 224–235. doi: 10.1016/j.flowmeasinst.2017.02.004.

Ndiaye, M., Gadoin, E., and Gentric, C. (2018). CO2 gas–liquid mass transfer and kLa estimation: Numerical investigation in the context of airlift photobioreactor scale-up. *Chem. Eng. Res. Des.* 133, 90–102. doi: 10.1016/j.cherd.2018.03.001.

Nedbal, L., Trtílek, M., Červený, J., Komárek, O., and Pakrasi, H. B. (2008). A photobioreactor system for precision cultivation of photoautotrophic microorganisms and for high-content analysis of suspension dynamics. *Biotechnol. Bioeng.* 100, 902–910. doi: 10.1002/bit.21833.

Ngo, S. I., and Lim, Y.-I. (2020). Multiscale Eulerian CFD of Chemical Processes: A Review. *ChemEngineering* 4, 23. doi: 10.3390/chemengineering4020023.

Papacek, S., Jablonsky, J., and Petera, K. (2018). Advanced integration of fluid dynamics and photosynthetic reaction kinetics for microalgae culture systems. *BMC Syst. Biol.* 12. doi: 10.1186/s12918-018-0611-9.

Park, S., and Li, Y. (2015). Integration of biological kinetics and computational fluid dynamics to model the growth of Nannochloropsis salina in an open channel raceway. *Biotechnol. Bioeng.* 112, 923–933. doi: 10.1002/bit.25509.

Patil, S. S., Behera, B., Sen, S., and P., B. (2021). Performance evaluation of bubble column photobioreactor along with CFD simulations for microalgal cultivation using human urine. *J. Environ. Chem. Eng.* 9, 104615. doi: 10.1016/j.jece.2020.104615.

Patnaik, R., Singh, N. K., Bagchi, S. K., Rao, P. S., and Mallick, N. (2019). Utilization of Scenedesmus obliquus Protein as a Replacement of the Commercially Available Fish Meal Under an Algal Refinery Approach. *Front. Microbiol.* 10. doi: 10.3389/fmicb.2019.02114.

Pelczar, M. J., Chan, E. C. S., and Krieg, N. R. (1993). *Microbiology*. Tata McGraw-Hill.

Pires, J. C. M., Alvim-Ferraz, M. C. M., and Martins, F. G. (2017). Photobioreactor design for microalgae production through computational fluid dynamics: A review. *Renew. Sustain. Energy Rev.* 79, 248–254. doi: 10.1016/j.rser.2017.05.064.

Posten, C. (2009). Design principles of photo-bioreactors for cultivation of microalgae. *Eng. Life Sci.* 9, 165–177. doi: https://doi.org/10.1002/elsc.200900003.

Pozzobon, V., and Perré, P. (2020). Multiscale numerical workflow describing microalgae motion and light pattern incidence towards population growth in a photobioreactor. *J. Theor. Biol.* 498, 110293. doi: 10.1016/j.jtbi.2020.110293.

PSI (2021). Photon Systems Instruments. *Photobioreactors*. Available at: https://photo-bio-reactors.com/products/photobioreactors/#gallery.

Pulz, O. (2001). Photobioreactors: production systems for phototrophic microorganisms. *Appl. Microbiol. Biotechnol.* 57, 287–293. doi: 10.1007/s002530100702.

Raffel, M., Willert, C. E., Scarano, F., Kähler, C. J., Wereley, S. T., and Kompenhans, J. (2018). "Introduction," in *Particle Image Velocimetry: A Practical Guide* (Cham, Switzerland: Springer International Publishing AG), 1–32. doi: 10.1007/978-3-319-68852-7_1.

Ramírez-López, C., Perales-Vela, H. V., and Fernández-Linares, L. (2019). Biomass and lipid production from Chlorella vulgaris UTEX 26 cultivated in 2 m3 raceway ponds under semicontinuous mode during the spring season. *Bioresour. Technol.* 274, 252–260. doi: 10.1016/j.biortech.2018.11.096.

Rebej, M., Vondál, J., and Jegla, Z. (2021). Numerical Study of the Air Injection Method into the Flat-Panel Photobioreactor. in *Proceedings of the 6th world congress on momentum, heat and mass transfer (MHMT 2021)* doi: 10.11159/enfht21.lx.305.

Rebej, M., Vondál, J., Juřena, T., Brummer, V., Jegla, Z., and Naď, M. (2022a). Numerical simulations of mass transfer prediction in a photobioreactor. in *Chemical Engineering Transactions* (AIDIC Servizi S.r.l.), 127–132. doi: 10.3303/CET2293022.

Rebej, M., Vondál, J., Juřena, T., and Jegla, Z. (2020). Evaluation of different drag models for simulations of a bubbly flow in a flat-panel photobioreactor. in *Proceedings of the 26th International Conference "Engineering Mechanics 2020"* 1. (Brno University of Technology, Institute of Solid Mechanics, Mechatronics and Biomechanics), 432–435. doi: 10.21495/5896-3-432.

Rebej, M., Vondál, J., Juřena, T., Naď, M., and Jegla, Z. (2022b). Sensitivity study of a bubble size on mass transfer in a CFD model of a bubble-column photobioreactor. in (Milovy, Czech Republic: Institute of Theoretical and Applied Mechanics of the Czech Academy of Sciences), 329–332. doi: 10.21495/51-2-329.

Rodolfi, L., Biondi, N., Guccione, A., Bassi, N., D'Ottavio, M., Arganaraz, G., et al. (2017). Oil and eicosapentaenoic acid production by the diatom Phaeodactylum tricornutum cultivated outdoors in Green Wall Panel (GWP®) reactors. *Biotechnol. Bioeng.* 114, 2204–2210. doi: 10.1002/bit.26353.

Sabeti, M. B., Hejazi, M. A., and Karimi, A. (2019). Enhanced removal of nitrate and phosphate from wastewater by Chlorella vulgaris: Multi-objective optimization and CFD simulation. *Chin. J. Chem. Eng.* 27, 639–648. doi: 10.1016/j.cjche.2018.05.010.

Sander, R. (2015). Compilation of Henry's law constants (version 4.0) for water as solvent. *Atmospheric Chem. Phys.* 15, 4399–4981. doi: 10.5194/acp-15-4399-2015.

Seo, I., Lee, I., Hwang, H., Hong, S., Bitog, J. P., Kwon, K., et al. (2012). Numerical investigation of a bubble-column photo-bioreactor design for microalgae cultivation. *Biosyst. Eng.* 113, 229–241. doi: 10.1016/j.biosystemseng.2012.08.001.

Seo, I., Lee, I.-B., Hong, S.-W., Bitog, J. P., Kwon, K. S., Lee, C., et al. (2014). Evaluation of a photobioreactor performance grafting microalgal growth model and particle tracking technique using CFD. *Trans. ASABE* 57, 121–139. doi: 10.13031/trans.57.10339.

Singh, R. N., and Sharma, S. (2012). Development of suitable photobioreactor for algae production – A review. *Renew. Sustain. Energy Rev.* 16, 2347–2353. doi: 10.1016/j.rser.2012.01.026.

Soman, A., and Shastri, Y. (2015). Optimization of novel photobioreactor design using computational fluid dynamics. *Appl. Energy* 140, 246–255. doi: 10.1016/j.apenergy.2014.11.072.

Sukačová, K., Lošák, P., Brummer, V., Máša, V., Vícha, D., and Zavřel, T. (2021). Perspective Design of Algae Photobioreactor for Greenhouses—A Comparative Study. *Energies* 14, 1338. doi: 10.3390/en14051338.

Tanaka, T., Yabuuchi, T., Maeda, Y., Nojima, D., Matsumoto, M., and Yoshino, T. (2017). Production of eicosapentaenoic acid by high cell density cultivation of the marine oleaginous diatom Fistulifera solaris. *Bioresour. Technol.* 245, 567–572. doi: 10.1016/j.biortech.2017.09.005.

Thobie, C., Gadoin, E., Blel, W., Pruvost, J., and Gentric, C. (2017). Global characterization of hydrodynamics and gas-liquid mass transfer in a thin-gap bubble column intended for microalgae cultivation. *Chem. Eng. Process. Process Intensif.* 122, 76–89. doi: 10.1016/j.cep.2017.10.009.

Tomiyama, A. (1998). Struggle with computational bubble dynamics. *Multiph. Sci. Technol.* 10, 369–405. doi: 10.1615/MultScienTechn.v10.i4.40.

Wang, C., and Lan, C. Q. (2018). Effects of shear stress on microalgae – A review. *Biotechnol. Adv.* 36, 986–1002. doi: 10.1016/j.biotechadv.2018.03.001.

Wheaton, Z. C., and Krishnamoorthy, G. (2012). Modeling radiative transfer in photobioreactors for algal growth. *Comput. Electron. Agric.* 87, 64–73. doi: 10.1016/j.compag.2012.05.002.

Wu, X., and Merchuk, J. C. (2003). Measurement of fluid flow in the downcomer of an internal loop airlift reactor using an optical trajectory-tracking system. *Chem. Eng. Sci.* 58, 1599–1614. doi: 10.1016/S0009-2509(02)00662-0.

Zeng, F., Huang, J., Meng, C., Zhu, F., Chen, J., and Li, Y. (2016). Investigation on novel raceway pond with inclined paddle wheels through simulation and microalgae culture experiments. *Bioprocess Biosyst. Eng.* 39, 169–180. doi: 10.1007/s00449-015-1501-9.

Zhang, D., Dechatiwongse, P., and Hellgardt, K. (2015). Modelling light transmission, cyanobacterial growth kinetics and fluid dynamics in a laboratory scale multiphase photo-bioreactor for biological hydrogen production. *Algal Res.* 8, 99–107. doi: 10.1016/j.algal.2015.01.006.

Zhang, Q., Wu, X., Xue, S., Liang, K., and Cong, W. (2013). Study of hydrodynamic characteristics in tubular photobioreactors. *Bioprocess Biosyst. Eng.* 36, 143–150. doi: 10.1007/s00449-012-0769-2.

Zhao, L., Tang, Z., Gu, Y., Shan, Y., and Tang, T. (2018). Investigate the cross-flow flat-plate photobioreactor for high-density culture of microalgae. *Asia-Pac. J. Chem. Eng.* 13, e2247. doi: 10.1002/apj.2247.

Ziegenhein, T., and Lucas, D. (2017). Observations on bubble shapes in bubble columns under different flow conditions. *Exp. Therm. Fluid Sci.* 85, 248–256. doi: 10.1016/j.expthermflusci.2017.03.009.

Nomenclature

Acronyms

ADV	Acoustic Doppler Velocimetry
CFD	Computational Fluid Dynamics
E-E	Eulerian–Eulerian
E-L	Eulerian–Lagrangian
EPA	Eicosapentaenoic Acid
LED	Light Emitting Diode
LDA	Laser Doppler Anemometry
PIV	Particle Image Velocimetry
PSU	Photosynthetic Unit
PUFA	Polyunsaturated Fatty Acid
rpm	Revolutions per Minute
RSM	Reynolds Stress Model
SFA	Saturated Fatty Acid
SIMPLE	Semi-Implicit Method for Pressure-Linked Equations
SP	Single Phase
SST	Shear Stress Transport
UDF	User-Defined Function

Latin Letters

α	volume fraction	$[m^3\ m^{-3}]$
a	specific gas-liquid interfacial area	$[m^2\ m^{-3}]$
β	light scattering coefficient	$[m^{-1}]$
C_G	pollutant concentrations in the gaseous phase	$[g\ m^{-3}]$
C_L	pollutant concentrations in the liquid	$[g\ m^{-3}]$
C_{CO_2}	CO_2 concentration	$[g\ m^{-3}]$
d_B	bubble diameter	$[m]$
$\Delta\rho$	density difference	$[kg\ m^{-3}]$
d_h	horizontal diameter	$[m]$
D_L	diffusivity of the solute in the liquid phase	$[m^2\ s^{-1}]$
d_v	vertical diameter	$[m]$
Eo	Eötvös number	$[-]$
ε_L	liquid turbulence dissipation rate	$[m^2\ s^{-3}]$
F	the penetration model constant	$[-]$
g	gravitational acceleration	$[m\ s^{-2}]$
H	Henry constant	$[-]$
I	irradiance	$[W\ m^{-2}]$
Ic	compensation irradiance	$[W\ m^{-2}]$
Ii	inhibition irradiance	$[W\ m^{-2}]$
Is	saturation irradiance	$[W\ m^{-2}]$
K	the eddy cell model constant	$[-]$
k_B	biofilm mass-transfer coefficient	$[m\ s^{-1}]$
k_G	gas phase mass-transfer coefficient	$[m\ s^{-1}]$
k_L	liquid phase mass-transfer coefficient	$[m\ s^{-1}]$
k_La	volumetric mass-transfer coefficient	$[s^{-1}]$
Mo	Morton number	$[-]$
R	overall volumetric mass-transfer rate	$[g\ m^{-3}\ s^{-1}]$
Re	Reynolds number	$[-]$
ρ_p	primary phase density	$[kg\ m^{-3}]$

σ	surface tension	$[N\ m^{-1}]$
$\vec{\mathrm{U}}_{(g)}$	velocity vector for the gas phase	$[m\ s^{-1}]$
$\vec{\mathrm{U}}_{(l)}$	velocity vector for the liquid phase	$[m\ s^{-1}]$
μ_p	dynamic viscosity of the primary phase	$[Pa\ s]$
u_{slip}	slip velocity between phases	$[m\ s^{-1}]$
ν_L	kinematic viscosity of the liquid	$[m^2\ s]$
x_1	resting (open) state	$[-]$
x_2	active (closed) state	$[-]$
x_3	inhibited state	$[-]$
$\vec{\mathrm{X}}_{(g)}$	position vector for the gaseous phase	$[m]$
$\vec{\mathrm{X}}_{(l)}$	position vector for the liquid phase	$[m]$

List of Author’s Other Activities

Publications

REBEJ, M., VONDÁL, J., JUŘENA, T., BRUMMER, V., JEGLA, Z., AND NAĎ, M. (2022). *Numerical simulations of mass transfer prediction in a photobioreactor.* in Chemical Engineering Transactions (AIDIC Servizi S.r.l.), 127–132. doi: 10.3303/CET2293022.

REBEJ, M., VONDÁL, J., JUŘENA, T., NAĎ, M., AND JEGLA, Z. (2022). *Sensitivity study of a bubble size on mass transfer in a CFD model of a bubble-column photobioreactor.* in (Milovy, Czech Republic: Institute of Theoretical and Applied Mechanics of the Czech Academy of Sciences), 329–332. doi: 10.21495/51-2-329.

REBEJ, M.; VONDÁL, J.; JEGLA, Z. *Numerical study of the air injection method into the flat-panel photobioreactor.* Proceedings of the 6th World Congress on Momentum, Heat and Mass Transfer (MHMT 2021). Proceedings of the World Congress on Momentum, Heat and Mass Transfer. Ottawa, Canada: 2021. p. 305-1 (305-8 p.) ISBN: 978-1-927877-89-0. ISSN: 2371-5316.

JUŘENA, T.; VONDÁL, J.; REBEJ, M.; JEGLA, Z. *Eulerian tracking of cumulative light dose in microalgal photobioreactor.* Proceedings of the 26th International Conference "Engineering Mechanics 2020". Brno, Czech Republic: Brno University of Technology, Institute of Solid Mechanics, Mechatronics and Biomechanics, 2020. p. 254-257. ISBN: 978-80-214-5896-3. ISSN: 1805-8248.

REBEJ, M.; VONDÁL, J.; JUŘENA, T.; JEGLA, Z. *Evaluation of different drag models for simulations of a bubbly flow in a flat-panel photobioreactor.* Proceedings of the 26th International Conference "Engineering Mechanics 2020". Brno, Czech Republic: Brno University of Technology, Institute of Solid Mechanics, Mechatronics and Biomechanics, 2020. p. 432-435. ISBN: 978-80-214-5896-3. ISSN: 1805-8248.

JUŘENA, T.; HÁJEK, J.; REBEJ, M.; VONDÁL, J. *Jak se daří mikrořasám v CFD modelech fotobioreaktorů?*. In: 66th Conference of Chemical and Process Engineering “CHISA 2019”. Key-note lecture. Seč, Czech Republic, 2019.

Rebej, M., Juřena, T., Vondál, J., Fuente, D. H., Červený, J., Jegla, Z. (2022). Numerical simulations and validation of single- and two-phase flow in a stirred lab-scale photobioreactor. *Biosystems Engineering*. Under review.

Supervision of Master Thesis

VINCE, Tomáš. CFD analýza tepelného zatížení trubkovnice. Brno, 2021. Available at: https://www.vutbr.cz/studenti/zav-prace/detail/132873. Master's Thesis. Brno University of Technology, Faculty of Mechanical Engineering, Institute of Process Engineering. Supervisor: Miroslav Rebej

Reviews of Master Thesis

WITOS, Anton. Užití vizualizační metody pro rekonstrukci výměníkové sítě [online]. Brno, 2022. Available at: https://www.vutbr.cz/studenti/zav-prace/detail/140751. Master's Thesis. Brno University of Technology, Faculty of Mechanical Engineering, Institute of Process Engineering. Supervisor: Zdeněk Jegla.

POLCSÁK, Jakub. Predikce a experimentální ověření funkce distribučního systému typu Z [online]. Brno, 2021. Available at: https://www.vutbr.cz/studenti/zav-prace/detail/132708. Master's Thesis. Brno University of Technology, Faculty of Mechanical Engineering, Institute of Process Engineering. Supervisor: Dominika Babička Fialová.

Academic Activities

Teaching exercises from Balancing of Process and Energy Systems (KBP) during winter term in the academic year 2019/2020.

Teaching exercises from Practical applications of CFD during winter term in 2019 to 2022.

Teaching exercises from Design of Process and Power Systems during winter term in 2019 to 2021.

Grants

Fond Vědy 2020 – Experimental exercises in fluid dynamics

Brno Ph.D. Talent 2019 beneficiary

Workshops

ANSYS ICEM 2021 – workshop on meshing in ANSYS ICEM